Ferroelectric control of magnetism in artificial multiferroic composites

Inauguraldissertation
zur
Erlangung der Würde eines Doktors der Philosophie
vorgelegt der
Philosophisch-Naturwissenschaftlichen Fakultät
der
Universität Basel
von

Jakoba Kolumbine Heidler
aus München, Deutschland

Basel, 2015

Genehmigt von der Phlilosophisch-Naturwissenschaftlichen Fakultät

auf Antrag von

Fakultätsverantwortlicher: Prof. Dr. Frithjof Nolting
Korreferent: Prof. Dr. Michel Kenzelmann

Basel, den 21.04.2015

Prof. Dr. Jörg Schibler
Dekan

Abstract

In this thesis, we studied ferromagnet/ferroelectric heterostructures, so-called artificial multiferroic composites, which exhibit magnetoelectric coupling between different ferroic order parameters. For a range of material combinations, we found that electrical switching of the ferroelectric polarization induces *non-volatile* reversible magnetization changes in the magnetic constituent and we contributed to the understanding of the underlying interface coupling mechanisms.

The ferromagnet/ferroelectric system $La_{0.7}Sr_{0.3}MnO_3$/ $[Pb(Mg_{1/3}Nb_{2/3})O_3]_{0.68}$-$[PbTiO_3]_{0.32}$ (011) (LSMO/PMN-PT) enables magnetoelectric control of the double exchange interaction via strain. Reversible electrical switching of the ferroelectric polarization induces a 10 K shift of the magnetic Curie temperature T_C. A similar magnitude in T_C change has been previously only observed under applied electric fields. Sweeping between oppositely out of plane (OOP) poled ferroelectric polarization directions, PMN-PT (011) may exhibit an in-plane (IP) poled state where the ferroelectric polarization lies in the surface plane. OOP and IP poled configurations are stable at remanence and reciprocal space maps highlight the accompanying lattice parameter changes which impose a biaxial strain on the manganite thin film. The magnetic response to the strain changes is probed by temperature dependent Mn $L_{3,2}$ x-ray magnetic circular dichroism (XMCD) providing quantitative values of the Mn spin and orbital moment. X-ray natural linear dichroism spectra for both strain states probe changes in the valence charge anisotropy. Multiplet and density functional theory calculations support the picture that the existing population imbalance between out of plane and in plane oriented orbitals increases further with tensile strain, favoring orbital occupation in the surface plane. An increase in tensile in-plane strain leads to an increased energy difference between the two e_g orbitals and a larger Mn-O-bond length. Increasing the electron-lattice coupling and reducing the e_g electron itinerancy that leads to ferromagnetism due to the double exchange interaction, results ultimately in lower T_C values in agreement with the Millis model.

In Co/PMN-PT (011), we disentangle the strain and charge contributions to the magnetic response upon electrical switching, using XMCD at the Co $L_{3,2}$ edges as the main probe. Our results evidence the coexistence of two coupling mechanisms leading to three distinct magnetization states upon electrical switching. If the ferroelectric polarization is switched to the IP poled state, the corresponding lattice parameter changes in the PMN-PT exert a strain on the Co layer and induce an anisotropy change with higher remanent magnetization along the $[01\bar{1}]$ direction. When comparing oppositely OOP poled ferroelectric polarization configurations, an additional Co anisotropy change is observed. Since the structure of PMN-PT in the

two OOP poled states is equivalent, this dependence of the anisotropy must stem from the substrate polarity. The bound charge at the interface is expected to be screened by the cobalt metal within the Thomas Fermi screening length of a few Angstroms. We use a Co wedge geometry to study the magnetic response as a function of Co layer thickness employing XMCD with surface sensitive total electron yield detection. Consequently, the anisotropy change induced by the charged substrate is observed for the thinner part but absent in the thicker part of the Co wedge.

Lattice parameter values for cobalt and PMN-PT obtained by x-ray diffraction as well as domain distributions obtained from atomic force microscopy serve as an input for density functional theory calculations which reproduce the experimentally observed anisotropy behaviour for fcc (111) textured cobalt as a function of the lateral strain and charge. Our investigation unravels how magnetoelasticity and interfacial charge density trigger changes in the magnetic anisotropy. The observed coexistence of multiple coupling mechanisms opens up the possibility to tune and enhance the cross-coupling between layers in heterostructures.

The possibility to induce ferromagnetism in a per se paramagnetic system via electrical switching is explored for a $Pd/Pb(Zr_{0.2}Ti_{0.8})O_3$ heterostructure. Pd has a large magnetic susceptibility and is close to fulfilling the Stoner criterion for magnetism. According to calculations the polarity of adjacent ferroelectric layers could trigger a paramagnetic/ferromagnetic transition in paramagnetic metals by introducing shifts in the density of states. No XMCD difference signal upon ferroelectric switching was found within the noise ratio of 0.2% at the $M_{3,2}$ edge and of 1% at the $L_{3,2}$ edge.

Contents

1 Introduction **7**
1.1 From intrinsic to artificial multiferroics 8

2 Characteristics of the material components **11**
2.1 Ferroelectric perovskite oxides 11
2.1.1 $Pb(Zr_{1-x}Ti_x)O_3$ 13
2.1.2 Relaxor ferroelectric $[Pb(Mg_{1/3}Nb_{2/3})O_3]_{(1-x)}$ -$[PbTiO_3]_x$ . . . 14
2.2 Band ferromagnets 16
2.2.1 Stoner band theory of ferromagnetism 16
2.2.2 Magnetic anisotropy 19
2.3 Ferromagnetic perovskite oxides 22
2.3.1 Jahn-Teller effect 23
2.3.2 Double exchange mechanism 24
2.3.3 Strain dependence 24

3 Experimental techniques and instrumentation **27**
3.1 X-ray absorption spectroscopy 28
3.2 X-ray magnetic circular dichroism 30
3.2.1 Quantum mechanical origin of the XMCD effect 30
3.2.2 Sum rules 32
3.3 X-ray natural linear dichroism 35
3.3.1 MultiX multiplet calculations 36
3.4 Instrumentation 37
3.4.1 X-ray absorption spectroscopy beamlines 37
3.5 X-ray diffraction - reciprocal space maps 40

4 Charge modulation at the Pd/PZT interface **43**
4.1 Results 43
4.1.1 Sample fabrication 43

4.1.2 XAS and XMCD at the Pd M edge . . . 45
4.1.3 XAS and XMCD at the Pd L edge . . . 48
4.2 Discussion/Conclusion . . . 48

5 Controlling magnetism via strain - LSMO/PMN-PT 53
5.1 Results . . . 54
5.1.1 Sample preparation and experimental details . . . 54
5.1.2 Strain dependent XAS and XMCD measurements . . . 54
5.1.3 X-ray diffraction - 2D reciprocal space maps . . . 59
5.1.4 Strain dependent x-ray natural linear dichroism . . . 62
5.2 Discussion . . . 67
5.3 Conclusion . . . 68

6 Controlling magnetism via strain and charge - Co/PMN-PT 71
6.1 Results . . . 72
6.1.1 Sample preparation and experimental details . . . 72
6.1.2 Strain mediated magnetoelectric coupling . . . 73
6.1.3 Dependence on the polarity of the substrate . . . 74
6.2 Discussion . . . 76
6.3 Conclusion . . . 81

7 Conclusion and outlook 83

Thank you so much 87

List of publications 89

Bibliography 91

List of abbreviations

AFM	atomic force microscopy
DFT	density functional theory
DOS	density of states
fcc	face centered cubic
FE	ferroelectric
FM	ferromagnetic
hcp	hexagonal close packed
IP	in plane
LH	linear horizontal
LSMO	$La_{1-x}Sr_xMnO_3$
LV	linear vertical
ME	magnetoelectric
MOKE	magneto-optical Kerr effect
OOP	out of plane
PM	paramagnetic
PMN-PT	$[Pb(Mg_{1/3}Nb_{2/3})O_3]_{(1-x)}$ -$[PbTiO_3]_x$
PZT	$Pb(Zr_{1-x}Ti_x)O_3$
RSM	reciprocal space map

STO	$SrTiO_3$
TEY	total electron yield
TFY	total fluorescence yield
XAS	x-ray absorption spectroscopy
XMCD	x-ray magnetic circular dichroism
XNLD	x-ray natural linear dichroism
XRD	x-ray diffraction

Chapter 1

Introduction

This thesis focuses on interface coupling mechanisms in ferromagnet/ferroelectric heterostructures. The single ferroic constituents employed each have a spontaneous, switchable long-range order: In ferromagnetic (FM) materials the alignment of spins can be switched for example by a magnetic field; ferroelectrics (FE) show a remanent polarization that can be reoriented in applied electric fields; and ferroelastic materials exhibit spontaneous strain which can be switched under applied stress.

The prospect of coupling between different order parameters was at the heart of the effort undertaken to develop materials with more than one ferroic order. In the late fifties of the last century chemists and physicists succeeded to discover materials that show more than one ferroic order, inspired by Curie's idea in 1894 that materials can be electrically polarized by means of a magnetic field and magnetized by means of an electric field [1]. Proposed by Dzyaloshinskii due to symmetry considerations [2], Cr_2O_3 was the first magnetoelectric (ME) material discovered [3] where modifications in its antiferromagnetic order can be induced via applied electric fields. Soon afterwards materials with more than one ferroic order were discovered by systematic variations of stoichiometries during sample growth: The boracite [4] and phosphate [5] families as well as first solid solutions with perovskite structure such as $PbFe_{1/2}Nb_{1/2}O_3$ [6]. In these crystals, the magnetoelectric coupling between order parameters is small, though [7]. In 1994, Schmid attributed the term 'multiferroic' to the class of materials where two or more ferroic properties coexist [1]. Nowadays, many intrinsic multiferroic compounds are known. Amongst the fundamental classes are the perovskites with the most prominent example $BiFeO_3$, the hexagonal manganites with general formula $ReMnO_3$ (Re for Y, Ho, Er, Tm, Yb, Lu, or Sc), the boracite compounds with $M_3B_7O_{13}X$ (with M = Cr, Mn, Fe, Co, Cu or Ni, and X = Cl, Br, or I) the fluoride compounds of $BaXF_4$ (X = Mn, Fe, Co, Ni) and the

spinels such as magnetite Fe_3O_4, to name only some of them [8, 9].

Searching for ways to develop multiferroics with stronger cross-coupling requires the insight that magnetism and ferroelectricity contradict each other to some extent. Ferroelectricity arises from non-centrosymmetricity [10]. For example, an off-centering of ions with respect to their symmetric ligands induces an electric dipole moment. In magnetic materials, cations with an incompletely filled d shell avoid off-centering due to the increase in Coulomb repulsion [10].

1.1 From intrinsic to artificial multiferroics

Modern synthesis techniques enable the growth of thin films with unprecedented crystallinity and control of stoichiometry. This improvement contributed considerably to the field of research on so-called artificial multiferroic composites. In heterostructures consisting of cross-coupled ferroic layers [11], the constituents show properties that differ from their respective bulk behaviour. At interfaces, even new functionalities can arise. The prospect of electric field control of magnetism with its potential use in technological applications [12, 13, 14, 15] has focussed attention on the subgroup of artificial multiferroics that exhibits magnetoelectric coupling. Since the modular nature of heterostructures allows one to tune the interface coupling, they prove to be an advantageous concept in searching for ways to enhance the magnetic response upon electrical switching.

Regarding the choice of materials, the class of perovskite oxides comprises compositions that exhibit a wide range of properties such as ferromagnetism and antiferromagnetism, ferroelectricity, superconductivity and colossal magnetoresistance. Since the different compositions share the same building block from a crystallographic point of view, perovskites are well suited for heteroepitaxial growth. The diversity of their properties stems from the interplay between charge, spin and orbital degrees of freedom, making them very susceptible to changes in strain, charge doping or hybridization [9]. For example, the phase diagram of the lanthanum manganites $La_{1-x}Sr_xMnO_3$ (LSMO) includes paramagnetic and antiferromagnetic insulating phases as well as ferromagnetic metallic phases depending on the doping concentration of La/Sr [16].

The coupling mechanisms involved in different multilayer systems are manifold and involve interesting, new physics. In composites of piezoelectric (ferroelectric) and magnetostrictive (ferromagnetic) compounds, an applied electric field induces a lattice deformation in the piezoelectric constituent which is mechanically transferred to the magnetostrictive layer leading to a change in magnetization [17, 18, 19, 20].

Furthermore, ferroelectric polarization reversal may change the overlap between

atomic orbitals [21, 22, 23] or drive a magnetic reconstruction [24, 25, 26, 27, 28, 29] at the interface.

Charge-mediated ME coupling exploits the electric field effect [30, 31, 32, 33] as well as the remanent electric polarization of ferroelectric components [34, 35, 36, 26] to modulate the charge carrier concentration in an adjacent ferromagnetic layer, where accumulation or depletion of spin-polarized electrons results in a change of the interface magnetization.

Different length scales apply to the aforementioned mechanisms. While the influence of strain extends to several tens of nanometers, charge mediated ME coupling is typically an interface or surface sensitive effect where screening of surface charge takes place within the Thomas-Fermi screening length. It follows that, depending on materials of interest and sample geometry, the interplay between structure, bonding and polarity of adjacent layers can involve several ME coupling mechanisms.

This thesis studies the magnetoelectric coupling mechanisms in artificial multiferroic composites investigating a range of material combinations. The focus lies on *non-volatile* electric field induced changes in the anisotropy behaviour of the ferromagnetic constituent or in the exchange interaction path responsible for ferromagnetism. We observe both strain and charge induced coupling mechanisms. X-ray magnetic circular dichroism is used as the main probe.

The next chapter summarizes relevant properties of the employed materials. The theoretical basics of the x-ray absorption spectroscopy techniques used throughout this thesis including approaches for data analysis are explained in chapter 3.

Chapter 4 explores the possibility of inducing ferromagnetism in a per se paramagnetic (PM) system. According to calculations the polarity of adjacent ferroelectric layers could trigger a paramagnetic/ferromagnetic transition in paramagnetic metals by introducing shifts in the density of states of metals which are close to fulfilling the Stoner criterion for magnetism. Chapter 4 investigates that approach for a Pd/$Pb(Zr_{0.2}Ti_{0.8})O_3$ (PZT) heterostructure.

In contrast, chapters 5 and 6 investigate two-component systems where each layer exhibits a memory function on its own. Chapter 5 addresses the request for electrically switchable changes in LSMO thin film magnetization that are stable at remanence. The magnetoelectric coupling in a heterostructure consisting of ferromagnetic LSMO and the relaxor ferroelectric $[Pb(Mg_{1/3}Nb_{2/3})O_3]_{0.68}$ -$[PbTiO_3]_{0.32}$ (PMN-PT) (011) is studied. Due to the specific crystal orientation chosen for this system, the latter can impose two distinct remanent strain states on the epitaxially grown LSMO top layer. We find that reversible electrical switching of the ferroelectric polarization results in a 10 K shift of the ferromagnetic Curie temperature. X-ray

diffraction reciprocal space maps give a complete picture of the PMN-PT lattice deformations, which induce the T_C change in LSMO. Changes in crystal field during the switching process are highlighted in x-ray natural linear dichroism measurements and multiplet calculations.

Chapter 6 investigates the inverse magnetostrictive behaviour of a Co wedge (0-7 nm) in response to PMN-PT (011) upon switching. We can set three distinct remanent and reversible magnetization states at room temperature and disentangle the changes in anisotropy that arise from the coexistence of charge and strain. We relate the changes to the magnetocrystalline and magnetoelastic anisotropy, respectively.

At the end, a summary of the most important results and an outlook will be given.

Chapter 2

Characteristics of the material components

In this chapter the structure and functional properties of the material systems explored in this thesis will be briefly reviewed. Ferroelectric materials such as PZT and PMN-PT show a spontaneous electric polarization while their piezoelectric properties imply possibilities of strain engineering via electric fields. Section 2.1 explains structural features and lists relevant important properties of these ferroelectrics. Section 2.2 first gives a short general survey on band ferromagnetism elaborating on the possibilities to induce ferromagnetism in Pd/PZT composites investigated in chapter 4. Subsequently, the two main contributions to the magnetic anisotropy are summarized, as strain can cause changes in the anisotropy behaviour of ferromagnetic metals, a route that was envisaged in the Co/PMN-PT heterostructures of chapter 6. In the last section, relevant characteristics of the ferromagnetic perovskite oxide $La_{1-x}Sr_xMnO_3$ are discussed, as chapter 5 addresses magnetoelectric coupling in a LSMO/PMN-PT heterostructure. The properties of ferromagnetic oxides are very susceptible to strain-related changes in anisotropy and Curie temperature.

2.1 Ferroelectric perovskite oxides

The ferroelectrics used in this thesis belong to the perovskite class of oxides that share the crystal structure ABO_3 sketched in Fig. 2.1 (a) where the B site cation is surrounded by an oxygen octahedron and the A site cation must fit in the cube corner positions between corner sharing octahedra [37]. Depending on the ionic radii of the A and B cations the structure distorts from the ideal cubic structure of Fig. 2.1 (a) by rotating and tilting the oxygen octahedra or by displacing ions as parametrized

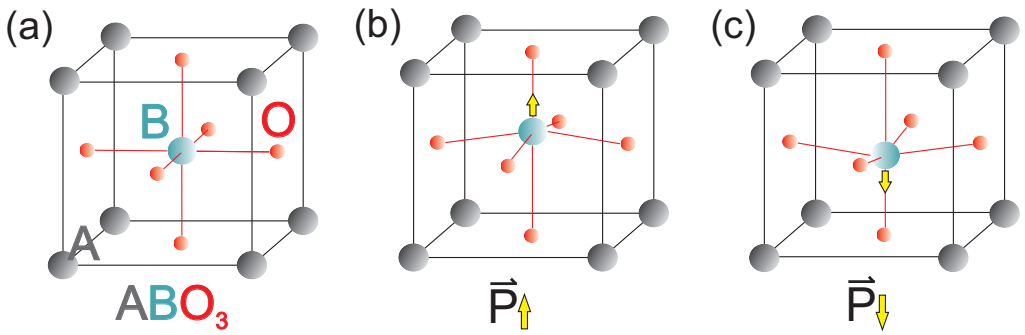

Figure 2.1: (a) Unit cell of the ABO_3 perovskite structure. The B cation is at the center of an oxygen octahedron, while the A cation occupies the spaces between corner sharing octahedra. (b) and (c): Ferroelectrics exhibit a spontaneous polarization, here indicated by atomic displacements inducing an electric dipole moment. By definition the spontaneous polarization has to be electrically switchable between multiple stable states.

by the Goldschmidt tolerance factor. The distortions can induce asymmetric charge surroundings as shown in Fig. 2.1 (b) thereby inducing electric dipole moments. An external electric field applied across the ferroelectric can align the neighboring dipole moments leading to a static bound charge at the ferroelectric surface. By definition, in ferroelectric materials the spontaneous electric polarization can be switched by an applied field between at least two equilibrium states, here illustrated by comparison of the ionic arrangements in Fig. 2.1 (b) and (c).

The polarization difference between oppositely poled states during the switching process can be measured in an I-V sweep, since the displacement of the ions causes a current flow $\mathbf{j} = \partial\mathbf{P}/\partial t$. In the I-V curve taken for a ferroelectric heterostructure $Pd(3\ nm)/Pb(Zr_{0.2}T_{0.8})O_3(200\ nm)/La_{0.65}Sr_{0.35}MnO_3(15\ nm)$ and shown in Fig. 2.2, switching peaks occur at voltages corresponding to the coercive field of the ferroelectric. The area under the curve is proportional to the spontaneous FE polarization. Apart from an external electric field, mechanical external stress and temperature can also change or induce a spontaneous polarization in a ferroelectric. Because the electric dipole moments are coupled to the lattice, a change in lattice parameters implies a change in dipole strength and FE polarization. The generation of a surface charge caused by external stress is called piezoelectricity. Pyroelectricity refers to induced FE polarization changes as a function of temperature. All ferroelectrics are piezoelectric and pyroelectric by nature, though the converse is not necessarily true.

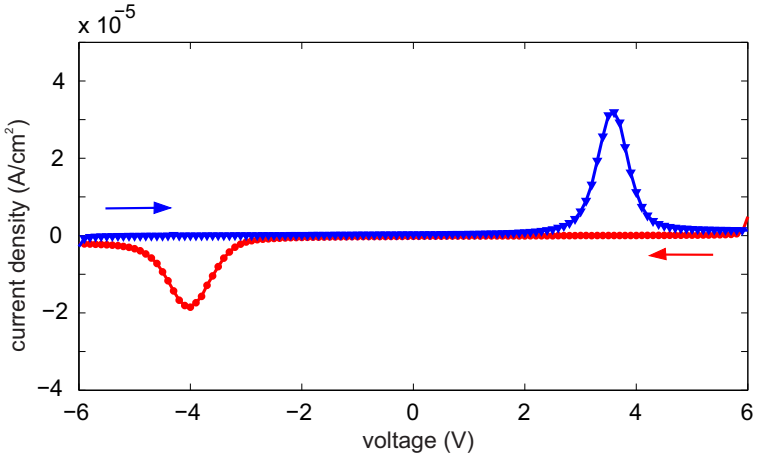

Figure 2.2: Displacement current density vs. applied voltage for a ferroelectric heterostructure Pd(3 nm)/Pb($Zr_{0.2}T_{0.8}$)O_3(200 nm)/$La_{0.65}Sr_{0.35}MnO_3$(15 nm) at 128 K. Arrows indicate the sweeping direction.The area under the curve corresponds to the spontaneous polarization.

2.1.1 $Pb(Zr_{1-x}Ti_x)O_3$

$Pb(Zr_{1-x}Ti_x)O_3$ [38, 39, 37] is a binary solid solution of the ferroelectric $PbTiO_3$ and the antiferroelectric[1] $PbZrO_3$ perovskite structures. The substitutions remain isoelectronic, i.e. Zr^{4+} for Ti^{4+}. For the Ti-rich compositions the cations are displaced along the [001] direction leading to a tetragonal symmetry, while the Zr-rich compositions are characterized by cation displacements along the [111] direction favouring a rhombohedral symmetry [39]. The piezoelectric response is highest close to the morphotropic phase boundary at compositions of about 50/50, where an applied electric field can induce a transition between rhombohedral and tetragonal symmetries [37]. The heterostructure in chapter 4 contains a composition closer to lead titanate, $Pb(Zr_{0.2}Ti_{0.8})O_3$. For $x = 0.8$, PZT has lattice constants a = 3.93 Å and c = 4.16 Å [41] and a Curie temperature around 450°C (see e.g. [38]). The electric field required to switch between polarization states is on the order of 1 V/1000 Å for thin films [42] as seen in Fig. 2.2. The investigated nanostructures in chapter 4 yield a remanent spontaneous polarization of 45 $\mu C/cm^2$.

[1] In antiferroelectric materials adjacent dipoles have opposite orientations resulting in zero remanent FE polarization on a macroscopic scale, but they can be aligned by a sufficiently high electric field [40].

2.1.2 Relaxor ferroelectric $[Pb(Mg_{1/3}Nb_{2/3})O_3]_{(1-x)}$ -$[PbTiO_3]_x$

Chapters 5 and 6 investigate heterostructures containing the relaxor ferroelectric alloy $[Pb(Mg_{1/3}Nb_{2/3})O_3]_{(1-x)}$ -$[PbTiO_3]_x$ where the A site is occupied by a Pb^{2+} ion, while the B site is occupied by Mg^{2+}, Nb^{5+} or Ti^{4+} ions [43].

Relaxors such as PMN with $x = 0$ are characterized by giant electrostriction and an extremely large dielectric constant showing a broad diffuse maximum associated with considerable frequency dispersion. They exhibit two essential structural characteristics: They contain chemically ordered nanoregions (CNR) embedded in a disordered matrix [44]. The cation order in the CNRs of PMN is of the form Pb $(\beta'_{1/2}\beta''_{1/2})O_3$ with sublattices β' and β''. Here, β' is solely occupied by Nb, β'' is randomly occupied by Nb and Mg. In its ordered form $Pb(Mg_{1/3}Nb_{2/3})O_3$ can then be written $Pb((Nb)_{1/2}(Mg_{2/3}Nb_{1/3})_{1/2})O_3$. This so-called 'random site' model for the B-site order is macroscopically charge balanced. In the disordered matrix the B site is randomly occupied. Annealing treatments aiming at complete ordering only showed negligible effects in PMN due to a too long relaxation time of ordering [43]. In addition to this compositional disorder polar nanoregions (PNR) exist that can be thought of as unusually large dipoles [45, 46, 47, 43]. These clusters of FE order start to freeze out at temperatures $T<T_B$ (the Burns temperature T_B, about 620 K for $Pb(Mg_{1/3}Nb_{2/3})O_3$). Upon cooling from the paraelectric state relaxors show a cross-over rather than a phase transition since there are no changes in the crystal structure on the macroscopic scale. A canonical relaxor does not undergo a spontaneous transition to the FE phase. But a phase with FE dipole order can be achieved via poling with external electric fields larger than the critical strength[2] below a certain freezing temperature, where the relaxation time for the reorientation of the dipoles becomes infinite [43, 49]. The FE hysteresis loops observed in relaxors compare well with normal ferroelectrics regarding the values of remanent polarization and coercive field.

Solid solutions of PMN and PT are expected to synergetically combine the properties of both relaxor ferroelectric PMN and ferroelectric PT [49]. The compositional phase diagram of PMN-PT shows a tetragonal crystal structure for PT rich compositions (above 37%) and a rhombohedral crystal structure for PT content below 30%. The morphotropic phase boundary corresponding to compositions from $x = 0.31$ to $x = 0.37$ [50] is characterized by an increased phase instability due to similar free energies of the various morphotropic phases [51]. The polarization can be easily rotated between different symmetries giving rise to an enhanced piezoelectric response. In this thesis, PMN-PT with a nominal doping of $x = 0.32$ is used. The crystal structure

[2]For PMN [48]: $E_{cr} = 1.7$ kV/cm at $T_c = 210K$.

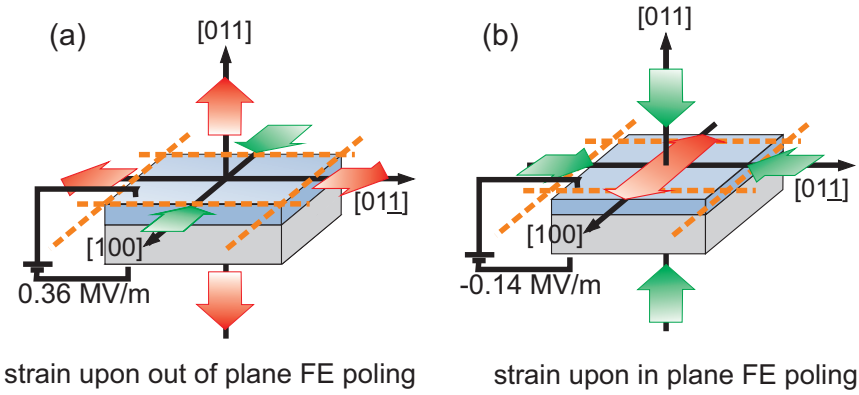

Figure 2.3: Schematic of the two distinct poled states in PMN-PT (011) that can be set by an electric field. (a) Strain state for OOP poled FE polarization. (b) At the coercive electric field the majority of the domains have FE polarization lying in the plane of the sample. The polarization rotation is accompanied by large lattice parameter changes for both IP and OOP poled configurations.

is monoclinic at room temperature with lattice constants a = 4.02 Å, b = 4.01 Å and c = 4.03 Å [50]. The switchable ferroelectric polarization is experimentally found to be 35 μC/cm^2.

For PMN-PT[3] with x =0.32 in the $(011)_{pc}$ cut (pc for pseudo-cubic; in the following this index will be omitted) Wu and coworkers reported on two reversible and remanent strain states that can be set by an applied voltage [20]. Figure 2.3 explains the two distinct strain states PMN-PT can impose on adjacent thin films if used in an artificial multiferroic composite. The FE polarization is poled out of plane (OOP) by applying ±0.36 MV/m at the bottom electrode, while the top electrode is connected to ground. FE domains align in parallel sharing an OOP lattice constant of c = 4.03 Å. In the following, I will refer to those domains as being in an OOP poled state. Sweeping between opposite OOP FE polarization directions, PMN-PT (011) may exhibit an in-plane poled state at the coercive electric field (±0.14 MV/m), where the FE polarization lies in the surface plane. I will refer to this configuration as the in plane (IP) poled state. Both OOP poled states as well as the IP poled configuration are stable at remanence. The lattice parameter changes are discussed in section 5.1.3.

[3]The text presented here is partly adapted from our recent publication [52].

2.2 Band ferromagnets

Cobalt and palladium are used as counterparts in artificial multiferroic composites in chapter 6 and 4 respectively. The Stoner-band model is the simplest model used to explain ferromagnetism in the 3d transition metals Fe, Co and Ni. Though Pd per se is not ferromagnetic, the Stoner band model places Pd in close proximity to the onset of ferromagnetism and, as such, Pd could be pushed into ferromagnetic order with the appropriate external stimulus.

2.2.1 Stoner band theory of ferromagnetism

The Stoner band model provides a successful simple approach to explain ferromagnetism in 3d transition metals. The approach outlined below follows the one given by Buschkow [53]. While Weiss' molecular field theory assumed localized electrons, Stoner used the theory of metallic properties introduced by Bloch, where electrons are treated as waves traveling through the crystal in the periodic field of the lattice [54]. In this collective electron treatment the distribution of states gives rise to a series of energy bands. Since electrons are partially shared between 4s, 3d↓ and 3d↑ bands, the Stoner band model was able to explain measured non-integer values of the magnetic moments [37]. For ferromagnetism to occur, the quantum-mechanical exchange energy is the fundamental driving force. The Hamiltonian in Eq. 2.1 accounts for the energy ascribed to the exchange interaction:

$$H = U_{eff} \cdot n_1 \cdot n_2 \tag{2.1}$$

Here, U_{eff}, a positive quantity, is the effective exchange energy per pair of 3d electrons, and $n_{1,2}$ represents the number of electrons per atom for each spin state, spin up ↑ and spin down ↓, where the total number of 3d electrons per atom is $n = n_1 + n_2$.

The schematic representation in Fig. 2.4 compares (a) paramagnetic and (b) ferromagnetic behaviour. In the latter case, an imbalance in the spin up and spin down electron occupation results in a reduction of the energy in Eq. 2.1. The energy gain ΔE_M with respect to equally filled spin up and spin down bands is given by

$$\Delta E_M = U_{eff} \cdot n_1 \cdot n_2 - U_{eff} \cdot \frac{n}{2} \cdot \frac{n}{2} = -U_{eff} \cdot n^2 \cdot p^2. \tag{2.2}$$

In the last step the fraction of electrons p that has moved from the spin down band to the spin up band was introduced: $p = (n_1 - n_2)/(2n)$. As sketched in Fig. 2.4 (b), a redistribution of n_1 and n_2 occupations requires the filling of states with higher

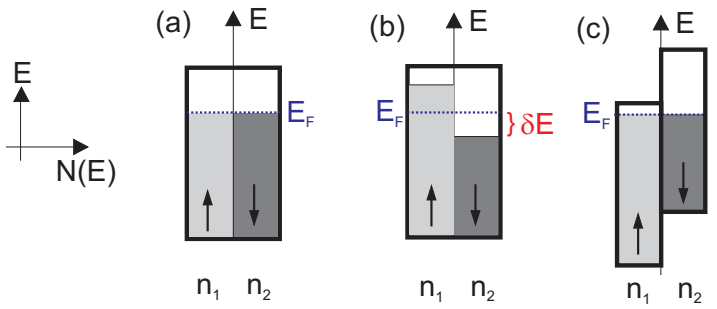

Figure 2.4: Schematic representation of the Stoner band model with partially depleted 3d band. (a) depicts the case of a paramagnetic DOS with two identical spin-up and spin-down bands, (b) shows a redistribution of spins in the case of a ferromagnet. Since the Fermi levels for spin up and spin down band have to align, (c) shows the exchange-split band structure, where the exchange interaction produces an exchange potential that effectively shifts the spin up and spin down DOS with respect to each other.

kinetic energy, hence it gives rise to an energy loss ΔE_{kin} counteracting the parallel spin alignment:

$$\Delta E_{kin} = 1/2 \cdot \delta E \cdot (n_1 - n_2) = \delta E \cdot n \cdot p \tag{2.3}$$

where $\delta E = E_1 - E_F = E_F - E_2$. From Fig. 2.4 (b) it can also be seen that $\frac{1}{2}(n_1 - n_2) = N(E_F)\delta E$. Then, the total change in energy ΔE is

$$\Delta E = \Delta E_{kin} + \Delta E_M = \frac{n^2 p^2}{N(E_F)}[1 - U_{eff} \cdot N(E_F)] \tag{2.4}$$

Hence, spontaneous magnetization arises, if

$$U_{eff} \cdot N(E_F) > 1, \tag{2.5}$$

which is the so-called Stoner criterion. It predicts ferromagnetism in metals for large values in U_{eff} and for a large density of states (DOS) at the Fermi level. Since, in Fig. 2.4 (b), the step at the Fermi level when comparing the DOS for spin up and spin down electrons is unphysical at equilibrium, Fig. 2.4 (c) shows a more appropriate picture, where the DOS for spin up and spin down electrons have been shifted to share the same Fermi energy. The so called 'exchange-split' DOS with an excess population of spin up electrons with respect to the number of spin down electrons is stabilized by the exchange energy. In the above description the model was simplified by rectangular 3d bands. In a realistic treatment one needs to consider the exact details of the DOS at the Fermi level. Janak reports calculated values of $U_{eff} \cdot N(E_F)$ for metallic elements ranging from Li to In [55] and predicts the

presence of ferromagnetism at the end of the 3d series for the elements Ni, Fe and Co due to their large 3d DOS at the Fermi level and a high exchange correlation parameter. In contrast, there is no ferromagnetism observed in the 4d series: The 4d wave functions extend further out from the nucleus implying a larger interaction with neighbouring atoms and a larger bandwidth resulting in a smaller density of states at the Fermi level [55]. However, Pd exhibits a large susceptibility enhancement due to the exchange interaction of the band electrons, with $U_{eff} \cdot N(E_F) = 0.775 \pm 0.039$. Gunnarson et al. reported values of $U_{eff} \cdot N(E_F) \sim 0.8$ [56].

Although exhibiting an atomic configuration of [Kr]4d10 with a completely filled 4d band, Pd is a paramagnetic metal in the solid state due to hybridization between 4d and 5s bands. Several theoretical electronic band structure calculations [57, 58, 59, 60, 61, 62, 63, 64] for Pd reveal that the Fermi level lies at a point where the DOS rapidly decreases following a steep slope towards higher energies. This implies the potential of tuning the exact position of $\mathrm{N(E}_F)$ via strain or charge and inspired an intense research to drive Pd magnetic.

Early experimental work [65, 66] considered alloys of Pd and magnetic elements. Upon addition of a small amount of magnetic impurities (0.1-0.2 at% Co [65] or Fe [66]) Pd develops polarization clouds in response to the exchange fields of the impurities. The measured total magnetic moment divided by the number of Co or Fe atoms respectively exceeds the nominal magnetic moment values for Co and Fe implying an induced ferromagnetic order in Pd. Also, Pd (111) films in contact with Ni (111) films showed ferromagnetic order [67].

Alternatively, ferromagnetism was predicted to develop upon a lattice expansion by about 5 to 10% with respect to the bulk metal [58, 59, 60]. An expanding lattice reflects a decrease in orbital overlap thereby reducing the bandwidth and triggering an increase of the DOS at the Fermi level. Also, the incorporation of 10% vacancies in a Pd matrix forecasts magnetism via charge transfer from the Pd to the vacancies [68].

Kudasov et al. [62] as well as Sun et al. [64] discussed the feasibility of driving a PM-FM phase transition by applying electric fields, either in a field effect structure or in a scanning tunneling microscope between tip and surface. In proximity to a gate layer under a negative potential, the metallic Pd layer responds by screening the electric field. Hence it develops a thin surface layer, depleted of electrons, where a shift of the Fermi level to lower energies enhances the local density of states. Sun et al. [64] expect that a shift in the Fermi level by about -4% should drive the system ferromagnetic. An electric field of 1.5 V/Å applied across a Pd/Ag (001) slab reduces the planar-averaged electron density at the interface by -0.006 1/Å^3 inducing a small planar-averaged spin density of 0.001 μ_B/Å^3. From density functional theory

calculations for bulk Pd, Kudasov et al. [62] assume that an increase in the DOS at the Fermi level by 10% induces ferromagnetism. A Fermi level shift of about -0.02 eV would require a number of excess holes $n_{h,bulk} = 0.04$ per Pd atom.

In this thesis, the route pursued to tune magnetism in Pd involves ferroelectric substrates instead of applied electric fields. PZT, with a spontaneous electric polarization $P = 90\mu$ C/cm^2 is used to modulate the charge carrier density with $n_e = 0.425$ electrons per surface area per Pd atom (here, a Pd surface area of 3.89×3.89 Å^2 per two Pd atoms is assumed). The ferroelectric polarization of PZT is nominally sufficient for the onset of ferromagnetism in Pd. However, the above discussion makes it clear that the onset of ferromagnetism in palladium depends crucially on the exact shape of the density of states and, implicitly, on the lattice mismatch upon growth, the hybridization with adjacent layers, and the penetration depth of the electric field.

2.2.2 Magnetic anisotropy

Ferromagnets exhibit hard and easy directions of magnetization within the crystal. The Heisenberg exchange interaction between spins cannot give rise to anisotropy since it is proportional to the scalar product of the spin vectors and a coherent rotation of the spin system does not change the exchange energy [69, 70]. Intrinsically, it is the spin-orbit coupling that provides a link between the magnetic spin moment and a crystal lattice and, as such, introduces magnetic anisotropy. Another factor influencing the magnetization alignment is the shape anisotropy which originates from the magnetic dipolar interaction. Since chapter 6 reports on electrically tunable anisotropy changes, the two contributions are explained here. This description follows Johnson et al. [69].

Magnetic dipolar interaction

The magnetic dipolar interaction in a material with magnetization $\mathbf{M}$ generates an internal field $\mathbf{H}_d$ opposite to the magnetization direction. This can be readily seen from one of Maxwell's equations using $\mathbf{B} = \mu_0(\mathbf{H} + \mathbf{M})$:

$$\nabla\mathbf{B} = \nabla(\mu_0(\mathbf{H} + \mathbf{M})) = 0 \tag{2.6}$$

$$\nabla\mathbf{H} = -\nabla\mathbf{M} \tag{2.7}$$

The magnetization $\mathbf{M}$ in a sample drops to zero at its surface resulting in a divergence of $\mathbf{M}$ [71]. Its existence is accompanied by an opposite divergence of $\mathbf{H}$. Equation (2.7) bears a similarity to the electrostatic analogue $\nabla\mathbf{E} = -\rho/\epsilon_0$, i.e. as

if fictitious magnetic monopoles have been left on the surface of the ferromagnet, and these monopoles act as sources of **H** [71]. The resulting **H** field is called the demagnetizing field $\mathbf{H}_d$. For the special case of ellipsoids and when **M** is uniform, it can be expressed as [69]

$$\mathbf{H}_d = -N \cdot \mathbf{M} \tag{2.8}$$

where N is a 3×3 demagnetizing tensor, that accounts for the geometric shape of a magnetized sample. The magnetostatic energy E_d related to the internal demagnetizing field $\mathbf{H}_d$ is [69]

$$E_d = -\frac{\mu_0}{2} \int_{volume} \mathbf{M} \cdot \mathbf{H}_d dV, \tag{2.9}$$

the factor 1/2 is introduced to correct for double counting since the integration runs over local magnetization elements that also contribute as a field source in $\mathbf{H}_d$. Regarding the demagnetizing field $\mathbf{H}_d$ of a thin film approximated as an infinite xy plane, all tensor elements are zero except the one referring to the z-direction $\mathrm{N}_{zz} = 1$. Then, the magnetostatic energy for a magnetized thin film (assuming saturation) amounts to

$$E_d = \frac{\mu_0}{2} M_{sat}^2 \cos^2 \theta, \tag{2.10}$$

where θ is the angle of the magnetization M_{sat} with respect the surface normal. Since the stray field contributions are minimized for an in-plane magnetization, $\theta = 90°$, the magnetic dipolar energy is responsible for the usual in-plane anisotropy of thin films, also called shape anisotropy.

Magnetocrystalline anisotropy

The Heisenberg exchange interaction between two spins that is responsible for ferromagnetism can not give rise to magnetic anisotropy since the associated exchange energy depends on the angle between spins only and not on the orientation of the spin axis relative to crystallographic directions [72]. On the other hand in transition metals in the solid state the orbital moment is almost completely quenched: in the crystal field of the surrounding atoms or ions the electron's orbit is restricted to preferred bonding directions. Hence, the orbital moment is strongly bound to the lattice. Intrinsically, it is the spin-orbit interaction that couples the magnetization to the lattice and defines hard and easy directions of magnetization within the crystal reflecting its symmetry. The magnetocrystalline anisotropy is the energy difference that arises due to different spin-orbit energies along 'easy' and 'hard' magnetization directions. The 'easy' axis of magnetization refers to the direction with the lowest spin-orbit energy. Forcing the magnetization away from that axis by applying

a magnetic field costs magnetocrystalline anisotropy energy required to overcome the spin-orbit coupling [73]. At interfaces and surfaces the symmetry is reduced compared to bulk leading to a modification of the magnetocrystalline contribution [72, 73].

Magnetoelastic anisotropy

Strain can influence the directions of easy and hard magnetization by changing the overlap of wave functions between neighbouring atoms, i.e. through the spin-orbit coupling. This reorientation of the magnetization is the inverse effect of magnetostriction. The magnetostriction coefficient $\lambda = \Delta l/l$ describes a change Δl in the sample dimension caused by an applied magnetic field. For positive λ values the material expands along the direction of applied magnetic field. Equivalently, if tensile stress elongates a magnetic sample with positive λ the magnetization increases [72]. In general the magnetostriction coefficient varies for different crystal axes and different orientations of the magnetization. Single crystalline hexagonal close packed (hcp) cobalt has negative magnetostriction values when measuring $\lambda \parallel \mathbf{H}$ for all angles tilted away from the hexagonal c-axis [74].

For a completely random polycrystalline material in a state of zero stress the relative change in length during magnetization from the demagnetized state to saturation λ_{sat} is a linear combination of the single-crystal magnetostriction constants [75, 76, 77, 78]:

$$\lambda_{\text{sat}} = \alpha\lambda_{100} + (1-\alpha)\lambda_{111}, \tag{2.11}$$

where the constants $\lambda_{100,111}$ represent the change in length along [100] or [111] in single crystalline cobalt when the magnetic field is also applied along that direction. In the case of uniform stress Akulov [75] derived $\alpha = 2/5$. For polycrystalline hcp cobalt $\lambda_{\text{sat}} = -62 \times 10^{-6}$ is reported [78]. Measurements on polycrystalline Co films report a negative magnetostriction coefficient λ_{par} parallel to the magnetic field [79, 80] and a positive λ_{trans} perpendicular to the applied magnetic field [80]. Klokholm et al. [81] report the same behaviour for polycrystalline films with both face centered cubic (fcc) and hcp phases present [81]. The inverse magnetostrictive effect might be at play in multilayer structures if there is a lattice misfit between top layers and substrate during epitaxial growth. In this thesis the inverse magnetostrictive behaviour of a Co thin film in response to a piezoelectric electrically switchable substrate is studied in chapter 6.

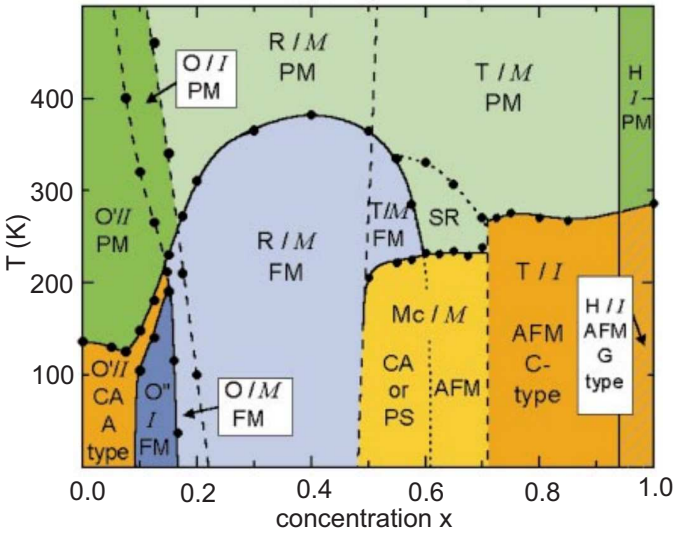

Figure 2.5: Phase diagram of $La_{1-x}Sr_xMnO_3$ as a function of doping and temperature from Ref. [16]. The crystal structures (orthorhombic (O), rhombohedral (R), tetragonal (T), monoclinic (Mc), and hexagonal(H)) are indicated, as well as the magnetic structures (paramagnetic (PM), short range order (SR), canted (CA), A-type antiferromagnetic (AFM), ferromagnetic (FM), phase separated (PS), and C-type AFM) and the electronic state (insulating (I), metallic (M).

2.3 Ferromagnetic perovskite oxides

The rare-earth manganites ($RE_{1-x}A_xMnO_3$, RE=rare earth, A=alkaline metal) belong to the class of the perovskite oxides with the crystal structure shown in Fig. 2.1 (a). In these compounds, a manganese ion is surrounded by an oxygen octahedron. The doping concentration x defines the distribution of aliovalent rare earth and alkaline ions and consequently the distribution of Mn^{3+}/Mn^{4+}. The doping ratio and cation sizes determine the Mn-O bond length as well as Mn-O-Mn bond angles and lead ultimately to a rich magnetic and electronic phase diagram. Fig. 2.5 shows the complexity of the system with several magnetic ground states of antiferromagnetic A- and C-type order ($x < 0.1$ and $x > 0.5$) as well as ferromagnetic order ($0.1 < x < 0.5$) [16]. At room temperature, $La_{1-x}Sr_xMnO_3$ exhibits an insulating, orthorhombic phase below $x = 0.2$, a ferromagnetic, metallic, rhombohedral phase for $0.2 < x < 0.5$, a ferromagnetic, metallic, tetragonal phase for $0.55 < x < 0.6$ as well as a metallic, tetragonal ($x > 0.55 < 0.7$) and insulating, hexagonal ($x > 0.95$) phases. In this thesis ferromagnetic metallic LSMO with x=0.3 doping is used. In bulk, the nominal Curie temperature is about 370 K. A strong interplay between electron transport, spin alignment and crystal lattice distortions makes LSMO very

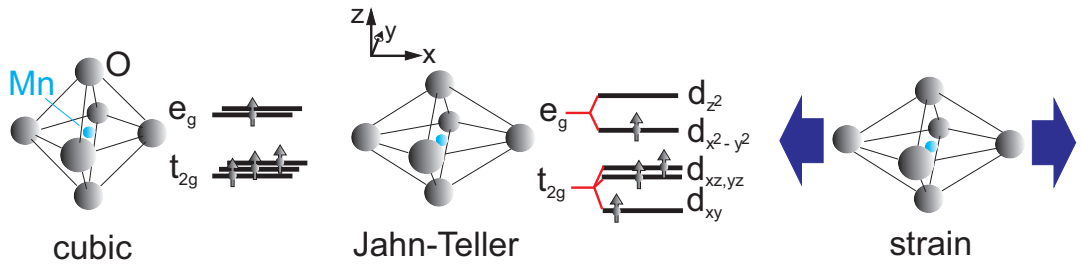

Figure 2.6: Left: For Mn^{3+} in a cubic crystal field the 3d states are split into three degenerate t_{2g} and two degenerate e_g levels. The resulting electronic ground state is a high spin state, where each of the t_{2g} orbitals and one of the e_g orbitals is single occupied. Middle part: The degeneracy of the e_g orbital occupation is lifted by the Jahn-Teller effect, leading to a MnO_6 octahedra distortion. Right: Epitaxial strain has a similar effect favouring the occupation of a certain e_g orbital by lowering the symmetry of the crystal field.

susceptible to changes in the electron concentration or strain-induced structural distortions. Interface charge can affect this distribution and strain can cause rotations of MnO_6 octahedra as well as changes in the Mn-O bond lengths. Strain also has an impact on the orbital occupation. The text presented in the following subsections is partly adapted from the recent publication [52].

2.3.1 Jahn-Teller effect

The structure of LSMO is close to the cubic perovskite. In a cubic crystal field the Mn 3d states are split into three degenerate t_{2g} (d_{xy}, d_{xz} and d_{yz}) and two degenerate e_g levels ($d_{x^2-y^2}$ and $d_{z^2-r^2}$) as depicted in Fig. 2.6 [82, 83]. The e_g orbitals point towards the surrounding negatively charged oxygen ions. Therefore they are higher in energy than the t_{2g} orbitals. In LSMO, the valence of the Mn-ions is Mn^{3+} or Mn^{4+} and, due to Hund's rule coupling, the resulting electronic ground state is a high spin state where each of the t_{2g} orbitals (and in the case of Mn^{3+} one of the e_g orbitals) is single occupied. In a Jahn-Teller active ion such as Mn^{3+} the degeneracy of the e_g orbital occupation is lifted by the Jahn-Teller effect, leading to a MnO_6 octahedra distortion which breaks the e_g symmetry and lowers the energy of the occupied e_g manifold as compared to a Mn^{3+} ion in a cubic crystal field. The configuration with the sub-title 'Jahn-Teller' in Fig. 2.6 shows a tetragonal octahedra distortion that exhibits larger Mn-O distances in the xy-plane. Due to the reduced Coulomb repulsion the $d_{x^2-y^2}$ is lower in energy [82, 73]. Although the t_{2g} orbitals also exhibit a splitting there is no overall energy gain with respect to the degenerate

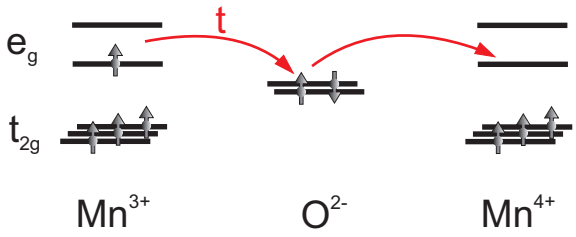

Figure 2.7: Double exchange mechanism for the Mn^{3+}-O^{-2}-Mn^{4+} conduction path favouring parallel spin alignment.

t_{2g} occupation involved.

With increasing Sr doping concentration in LSMO the contribution of Jahn-Teller active ions decreases, since Mn^{4+} is not a Jahn-Teller active ion.

2.3.2 Double exchange mechanism

The double exchange mechanism was originally proposed by Zener [84]. In LSMO, the substitution of La with Sr removes one electron from the Mn cation, leading to a Mn $3d^4$ occupation and acting as hole doping. The simultaneous existence of Mn^{3+} and Mn^{4+} permits conductivity between high-spin states as sketched in Fig. 2.7. The e_g electrons can hop from site to site via an oxygen atom. Since the 2p orbitals of O^{-2} are both occupied, the conduction path involves two hoppings [73]. A delocalization of conduction electrons is energetically favourable, as well as a 3d high spin state. Hence, the double exchange scenario favours a ferromagnetic alignment of neighbouring spins. LSMO with x =0.3 has a ferromagnetic ground state, where magnetism and conductivity are linked [83, 73]. Close to the Curie temperature, spin-charge scattering increases and so does the resistivity [85]. The conduction path Mn^{3+}-O^{-2}-Mn^{4+} and hence ferromagnetism depends sensitively on the Mn-O distance and the Mn-O-Mn bond angle [83, 82].

2.3.3 Strain dependence

Epitaxial strain bears analogy to the Jahn-Teller effect favouring one direction of octahedral distortions as shown in Fig. 2.6 on the right side. Here, the lowering of the symmetry of the crystal field leads to a preferred occupation of the $d_{x^2-y^2}$ orbital. The physics of the doped manganites is governed by the competition between the localizing effect of a strong electron-lattice coupling and the Mn e_g electron

itinerancy leading to ferromagnetism due to double exchange coupling [86]. Millis et al. introduced a model that links the dependence of the Curie temperature T_C in ferromagnetic manganite films to hydrostatic and biaxial strain. Hydrostatic compression (expansion) will increase (decrease) the electron hopping amplitude and thereby reduce (increase) the electron-lattice coupling resulting in higher (lower) T_C values [86]. Volume preserving biaxial or shear strain increases the energy difference between the e_g levels imposed by Jahn-Teller distortion, reinforcing the electron tendency to localize, thus leading to a reduction of the Curie temperature.

Considerable work has explored the strain dependence of manganite thin films [87, 88, 89, 90, 91, 92]. The magnetic properties of manganites in bulk [87] and thin films [88] have been found to be very susceptible to hydrostatic pressure. Also, the substitution of rare-earth cations with different radii acts as a source of chemical pressure, such that larger cation sizes correspond to higher Curie temperatures [93, 94, 95, 96].

Tsui et al. have studied the effects of strain on the anisotropy and Curie temperature of $La_{0.7}Sr_{0.3}MnO_3$ using various substrates resulting in differently strained films [89]. Strain-induced anisotropy typically dominates over the weak magnetocrystalline anisotropy in LSMO [97, 89, 98]. Strain dependent orbital occupation for LSMO (001) grown on different substrates has been investigated employing x-ray linear dichroism [90, 99, 100]: tensile (compressive) in-plane strain favours the occupation of orbitals lying in the surface plane (pointing out-of plane). Besides the use of structural mismatch during growth, the tunability of anisotropy and Curie temperature via electric fields has been the subject of many studies. Thiele et al. reported on piezoelectrically induced biaxial compression in a heterostructure consisting of a thin film of LSMO grown on the relaxor ferroelectric PMN-PT (001) [98]. Changes in T_C as well as in magnetization were detected under an applied electric field, but detected changes did not remain at remanence. Yang et al. observed an in-plane rotation of the magnetic easy axis in LSMO/PMN-PT(x=0.3) (011) due to an electric field [101]. The induced rotation did not remain, once the bias field was switched off. Chapter 5 reports results on the non-volatile magnetic response of LSMO to a piezoelectric PMN-PT (011) substrate that can exhibit two distinct remanent strain states.

So far, a general overview was given explaining the structure and functional properties of the components employed in the heterostructures of chapters 4 to 6. Also, strategies have been outlined to modulate characteristic properties such as the exchange interaction in LSMO or the onset of ferromagnetism in Pd via magnetoelectric coupling. The next chapter introduces the used experimental methods and the

theory behind them.

Chapter 3

Experimental techniques and instrumentation

In this chapter the theoretical basics of the spectroscopy techniques used throughout this thesis, i.e. x-ray absorption spectroscopy (XAS), x-ray magnetic circular dichroism (XMCD) and x-ray natural linear dichroism (XNLD), are explained including approaches to data analysis. The interaction of photons with matter exhibits many channels, the most prominent one in the soft x-ray range is the photoelectric effect related to absorption. At synchrotrons, photon energies can be resonantly tuned to match atom-specific absorption edges. The polarization of the incoming light can be selected, enabling one to obtain information on the properties of the unoccupied states. In XMCD, the intensity difference between left circular polarized x-rays ($c+$) and right circular polarized x-rays ($c-$) is an element sensitive probe of the spin imbalance along the photon propagation direction.[1] Sum rule analysis of the XMCD spectra allow for extraction of the spin and orbital contributions to the total magnetic moment. XAS spectra taken with linearly polarized light contain information on the orbital occupation of the valence states along the x-ray polarization direction. For example, XNLD can shed light on the strain induced orbital occupation in manganite films [90, 99, 100]. In this work, resonant XAS was used as the main tool to probe cross-coupling changes in FM/FE heterostructures. Two complementary detection methods, total electron yield and total fluorescence yield, exhibit distinct probing depths and provide a way to distinguish between interface

[1] Here, for the x-ray polarization the convention is chosen that left handed circular polarized x- rays, denoted as '$c+$', have positive helicity and the photon spin ($+\hbar$) points parallel to the propagation direction. Right handed circular polarized x- rays, denoted as '$c-$', have negative helicity and the photon spin points antiparallel to the propagation direction.

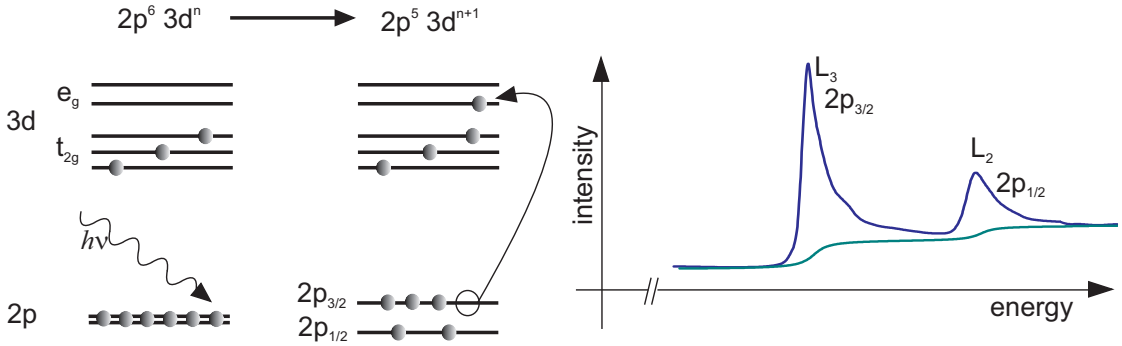

Figure 3.1: Resonant XAS process at the L-edge in the electron configuration picture. In the presence of the core hole the 2p states are spin-orbit split, giving rise to the characteristic XAS line shape with two main peaks at the L-edge.

and bulk signal contributions. Following the explanation of the spectroscopic techniques in section 3.1 to 3.3, details of the instrumentation are given in section 3.4. Since lattice parameter changes play a role in PMN-PT due to its strong piezoelectric response, the XAS measurements are complemented with x-ray diffraction (XRD) reciprocal space maps. This technique is outlined in the last section of this chapter.

3.1 X-ray absorption spectroscopy

In an x-ray absorption process a photon impinging on matter transfers its energy and angular momentum to an electron of a core level that is excited to empty states above the Fermi level. At synchrotron sources the energy of the incoming photons can be tuned to match element specific binding energies of inner atomic shells, e.g. the 2p $\rightarrow$ 3d transitions (so-called L edge) of the transition metals with their partly unfilled 3d orbitals. Hence the XAS process at resonance becomes element specific. Within the configuration picture in Fig. 3.1, an atom is excited from the ground state configuration $2p^6 3d^n$ to a final state configuration $2p^5\ 3d^{n+1}$. While the ground state configuration has a completely filled 2p shell, the final state exhibits a 2p core hole with angular momentum which couples to the spin via spin-orbit coupling. In the presence of the core hole the 2p states are spin-orbit split into $2p_{3/2}$ and $2p_{1/2}$ levels which is observed as a separation of the experimental L-edge XAS spectrum into L_3 and L_2 edges, respectively, as sketched on the right hand side of Fig. 3.1.

Theoretically, the XAS process is described through *Fermi's golden rule*. The transition probability P_{fi} from an initial state $|\psi_i\rangle$ to a final state $|\psi_f\rangle$ with energy

density $\rho(E_f)$ per unit time can be written as [73, 102]

$$P_{fi} = \frac{2\pi}{\hbar} \left|\langle\psi_f|H_{int}|\psi_i\rangle\right|^2 \rho(E_f)\delta(E_f - E_i - \hbar\omega), \tag{3.1}$$

where the δ-function accounts for energy conservation and H_{int} is the time-dependent perturbation that drives the electronic transition. From a classical picture it is intuitive that an electromagnetic wave with electric field $\boldsymbol{E} = \boldsymbol{\epsilon}\ E_0\ e^{-i(\omega\ t\ -\ \boldsymbol{k}\cdot\boldsymbol{r})}$, (with electric polarization $\boldsymbol{\epsilon}$, wave vector $\boldsymbol{k}$ and frequency ω) incident on an electron will set the electron in motion. The electron following the oscillating electric field can be viewed as an induced electric dipole moment oscillating along the direction of $\boldsymbol{E}$. This induced electric dipole moment will in turn re-eradiate electromagnetic waves. In a quantum mechanical treatment it can be shown that the resonant matter-radiation interaction in the *dipole approximation* is described through transition matrix elements of the form

$$P_{fi} \propto \left|\langle\psi_f|\boldsymbol{\epsilon}\cdot\boldsymbol{r}|\psi_i\rangle\right|^2 \rho(E_f)\delta(E_f - E_i - \hbar\omega) \tag{3.2}$$

with a polarization dependent dipole operator $\boldsymbol{\epsilon}\cdot\boldsymbol{r}$. The *dipole approximation* assumes that the electric field driving the electronic transition is constant throughout the atomic volume. This is true within the soft x-ray range, where the wavelength λ (600 eV correspond to $\lambda = 2.1$ nm) is much larger than the radius of a core shell $|\boldsymbol{r}| \approx 0.01$ nm. The transition probability in Eq. (3.2) depends on the propagation direction of the incoming light with respect to the sample coordinate system as well as its electric polarization $\boldsymbol{\epsilon}$. The photon transfers angular momentum $q\hbar$ to the electron, where $q = 0$ refers to linear polarized light while $q = +1$ and $q = -1$ refer to $c+$ and $c-$ circular polarized light. For linear polarization the direction of $\boldsymbol{E}$ determines the XAS intensity, for circular polarized light the angular momentum $\boldsymbol{L_{ph}}$ is aligned parallel or antiparallel to the wave vector $\boldsymbol{k}$. Transitions are allowed for non-vanishing matrix elements in Eq. (3.2) which leads to dipole selection rules between atomic wave functions of the form $|R_{n,l}(r); l, m_l, s, m_\mathrm{s}\rangle$ [73]:[2]

$$\begin{aligned} \Delta l &= \pm 1, \\ \Delta m_l = q &= 0, \pm 1, \\ \Delta s &= 0, \\ \Delta m_\mathrm{s} &= 0, \end{aligned} \tag{3.3}$$

[2]here, $R_{n,l}$ denotes the radial component of a shell n with orbital quantum number l, s is the spin quantum number. m_l is the magnetic quantum number ranging from $-l$ to l in integer steps and m_s is the spin projection quantum number ranging from $-s$ to s in integer steps.

Here the polarization and geometry dependence of Eq. (3.2) can be exploited to study properties of the density of empty states that give rise to dichroism.

3.2 X-ray magnetic circular dichroism

Besides elemental and chemical specificity, resonant XAS opens the possibility to study polarization-dependent properties of the 3d electrons, such as magnetism. In XMCD the intensity difference between $c+$ and $c-$ polarized light is an element sensitive probe of the magnetization $\boldsymbol{M}$ along the photon propagation direction.

$$\Delta I_{XMCD} = I^{c+} - I^{c-} = I^{\uparrow \boldsymbol{L_{ph}} \uparrow \boldsymbol{M}} - I^{\downarrow \boldsymbol{L_{ph}} \uparrow \boldsymbol{M}} \tag{3.4}$$

The arrows denote the alignment of the photon angular momentum $\boldsymbol{L_{ph}}$ and $\boldsymbol{M}$ with respect to each other. Equation 3.4 shows that an equivalent dichroism value can be obtained by keeping the light polarization constant and reversing the direction of the magnetization. Fig. 3.2 (a) shows an example of XAS spectra taken with $c+$ and $c-$ polarized light at the Co $L_{3,2}$ edge with a magnetic field of 2T applied along the beam direction. The resulting difference spectrum arising from preferential spin alignment in cobalt is shown in 3.2 (b).

3.2.1 Quantum mechanical origin of the XMCD effect

The XMCD absorption difference can be explained within a two-step model [73]. In a first step the non-vanishing matrix elements of Eq. (3.2) obeying the dipole selection rules in Eq. (3.3) favour a preferential spin polarization that depends on the sign of the photon angular momentum transfer $\pm q\hbar$. In the following, the spin polarization dependence is outlined for 2p $\rightarrow$ 3d transitions.

Table 3.1 contains the relevant angular 2p spin-orbit coupled initial state wave functions $|l, m_l, j, m_j\rangle = C_{m_l, m_s; j, m_j} |l, m_l, s, m_s\rangle$ that are here expressed in linear combinations of the atomic wave functions $|l, m_l, s, m_s\rangle$ [73, 103], where the C_{m_l, m_s} are the *Clebsch-Gordon Coefficients* [104, 105]. Evaluation of the angular part of the dipole matrix elements for $c+$ polarized light

$$\langle l+1, m_l+1 | {C_1}^1 | l, m_l \rangle = \sqrt{\frac{(l+m+2)\cdot(l+m+1)}{2(2l+3)\cdot(2l+1)}}, \tag{3.5}$$

and for $c-$ polarized light, respectively,

$$\langle l+1, m_l-1 | {C_{-1}}^1 | l, m_l \rangle = \sqrt{\frac{(l-m+2)\cdot(l-m+1)}{2(2l+3)\cdot(2l+1)}} \tag{3.6}$$

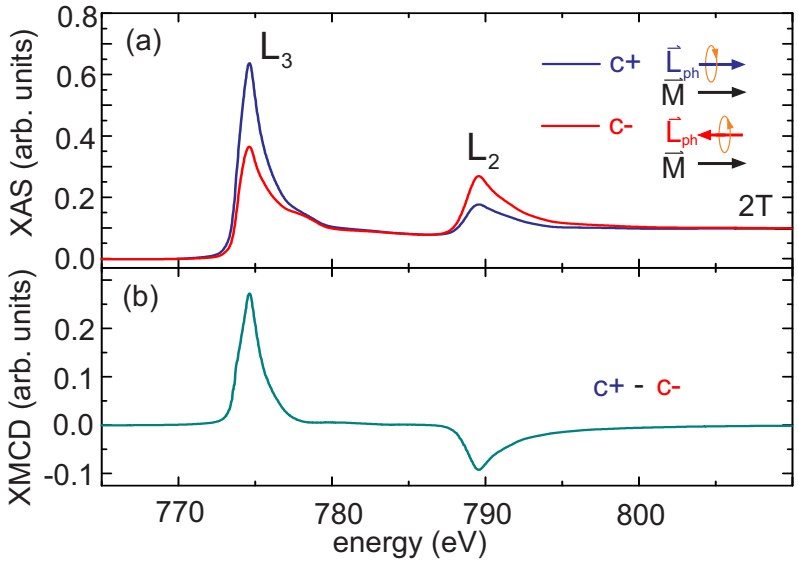

Figure 3.2: (a) XAS spectra at the Co $L_{3,2}$ taken with $c+$ ($c-$) circular polarized light, where the photon angular momentum and the magnetization of the sample are aligned in parallel (antiparallel). The corresponding XMCD difference spectrum is shown in (b).

gives the transition probabilities for spin up and spin down states [73].

Table 3.1 lists the non-vanishing contributions. Hence, a photon momentum transfer of $+q\hbar$ results in a preferential excitation ∼62.5% of spin-up electrons compared to the number of excited spin-down electrons ∼37.5% at the L_3 edge. At the L_2 edge a momentum transfer of $+q\hbar$ yields an excitation ∼75% of spin-down electrons and ∼25% of spin-up electrons. For a photon momentum transfer of $-q\hbar$ the situation is reversed with a preferential excitation of ∼62.5% of spin-down electrons and a minor excitation of spin-up electrons ∼37.5% at the L_3 edge; at the L_2 edge 75% spin-up electrons and ∼25% spin-down electrons are excited. In the photon absorption process the angular momentum is conserved and transferred to the photoelectron spin via spin-orbit coupling. Since $2p_{1/2}$ and $2p_{3/2}$ have opposite spin-orbit coupling, photoelectrons originating from those edges exhibit opposite spin polarizations with respect to each other. As visualized in the sketch of the two-step model in Fig. 3.3, the angular momentum transfer acts as a spin polarized source in the excitation process. In a second step vacant exchange-split spin-up and spin-down bands act as spin-sensitive 'detectors'. Thus, the detected dichroism stemming from the exchange splitting of the empty bands is indirectly connected to the magnetization arising from the spin imbalance in the filled bands.

Table 3.1: Preferential spin polarization caused by a photon momentum transfer $\pm q\hbar$ in the transition probability Eq. (3.1). The angular 2p spin-orbit coupled initial state wave functions $|l, m_l, j, m_j\rangle$ are written as linear combinations of the atomic wave functions $|l, m_l, s, m_\mathrm{s}\rangle$ with Clebsch-Gordon Coefficients C_{m_l,m_s}. The $2p_{3/2}$ and $2p_{1/2}$ levels act as spin polarized sources.

$\|l, m_l, j, m_j\rangle$ basis		$\|l, m_l, s, m_\mathrm{s}\rangle$ basis	transition probability	
j	m_j	$\|m_l, m_\mathrm{s}\rangle$	$+q\hbar$	$-q\hbar$
$\frac{3}{2}$	$+\frac{3}{2}$	$\|+1,\uparrow\rangle$	$\frac{2}{5}\uparrow$	$\frac{1}{15}\uparrow$
	$+\frac{1}{2}$	$\sqrt{\frac{2}{3}}\|0,\uparrow\rangle + \sqrt{\frac{1}{3}}\|+1,\downarrow\rangle$	$\frac{2}{15}\uparrow + \frac{2}{15}\downarrow$	$\frac{2}{15}\uparrow + \frac{1}{45}\downarrow$
	$-\frac{1}{2}$	$\sqrt{\frac{1}{3}}\|-1,\uparrow\rangle + \sqrt{\frac{2}{3}}\|0,\downarrow\rangle$	$\frac{1}{45}\uparrow + \frac{2}{15}\downarrow$	$\frac{2}{15}\uparrow + \frac{2}{15}\downarrow$
	$-\frac{3}{2}$	$\|-1,\downarrow\rangle$	$\frac{1}{15}\downarrow$	$\frac{2}{5}\downarrow$
$\frac{1}{2}$	$+\frac{1}{2}$	$-\sqrt{\frac{1}{3}}\|0,\uparrow\rangle + \sqrt{\frac{2}{3}}\|+1,\downarrow\rangle$	$\frac{1}{15}\uparrow + \frac{4}{15}\downarrow$	$\frac{1}{15}\uparrow + \frac{2}{45}\downarrow$
	$-\frac{1}{2}$	$-\sqrt{\frac{2}{3}}\|-1,\uparrow\rangle + \sqrt{\frac{1}{3}}\|0,\downarrow\rangle$	$\frac{2}{45}\uparrow + \frac{1}{15}\downarrow$	$\frac{4}{15}\uparrow + \frac{1}{15}\downarrow$

3.2.2 Sum rules

In XMCD, quantitative values for the orbital and spin moment m_orb and m_s in units of μ_B/atom can be determined from the analysis of the XAS and XMCD spectra using the following *sum rules* [106, 107, 108],

$$m_\mathrm{orb} = -\frac{4\int_{L_3+L_2}(\mu_+ - \mu_-)d\omega}{3\int_{L_3+L_2}(\mu_+ + \mu_-)d\omega}(10 - n_{3d}) \tag{3.7}$$

$$m_\mathrm{spin} = -\frac{6\int_{L_3}(\mu_+ - \mu_-)d\omega - 4\int_{L_3+L_2}(\mu_+ - \mu_-)d\omega}{\int_{L_3+L_2}(\mu_+ + \mu_-)d\omega}(10-n_{3d})\left(1 + \frac{7\langle T_z\rangle}{2\langle S_z\rangle}\right)^{-1} \tag{3.8}$$

where μ_+, μ_- denote the XAS spectra taken with $c+$ and $c-$ polarized light. The electron occupation number in the valence band n_{3d} has to be known from other experiments or calculations. The indices L_3 and L_2 refer to the energy integration over the respective edges. $\langle S_z\rangle$ is the expectation value of the spin moment projection along the beam direction, $\langle T_z\rangle$ is the expectation value of the intra-atomic magnetic dipole operator term $\boldsymbol{T} = \boldsymbol{S} - 3\boldsymbol{r}(\boldsymbol{r}\cdot\boldsymbol{S})$. The latter provides a measure of the anisotropy of the field of the spins, when the atomic cloud is distorted by crystal-field effects or spin-orbit interaction [109] (see below). Figures 3.4 and 3.5 show the determination of the integral spectral values required for the sum rules at the Co and Mn $L_{3,2}$ edges. A baseline (green line) was subtracted from the XAS spectra in

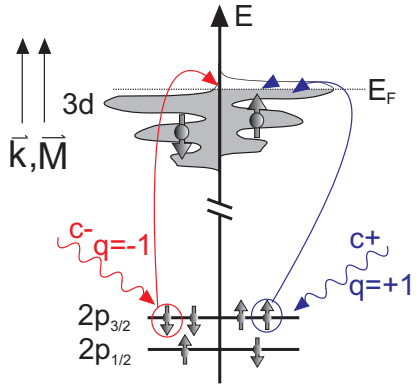

Figure 3.3: Two-step model of XMCD. In the first step of the excitation process the spin-orbit split core levels act as a spin polarized source depending on the helicity of the incoming photons. At the L_3 edge $c+$ ($c-$) polarized light excites preferentially spin-up (spin-down) electrons. In the second step, the exchange split valence band acts as spin-sensitive detector. The oppositely pointing spins at the $2p_{1/2}$ level remind of the reversed situation at the L_2 edge, where $c+$ ($c-$) polarized light excites preferentially spin-down (spin-up) electrons.

Fig. 3.4 (a) and 3.5 (a) to effectively remove contributions from excitations in higher order unoccupied d states. The step function subtracted at the L_3 edge (L_2 edge) represents 2/3 (1/3) of the complete edge jump in analogy to the degeneracy of the initial states $L_3/L_2 \sim 4/2$. The dotted line in Fig. 3.4 (b) and 3.5 (b) separates the integration intervals assigned to the L_3 edge and the L_2 edge, respectively. This separation is justified at the Co edge with well separated core spin-orbit multiplets in the final state, see Fig. 3.4 (b). Towards the early transition metals[3] other interactions including core-valence Coulomb interactions become comparable in strength leading to a mixing of both the L_3 and L_2 edges [110]. Multiplet calculations can be used to correct for the deviation in the spin sum rule. The integration curves in Fig. 3.5 (b) obtained at the Mn edge in an $La_{0.67}Sr_{0.33}MnO_3$ thin film show an example where the spin-orbit splitting is not sufficiently large. A correction factor is estimated using charge-transfer multiplet calculations [111]. With a nominal ratio of $Mn^{3+}/Mn^{4+}= 2/1$ in $La_{0.67}Sr_{0.33}MnO_3$ the calculations involve two ground states $2p^63d^3+2p^63d^4\underline{L}$ and $2p^63d^4+2p^63d^5\underline{L}$, where $\underline{L}$ denotes a ligand hole. A comparison of the calculated expectation value $\langle S_z^{calc}\rangle$ of the spin moment given by the program with the value $\langle S_{z,eff}^{SR}\rangle$ derived from the calculated XAS and XMCD spectrum using the sum rule of Eq. 3.8 results in a correction factor of $\frac{\langle S_z^{calc}\rangle}{\langle S_{z,eff}^{SR}\rangle} = 1.52$.

[3]The spin-orbit coupling decreases with decreasing atomic number.

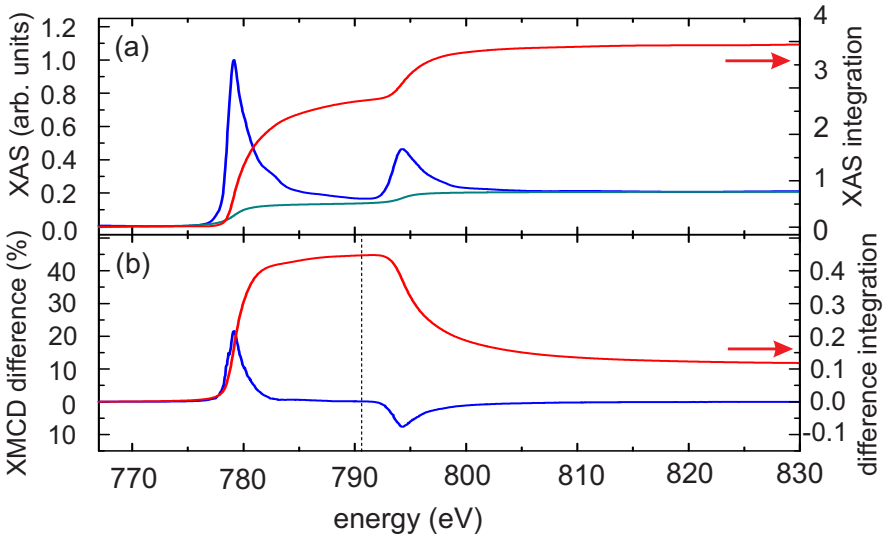

Figure 3.4: Sum rules analysis of (a) the XAS and (b) the XMCD spectra at the Co $L_{3,2}$ edge. Red lines show the integrated area of each spectrum (blue). The integrated XAS spectrum was corrected by the subtraction of a baseline (green).

So far, the magnetic dipole operator term $\langle T_z \rangle$ has been omitted. Since the absorption process in Eq. 3.2 is orientation and polarization dependent, anisotropies of charge and spin can be probed. An anisotropy in charge can arise for example at interfaces or surfaces where the coordination number of the absorbing atom changes abruptly. Anisotropic strain can also cause a preferential occupation of certain orbitals [103]. Mathematically, an anisotropic charge distribution can be written in a multipole expansion. Figure 3.6 (a) shows an example, where an aspheric charge distribution is represented through a monopole and an additional quadropole. The latter one can be described by a quadropole tensor $Q_{\alpha\beta}$ [112] where

$$Q_{\alpha\beta} = \delta_{\alpha\beta} - 3r_\alpha r_\beta / r^2. \tag{3.9}$$

with $Q_{\alpha\beta} = Q_{\beta\alpha}$ and $\sum_\alpha Q_{\alpha\alpha} = 0$. In analogy to the charge anisotropy example the magnetic dipole operator term $\langle T_z \rangle$ reflects an anisotropic spin distribution due to an anisotropic charge distribution around the absorbing atom or due to spin-orbit interaction. Stöhr and König [112] rewrite the magnetic dipole operator in terms of the charge quadropole tensor from Eq. 3.9

$$T_\alpha = \sum_\beta Q_{\alpha\beta} S_\beta \tag{3.10}$$

where the spin quantization axis is aligned along α, indicating the coupled charge

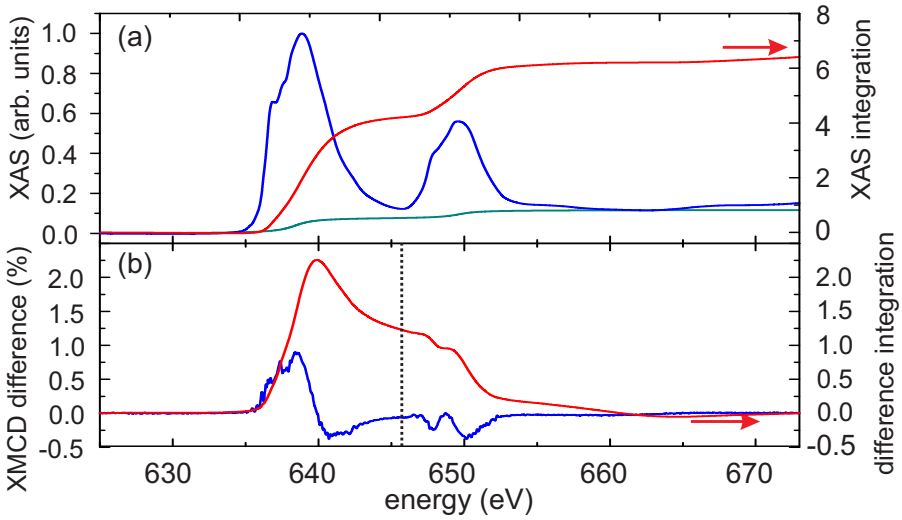

Figure 3.5: Sum rules analysis of (a) the XAS and (b) the XMCD spectra for LSMO at the Mn $L_{3,2}$ edge. Red lines show the integrated area of each spectrum (blue). The integrated XAS spectrum was corrected by the subtraction of a baseline (green).

and spin components of T. To evaluate the sum rule Eq. 3.8, $\langle T_z \rangle$ has to be known, and in thin films the contribution might not be negligible. However, DFT calculations [113] for the Co thin film measured in chapter 6 give a negligible $\langle T_z \rangle$. For the LSMO thin film of chapter 5 XMCD measurements in saturation along three perpendicular directions result in the same spin moment. Since the vanishing trace of $Q_{\alpha\beta}$ implies that angular averaging over three perpendicular crystal directions cancels contributions of $\langle T_z \rangle$ in the sum rule Eq. 3.8, a $\langle T_z \rangle$ contribution induced by an anisotropic charge can be excluded. There could be a $\langle T_z \rangle$ term related to spin-orbit coupling[4]. For weak spin-orbit coupling this effect can be neglected [112].

3.3 X-ray natural linear dichroism

XNLD calculated as the intensity difference between spectra measured with linear horizontal (LH) and linear vertical (LV) polarized light arises due to an anisotropy of the valence charge distribution along the respective directions, as sketched in

[4]If the spin moment is aligned along a preferred direction, the charge distribution might also be altered due to spin-orbit coupling. When probing an angular dependence the spin-quantization axis will rotate with the external magnetic field and so will the charge distribution and ultimately $\langle T_z \rangle$. Then $\langle T_z \rangle$ will always contribute to the effective spin moment.

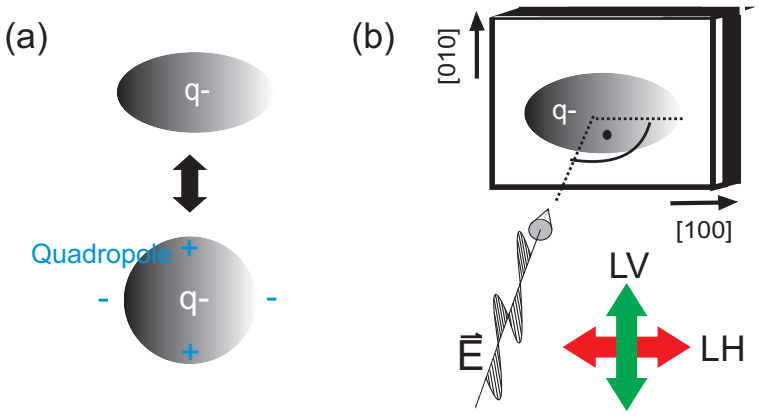

Figure 3.6: (a) A uniform aspherical charge distribution is equivalent to a sphere and a charge quadropole. (b) Explanation of the XNLD difference $LH - LV$ due to an asymmetric charge distribution. The $\boldsymbol{E}$-field vector of the incoming photon acts as a search light with respect to the unoccupied density of states.

Fig. 3.6 (b). The *search-light effect* [102] provides a simple picture of the XNLD process. The electric field vector $\boldsymbol{E}$ acts as a search-light probing the occupation of the valence orbitals along $\boldsymbol{E}$. The transition probability is proportional to the number of empty states along the $\boldsymbol{E}$ field direction.

XNLD proves to be a valuable technique to study the strain dependent orbital occupation for LSMO (001) grown on different substrates [90, 99, 100]: In LSMO, a tensile (compressive) in-plane strain favours the occupation of orbitals lying in the surface plane (pointing out-of plane).

3.3.1 MultiX multiplet calculations

Multiplet calculations allow one to relate the energy and polarization dependence of experimental XAS spectra to the properties of crystal field atomic multiplets [114]. The energy levels of the electrons in an open shell form multiplets under the effect of the electron-electron interaction, the spin-orbit coupling, and the crystal field [114].The code multiX [114] employed in this thesis facilitates the study of spectroscopic effects arising from low symmetry environments. The ground state and core hole state giving rise to the multiplet structure are determined for a given crystal field, which is constructed explicitly from the positions of neighboring point charges interacting with the open shells of the considered Mn atom.

In section 5.1.4, multiplet calculations are used to investigate the influence of biaxial in-plane strain on XNLD spectra of LSMO thin films. For ferromagnetic

LSMO $x = 0.33$, the crystal field is introduced by an xyz-coordinate file containing the positions and charges of surrounding La (Sr), Mn and O atoms in rhombohedral symmetry [115]. This point charge crystal field is then scaled by 1.7 to obtain a better agreement with the data. As the elements La and Sr inhabit nominally the same positions in the crystal lattice, $LaMnO_3$ and $SrMnO_3$ coordinate files are treated separately in the calculations. XNLD spectra are calculated for $LaMnO_3$ with a Mn^{3+} configuration (ground state $2p^6\ 3d^4$), as well as for $SrMnO_3$ with a Mn^{4+} configuration (ground state $2p^6\ 3d^3$). Note that the XNLD of the latter is about 4 times smaller, because Mn^{4+} with a half-filled t_{2g} triplet and unoccupied e_g orbitals is not a Jahn-Teller active ion.

The resulting XNLD spectra are weighted according to the doping concentration of LSMO $x = 0.33$. The best agreement between calculation and experiment in chapter 5.1.4 was obtained with the following parameters: The Coulomb interaction was set to 0.8. The 2p spin-orbit coupling defines the separation between the L_3 and L_2 edges and the atomic value was used. The 3d spin orbit coupling was set to zero, justified by the negligible orbital moment obtained from sum rules analysis, see section 5.1.2. A Boltzmann distributed population of the initial states reflects the experimental temperature setting of about 300 K. A core-hole lifetime broadening of 0.3 was set for the L_3 edge, it was linearly increased from 0.3 to 0.4 over the L_2 edge.

3.4 Instrumentation

The soft XAS and XMCD measurements in chapters 4-6 were carried out at the X-Treme beamline [116] at the Swiss Light Source, Paul Scherrer Institut (Switzerland) and at beamline 6.3.1 [117] at the Advanced Light Source, Lawrence Berkeley National Laboratory (California, USA). The hard XAS measurements in chapter 4 where conducted at the PHOENIX beamline [118] at the Swiss Light Source, Paul Scherrer Institut (Switzerland).

3.4.1 X-ray absorption spectroscopy beamlines

X-Treme and PHOENIX are equipped with an elliptically polarizing undulator that allows for switching of the x-ray helicity to obtain XMCD spectra. X-Treme operates in the soft x-ray regime, 400-1800 eV. For the energies used in this thesis the degree of circular polarization at the first harmonic is 100%. The beam spot size has a width of 220 μm, while the height is defined by an adjustable exit slit (usually 20-30 μm). These settings were used for the nanostructured samples of chapter 4 with

dimensions between 200×260 μm^2 and 90×100 μm^2. The thin film measurements were taken with a defocused beam to average over many domains. The X-Treme endstation has a base pressure in the low 10^{-11} mbar range, a pumped ^{4}He cryostat with separated 1 K pot which allows one to reach temperatures down to 2 K. The end-station contains a superconducting vector-magnet that allows one to apply 7 T parallel to the beam direction and 2 T perpendicular to it in the horizontal plane. The remanent field ranges from 40 to 100 Oe, depending on the magnet's field history. Electrical switching of FE layers was done in-situ in the endstation. At X-Treme, the detection methods used included total electron yield (TEY) and total fluorescence yield (TFY) mode [102, 73]. The energy scans were obtained in on-the-fly mode, i.e. monochromator and insertion device are scanned continuously and simultaneously.

The PHOENIX beamline, equipped with a two-crystal monochromator, covers the energy range from 800-8000 eV. For the measurements at the Pd L edge in chapter 6 the fifth harmonic was used with a polarization degree of 80%. The beam spot size was 150 μm x 100 μm. The pressure in the endstation was in the low 10^{-7} mbar range and a closed cycle ^{4}He cryostat reached down to 65 K. Also at PHOENIX, the electrical switching of FE layers was done in-situ. A permanent magnet of 0.45 T was mounted on the sample holder with the sample attached on top. The XAS spectra were detected in TFY mode 3° off normal incidence.

Beamline 6.3.1 covers the energy range from 200 eV to 2000 eV. The bending magnet source with an aperture mounted above the orbit provides elliptically polarized radiation with a polarization degree of 65%. The aperture was fixed, therefore dichroism was probed by reversing the magnetization of the sample leading to an antiparallel or parallel alignment of $\boldsymbol{k}$ and $\boldsymbol{M}$. Hysteresis curves were obtained as the ratio of loops taken at the L_2 and L_3 edge, respectively. At beamline 6.3.1 only room temperature measurements were conducted. The endstation pressure was in the 10^{-9} mbar range. Magnetic fields were applied collinear to the incoming x-ray beam using an electromagnet of up to 2 T, which is advantageous in terms of the ramping velocity and low remanent field, which enabled us to monitor the small hysteresis openings in chapter 6. Electrical switching of FE layers was done in-situ.

An XAS process can be probed by monitoring the follow-up de-excitation processes. When created core holes are filled by outer shell electrons, the energy needs to be conserved. This de-excitation process is therefore accompanied by the emission of Auger electrons and fluorescent photons. The de-exitation channels in XAS are proportional to the absorption cross-section. The x-ray absorption cross-section is energy dependent and increases strongly at an absorption edge. The three most common types of detection are transmission, TEY and TFY. Measuring the transmission of x-rays through a sample by comparing the beam intensity before (I_0) and after the

sample (I) via grids and photodiodes, respectively, would be the most direct method of detection [119]. However, with ferroelectric substrates of thicknesses ~ 0.5 mm used in chapters 4 to 6, the transmission of soft x-ray photons is negligible. Hence the detection methods used in this thesis were restricted to TEY and TFY. First, the probing depth in TEY will be described, following the description given by Stöhr [102, 73].

The photon mean free path in the soft x-ray range in the solid state is on the order of 1000 Å. The created Auger- and photoelectrons responsible for the TEY signal obey the universal curve, which states that the electron mean free path is mainly a function of kinetic energy. For energies corresponding to the soft x-ray range the electron mean free path is typically less than 10 Å. Hence, the Auger electrons trigger a low energy electron cascade through inelastic scattering processes (electron-electron, electron-plasmon and electron-phonon) on their way to the surface. Once the surface is reached, all those electrons contribute to the TEY signal who can overcome the surface potential barrier. The TEY is dominated by low energy electrons with kinetic energy below about 20 eV. One can show [102] that the TEY contribution from buried layers falls off exponentially with their distance from the surface. The electron sampling depth λ_e constitutes the depth at which the intensity contribution of a buried layer reaches 1/e with respect to the surface. It was found to be about 2 nm for Ni, Fe and Co metals [120]. The above described processes limit the probing depth in TEY detection to about 20-130 Å depending on material characteristics such as conductivity.

If the incidence angle of the x-rays with respect to the sample surface is too shallow, all x-rays are absorbed within a layer close to the surface. As a consequence, all incident photons will generate electrons that escape the sample and the energy dependent modulation is lost [121]. The TEY is not proportional to the XAS absorption coefficient anymore and such saturation effects need to be taken into account. To prevent saturation in our experiments, we used incidence angles from 0° to 60° with respect to the surface normal.

TFY [122] is a radiative de-excitation process. Due to the large mean free path, the fluorescent photons interact less strongly with matter as compared to electrons, resulting in a higher probing depth. A drawback in TFY is the strong geometry dependence that restricts the proportionality to the XAS absorption coefficient. Also, the photons can be reabsorbed on their way to the surface. If the x-rays enter at a grazing incidence geometry and the fluorescent photons are measured perpendicular to the surface, nearly all generated fluorescence photons will be able to escape out of the sample into the detector, therefore the detected signal is independent of the x-ray absorption coefficient. In the case of not too thick films, in normal-incidence and

grazing detection the signal becomes more and more proportional to the absorption coefficient. The absorption of the generated fluorescence radiation on the way out of the sample attenuates the fluorescence radiation. If the absorption coefficient of the sample is high, most fluorescence radiation detected arises from the region close to the surface; consequently the detected signal is high. If the absorption coefficient is low, the deeper substrate region contributes more to the fluorescence and the detected signal is lower [123]. For the TFY spectra on Co/PMN-PT in chapter 6, a comparison of TEY and TFY gave an error of 10% in the determination of the magnetic moment for the respective geometry used, which is well within the error bars of the sum rule procedure. XAS spectra of both TEY and TFY are normalized to the detected I_0 signal of a gold grid (with no absorption edges in the energy range of interest) mounted in front of the endstation to normalize out changes in photon flux (flux decay and top-up mode of the ring; also, the insertion device and bending magnets don't have the same flux at all energies). At PHOENIX, the XAS was measured in partial fluorescence yield (PFY) mode, where an energy selective detector is used [121]. Hence the normalization on an I_0 originating from a gold grid can be replaced by a normalization using a non-resonant fluorescence signal from another energy interval stemming from other elements present, for example in the capping layer or the substrate. This normalization method also accounts for any beam movements (crucial for small nanostructures) as the I_0 fluorescence originates from the sample and is measured with the same detector.

3.5 X-ray diffraction - reciprocal space maps

Strain induced changes in voltage dependent XAS and XMCD measurements are complemented by x-ray diffraction reciprocal space maps (RSM) that monitor voltage dependent lattice parameter changes in PMN-PT (see chapter 5). XRD is a powerful tool to investigate the crystalline structure of materials, thanks to x-ray wavelengths that are comparable to inter-atomic distances. The XRD was performed with a Rigaku SmartLab four-circle diffractometer (Cu K_α radiation). The OOP lattice spacing is obtained from a symmetric coupled $2\theta - \omega$ scan; the geometry is sketched in Fig. 3.7 (a). For parallel (hkl) planes with spacing d_{hkl}, constructive interference occurs only when Bragg's law is fulfilled:

$$n \cdot \lambda = 2 \cdot d_{hkl} \cdot sin\theta \tag{3.11}$$

By changing ω and 2θ in a coupled manner (i.e. if ω increases by 1°, 2θ increases by 2°) one scans along the direction of the normal to the set of planes that bisects

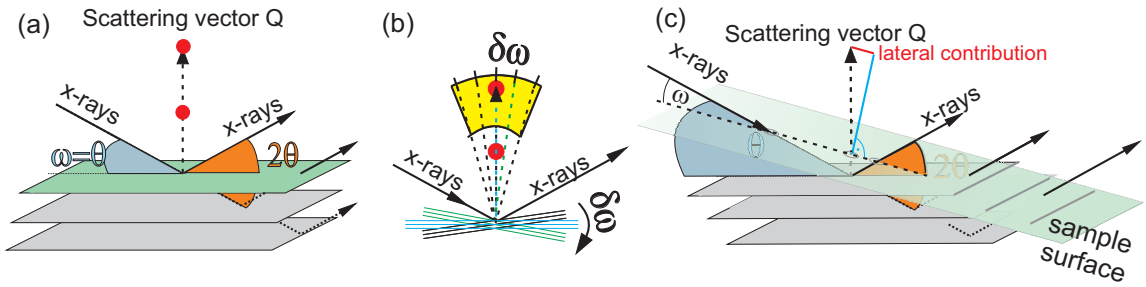

Figure 3.7: (a) Bragg condition for parallel (hkl) planes with spacing d_{hkl}, when searching for a symmetric reflection. (b) A reciprocal space map consists of coupled scans, where each one has a slightly different offset that is induced by tilting the sample. Hence one scans the yellow area by rotating the normal with respect to different sets of planes through the detection geometry setting, which is defined by x-ray source and detector. (c) Mapping an asymmetric reflection with different coupled scans gives also information on the lateral contribution to the scattering vector Q and the in-plane lattice parameter.

the incident and diffracted x-ray beams. Eventually, the chosen θ-2θ values detect Bragg reflections corresponding to constructive interference (represented by the red dots). For the symmetric scan in Fig. 3.7 (a) ω equals θ.

A reciprocal space map consists of a collection of coupled scans with slightly different sample tilts, as indicated in Fig. 3.7 (b) by the yellow area. ω has a small varying offset such that $\omega = \theta + \delta\omega_{offset}$. Apart from the offset, ω and 2θ are again coupled.

In order to scan an asymmetric reflection from a particular set of planes, as shown in Fig. 3.7 (c), the crystal is again tilted such that the normal to the set of planes bisects the incident and diffracted x-ray beams. From Fig. 3.7 (c) it is clear, that the probe of such an asymmetric reflection gives also information on IP lattice parameters, as the Q vector has an in-plane component (indicated by the red line) with respect to the surface. For (011) oriented PMN-PT in section 5.1.3, the in-plane lattice parameters along $(01\bar{1})$ and (100) can be extracted from RSMs around the asymmetric $(\bar{2}22)$ and (031) Bragg peaks of the PMN-PT substrate.

Chapter 4

Charge modulation at the Pd/PZT interface

As outlined in chapter 2.2.1, palladium is paramagnetic (PM) with a Stoner parameter slightly short of fulfilling the condition for ferromagnetism by about 10 % [55, 56]. The prospect of shifting the Fermi level to slightly lower energies motivated recent proposals for the electrostatic control of magnetism in Pd [62, 64]. Here, a modulation of the charge carrier density via an adjacent FE PZT layer was envisaged. From the discussion in section 2.2.1 it is clear that the onset of ferromagnetism depends crucially on the exact shape of the density of states close to the Fermi level. No calculations or growth studies for Pd/PZT exist. In this chapter a first experimental approach for verification of the prediction is described. The next subsection describes the sample preparation following the reports on epitaxial growth for Pd/$SrTiO_3$ [124, 61]. XAS and XMCD measurements on the Pd/PZT device structures upon switching are presented in subsections 4.1.2 and 4.1.3 for the Pd $M_{3,2}$ and $L_{3,2}$ edges, respectively. Unfortunately, no conclusive results were achieved.

4.1 Results

4.1.1 Sample fabrication

Au/Pd/PZT/LSMO/Ti/$SrTiO_3$(001) nanostructures were prepared in a three-step e-beam lithography process[1]. An optical microscope image of the device structure is shown in Fig. 4.1 (a). The blue rectangle marks the active switchable area of a

[1]Lithography was done by Carlos Vaz, Paul Scherrer Institut, Switzerland.

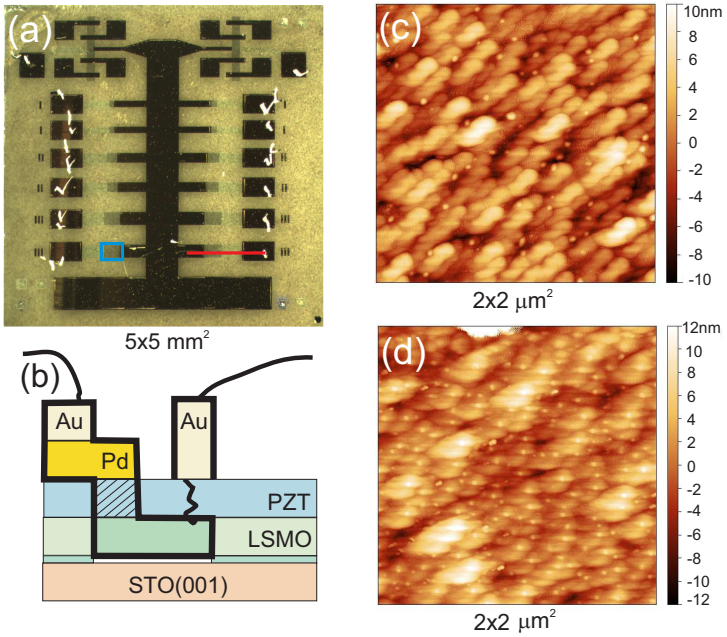

Figure 4.1: (a) Optical microscope image of the device structure. The blue rectangle marks a switchable Pd/PZT pad. A schematic cross section along the red line is shown in (b) clarifying the underlaying conduction path between the two electrodes. Only the shaded part of PZT is electrically switchable. (c) AFM picture of the PZT surface on top of conducting LSMO. (d) The AFM picture of the surface of 4nm Pd grown on PZT/conducting LSMO shows continuity between islands.

device. The conduction path becomes more clear by looking at the cross section along the red line illustrated in Fig. 4.1 (b). Positive photoresist is spin coated on a $SrTiO_3$ (001) (STO) substrate. After electron beam lithography exposure and development, a TiO layer is grown as a mask layer. After removal of the photoresist, 15 nm LSMO with $x = 0.35$ doping and 200 nm $Pb(Zr_{0.2}Ti_{0.8})O_3$ were grown by off-axis magnetron sputtering[2]. On top of the TiO_x layer LSMO grows amorphous, while the uncovered areas of the STO induce growth of single crystalline conducting LSMO and serve as the bottom contact. An atomic force microscopy (AFM) picture in Fig. 4.1 (c) shows the PZT surface on top of conducting LSMO. Following a second lithography step, Pd is deposited on top of the PZT by thermal evaporation. Test samples with Pd grown at room temperature resulted in discontinuous thin films. Hence, the procedure outlined in reference [124] for the Pd/STO system was employed to induce epitaxial growth of Pd on PZT, as the lattice mismatch (3.93Å-

[2]Collaboration with M. S. J. Marshall, Yale University, New Haven, USA.

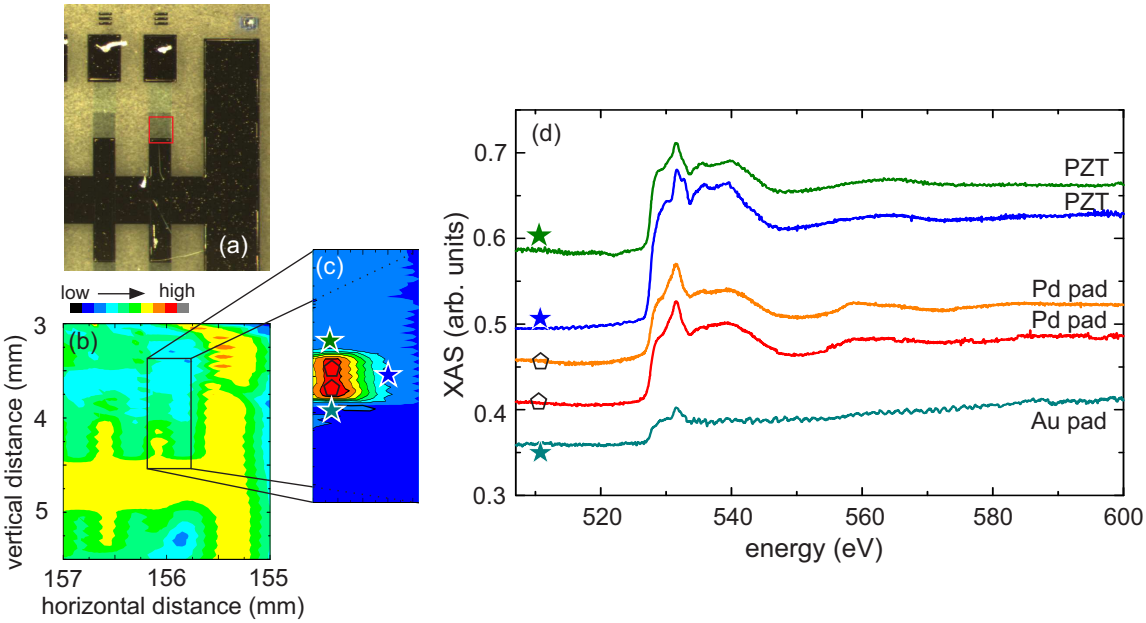

Figure 4.2: (a) Optical microscope image of the device structure. The red rectangle marks the area of a switchable Pd/PZT/LSMO pad. (b) X-ray absorption 2D scan of the same sample region taken at 531 eV with TEY. (c) 2D scan monitoring the photocurrent at the back electrode upon scanning the sample surface with the X-ray beam. The red area corresponds to the Pd/PZT/LSMO pad. (d) Pd M_3 edge/O K edge XAS spectra for different areas on and off the Pd pad.

3.89Å)/3.89Å= 1% for Pd/PZT is only slightly higher than for the Pd/STO (001) system with (3.905Å-3.89Å)/3.89Å=0.4%. After soft sputtering of the PZT surface with Ar and outgassing at elevated temperatures 300 °C to remove contaminations from the surface, 1 nm Pd was grown at 250° C to induce cube-on-cube epitaxial single crystalline growth followed by 3 nm Pd grown at room temperature and in-situ annealing at 300° C. AFM data of a Pd pad in Fig. 4.1 (d) suggest continuity between the islands. In a third lithography step Au contacts are deposited and the conducting LSMO film is connected as a bottom electrode through surface scratches. Only the shaded part of the PZT in Fig. 4.1 (b) is switchable. Three different contact size areas have been tested, 200×260 μm^2, 180×150 μm^2 and 90×100 μm^2, for Pd layers with thicknesses of 3 nm and 4 nm.

4.1.2 XAS and XMCD at the Pd M edge

To test the prediction of the onset of ferromagnetism in Pd, XAS and XMCD measurements at the Pd $M_{3,2}$ edges were carried out for Pd (3 nm)/ PZT and

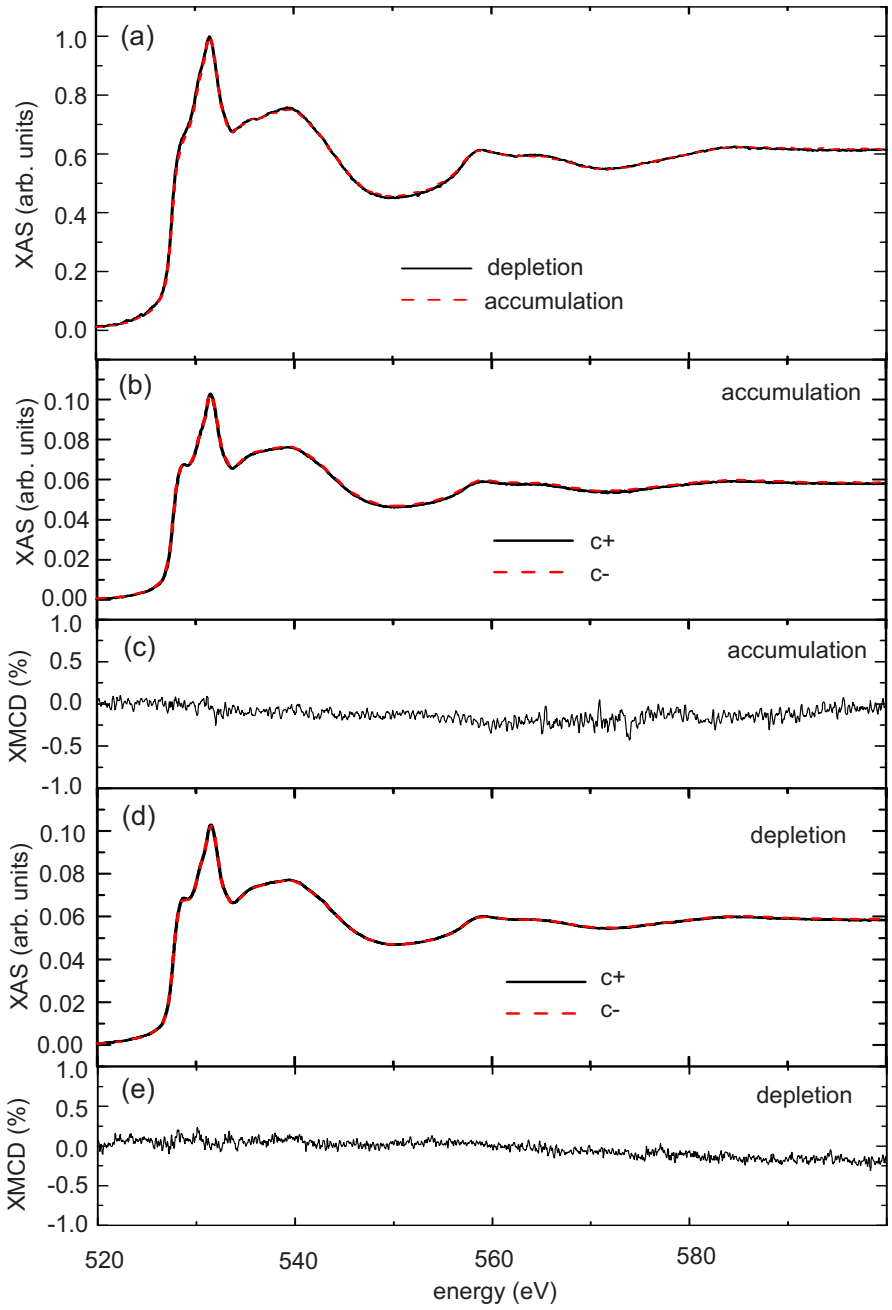

Figure 4.3: (a) Pd M_3 edge XAS spectra taken in normal incidence under a magnetic field of 6.5 T at 2 K for opposite FE polarization states corresponding to electron accumulation or depletion at the Pd/PZT interface. Spectra taken with $c+$ and $c-$ polarized light and resulting XMCD spectrum for the accumulation scenario are shown in (b) and (c), respectively. (d) and (e) show XAS and XMCD difference for electron depletion at the interface.

Pd (4 nm)/ PZT nanostructures at the X-Treme beamline. All investigated structures showed in-situ FE switching; an example of an I-V curve was given earlier in chapter 2.1, see Fig. 2.2.

Fig. 4.2 compares the optical microscope image (a) with an X-ray absorption 2D scan of the same sample region taken at 531 eV corresponding to the Pd M_3 edge energy via TEY (b). The picture highlights the procedure how to locate the nanostructures. The top electrode is connected to the analog-to-digital-converter monitoring the TEY. The thick Au pads have the highest conductivity and show the highest count rate. The count rate stemming from the Pd pads is a bit lower (green). The bare PZT substrate area beside the Pd pads also causes a high count rate in proximity to the conducting Au structure and is not distinguishable from the Pd pad. This is due to oxygen K edge which is found in the same energy range as the Pd M edge and contributes to the TEY since the PZT is oxygen-rich. Therefore, a more precise procedure to find the connected Pd pad of interest was to monitor the photocurrent across the PZT at the back electrode by scanning the sample surface with the focussed x-ray beam. An example of a photocurrent 2D scan for a switchable Pd pad is shown in Fig. 4.2(c). Five positions on and around the Pd pad are indicated in Fig. 4.2(c), XAS spectra taken at those positions are displayed in Fig. 4.2(d) (vertically offset for clarity). All marked positions give rise to a XAS spectrum within the energy interval of interest. On the Pd pad two elements contribute to the XAS spectrum, that is palladium from the Pd thin film and oxygen contained in the PZT ferroelectric substrate underneath. On the bare substrate the XAS spectrum arises solely due to the oxygen content in the PZT. Spectra taken on the Pd pad show a broader peak above 536 eV at the M_3 edge while the PZT shows a double peak in that energy range, Pd gives also rise to a more pronounced M_2 edge from 550 eV onwards. The similarity of the spectral shape and the small contact size area imply that a good temperature stabilization is crucial to exclude thermal drift away from the Pd pad and obtain good statistics with scans taken at the same sample spot. Fig. 4.3 (a) reports XAS spectra ($c+ + c-$) at the Pd $M_{3,2}$ edges taken in normal incidence under a magnetic field of 6.5 T for the cases of accumulation and depletion at the Pd/PZT interface at 2 K. The line shape does not change upon switching. XAS spectra taken with $c+$ and $c-$ polarized light in normal incidence at 6.5 T and 2 K are shown in Fig. 4.3 (b) for the accumulation state and in (d) for the depletion state, the respective difference spectra normalized on the M_3 XAS edge jump are shown in (c) and (e). No XMCD line shape indicating a magnetic contribution is obtained within the noise ratio of 0.2% for both FE polarization states.

4.1.3 XAS and XMCD at the Pd L edge

Since the overlap with the O K edge prevents a clear measure of the Pd $M_{3,2}$ edges, measurements were extended to the Pd $L_{3,2}$ edges where no other spurious contributions are present. They were conducted at the PHOENIX beamline (Paul Scherrer Institut, Switzerland) where XMCD had not been established before. For higher harmonics the polarization degree decreases (here, for Pd the 5th harmonic is used). Hence, a Ta(1.5)/Pd(1.6)/$[$Co(0.3)/Pd(0.9)$]_8$/Pd(0.9) multilayer (numbers in units of nm) was checked beforehand as a test sample where magnetism at the Pd L edge is expected, see Fig 4.4 for the XAS and XMCD spectrum taken at room temperature. Measurements (here and in the following) were taken with a geometry close to normal incidence with the x-rays impinging at an angle 3° away from the surface normal under a magnetic field provided by permanent magnet, ~ -0.45 T along the sample surface normal. The energy selective fluorescence detector allowed to select the counts corresponding to the energy interval of the Pd L_3 and L_2 edge, respectively. Hence, it is possible to remove a large part of the contributions to the TFY signal stemming from other elements. The XMCD spectrum in Fig 4.4 is normalized to the respective L_3 or L_2 edge jump.

Figure 4.5 shows XAS ($c+$ + $c-$) L_3 edge measurements for the Pd(4nm)/ PZT(200nm) structure taken at 65 K under a magnetic field of a permanent magnet ~ -0.45 T, for opposite FE poling orientations. The XAS shape across the L_3 edge in Fig 4.5 does not change upon switching the FE. To exclude a possible depolarization of the PZT after FE switching due to x-ray illumination, measurements were done both at remanence and with ± 2 V applied, but no switching dependent change in XAS line shape was observed.

Spectra taken with $c+$ and $c-$ polarized light under the same temperature and geometry conditions for the cases of electron accumulation (left side) and electron depletion (right side) at the Pd/PZT interface are depicted in Fig. 4.6. No clear XMCD difference is visible within the noise level of about 1%. On the right side, the XMCD spectra for the depletion setting (in red) and for the case of accumulation (in blue) are superposed.

4.2 Discussion/Conclusion

At X-Treme, no XMCD difference signal was found within the noise ratio of 0.2%, when normalized on the M_3 XAS edge jump. Since also oxygen from the underlying PZT contributes to the edge jump, the noise ratio in percent referring solely to Pd will be higher. While the overlap with the oxygen edge is absent for the experiments

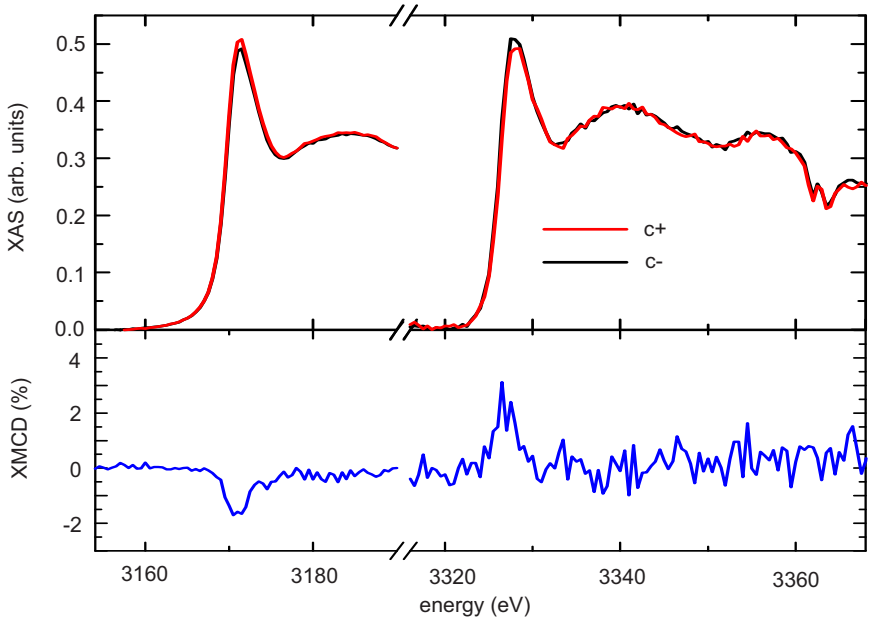

Figure 4.4: Pd L edge XMCD for a Ta(1.5)/Pd(1.6)/[Co(0.3)/Pd(0.9)]$_8$/Pd(0.9) multilayer (numbers in nm) taken at the PHOENIX beamline 3˚ off normal incidence under a magnetic field of 0.45 T at room temperature to confirm that XMCD acquisition is feasible at the PHOENIX beamline as far as the x-ray polarization is concerned.

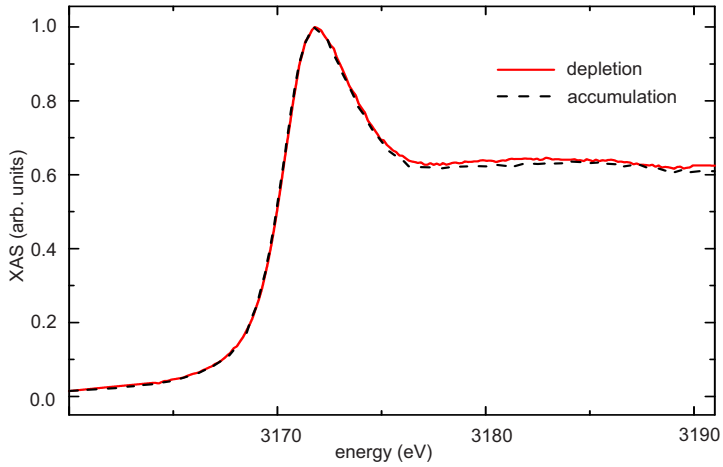

Figure 4.5: Pd L_3 edge XAS ($c+ + c-$) spectra for oppositely poled PZT substrate taken in a geometry 3˚off normal incidence under a magnetic field of 0.45 T at 65 K.

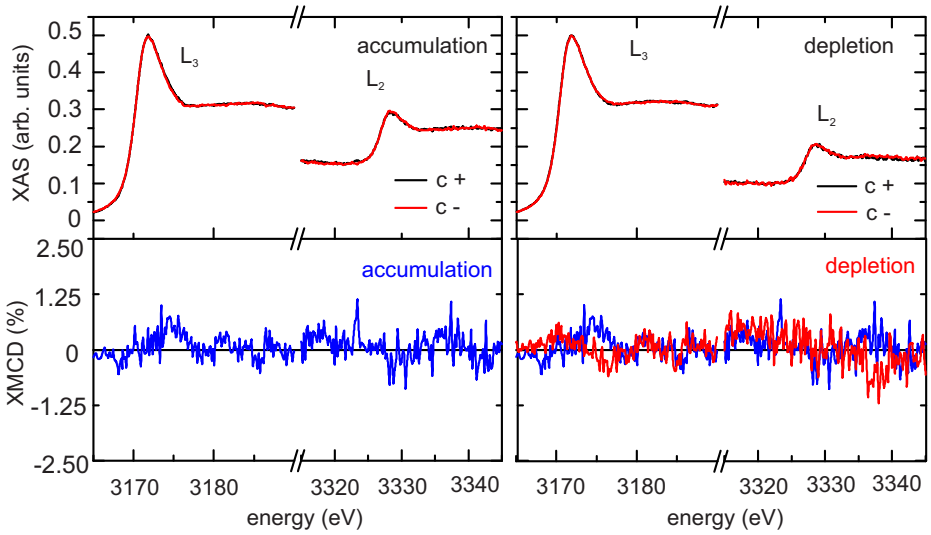

Figure 4.6: Pd $L_{3,2}$ edge XAS spectra taken with $c+$ and $c-$ polarized light and resulting XMCD spectrum for charge accumulation at the Pd/PZT interface (left) and for a charge depleted interface (right).

at PHOENIX, lower temperatures and higher magnetic field would be desirable to exclude that there is magnetism present in the Pd/PZT system.

Although for all measured nanostructures the displacement current upon switching was monitored in-situ both at X-Treme and at PHOENIX and the Pd film surface seemed to be continuous as shown by the AFM data, a dead layer or spurious contamination at the PZT surface cannot be excluded. To remove contaminations from the surface the PZT had been soft sputtered with Ar and outgassed at elevated temperatures prior to Pd deposition, as mentioned in section 4.1.1. The roughness of the PZT could also influence competing energy terms during growth and affect the single crystalline Pd growth on top of PZT [125, 126].

Additionally, while the Stoner criterion defines the onset of magnetic order, the latter could also include non-collinear spin configurations as the ground state, such as antiferromagnetism which would display no net magnetization. In principle such spin configurations can be investigated with XLD.

The absence of magnetism at the interface could be caused by hybridization across the Pd/PZT interface resulting in a larger bandwidth. Upon comparison with bulk Pd, interfacial Pd has a reduced coordination number and a decrease in the number of neighbours results in a narrower density of states [125]. Also, as the PZT lattice constant is slightly larger, the lattice mismatch should decrease the hopping matrix element and lead to a reduced hybridization. While these arguments would

help to fulfill the Stoner criterion, hybridization between top layer and substrate can have the contrary effect of reducing the electron density of states at the Fermi level thereby preventing the onset of magnetism.

Further research will be required to demonstrate electric field control of magnetism in Pd. In this regard we anticipate that hybridization at the interface and strain resulting from lattice mismatch are the key parameters to modulate the density of states in Pd. One could try other ferroelectrics such as $BaTiO_3$, $PbTiO_3$, $BiFeO_3$ or PMN-PT with different in-plane lattice mismatch and different hybridization formation between substrate and top layer. Regarding the modulation of the electron DOS at the Fermi level, PZT prepared by molecular beam epitaxy can reach much higher polarizations of $P = 85\ \mu C/cm^2$ [127], $BaTiO_3$ reaches up to $P = 70\ \mu C/cm^2$ [128], $PbTiO_3$ reaches $P = 75\ \mu C/cm^2$ [37], for $BiFeO_3$ values of $P = 150\ \mu C/cm^2$ [129] have been reported[3]. Another route to proceed would be to investigate a field effect structure, for example Pd on paraelectric $SrTiO_3$, where the induced charge at the interface can be varied continuously.

[3]All values at room temperature, allowing for modulations of $2 \times P$.

Chapter 5

Controlling magnetism via strain - LSMO/PMN-PT

Chapter 2.3.3 reviewed strain dependent studies on the ferromagnetic manganites. The magnetic properties of the manganites have been found to be very susceptible to pressure [87, 88, 93, 94, 95, 96] or strain [89, 90, 91, 92, 97, 98]. For example, LSMO exhibits different Curie temperatures and anisotropy behaviour when grown epitaxially under lattice mismatch on various substrates [89]. Thiele et al. [98] reported electric field induced changes in T_C as well as in magnetization for LSMO/PMN-PT (001) due to the piezoelectric properties of the substrate; however, induced changes did not remain once the bias field was switched off. This chapter investigates the magnetoelectric coupling in a bilayer consisting of LSMO (x =0.3) on top of ferroelectric PMN-PT (x =0.32) (011) that can exhibit two distinct remanent strain states in the (011) cut. The material characteristics of LSMO and PMN-PT have shortly been reviewed in chapters 2.3 and 2.1.2, respectively. In this chapter, we find that reversible electrical switching of the PMN-PT polarization results in a 10 K shift of the Curie temperature T_C of LSMO. Section 5.1.2 presents results on the strain induced change in the Curie temperature employing XMCD. XRD reciprocal space maps in section 5.1.3 give a complete picture of the PMN-PT lattice parameter changes, which induce the magnetization change in LSMO. Changes in crystal field during the switching process are highlighted in XNLD measurements and multiplet calculations in section 5.1.4. Density functional theory (DFT) calculations give details on the electron redistribution between e_g orbitals. The following chapter is partly adapted from our recent publication [52].

5.1 Results

5.1.1 Sample preparation and experimental details

An 8 nm thick film of LSMO has been grown on PMN-PT (x =0.32) (011) by pulsed laser deposition. The film was synthesized from a stoichiometric target using a laser fluence of 1.3 J/cm^2 at a repetition rate of 0.5 Hz while the PMN-PT substrate was kept at a constant temperature of 660 °C in a 300 mTorr O_2 ambient environment. With a pseudocubic bulk lattice constant of 3.878 Å LSMO grows in tension on PMN-PT (detailed characterization given in section 5.1.3). The (011) PMN-PT single crystal ferroelectrics used in this work were manufactured by Atom Optics Co., LTD. (Shanghai, China) using the modified Bridgman growth method with a nominal percentage of 32 % TiO_2 powder. The FE polarization of the substrate was switched in-situ by applying the appropriate electric field values. The two distinct strain states for OOP and IP poling of the ferroelectric that can be set by an applied voltage have been described in section 2.1.2 and are sketched in Fig. 2.3.

The XAS measurements were done in TEY mode at the X-Treme beamline, Paul Scherrer Institute, Switzerland. For details, see section 3.4.1. Spectra were recorded with the x-rays set at 60° from the sample surface normal. If not otherwise stated, the procedure of XAS data analysis was the following: From all XAS spectra a constant background was subtracted at the pre-edge. XMCD difference spectra ($c+ - c-$) and XNLD difference spectra ($LH - LV$) were normalized to the L_3 XAS peak height. If not otherwise stated, measurements were taken at 250 K, which is below the ferromagnetic Curie temperature of LSMO. Temperature dependent XAS measurements for both PMN-PT poling states were done at remanence on substrates originally poled at 250 K.

5.1.2 Strain dependent XAS and XMCD measurements

Figure 5.1 shows Mn $L_{3,2}$ XMCD measurements with the magnetization projected along $[01\bar{1}]$ at 0 T[1] after saturating at 3 T in grazing incidence geometry as a function of applied voltage. The magnitude of the XMCD is proportional to the magnetization component along the x-ray beam. Starting with a negatively OOP poled PMN-PT substrate in zero applied electric field, the LSMO magnetization starts to decrease while approaching the coercive field value. At 0.22 MV/m the polarization of the PMN-PT rotates parallel to the plane, and LSMO exhibits a minimum of magnetiza-

[1] At X-Treme, the remanent magnetic field ranges from 40 to 100 Oe, depending on the maximum magnetic field applied before.

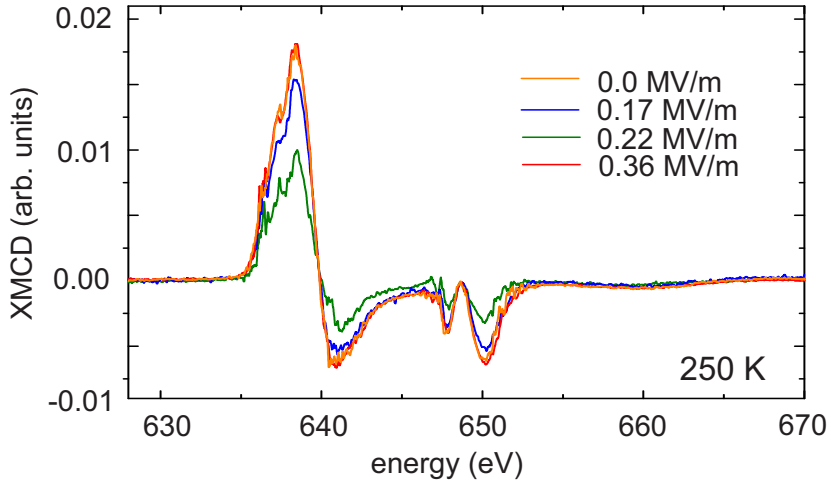

Figure 5.1: Mn $L_{3,2}$ XMCD spectra measured in remanence at 250 K along $[01\bar{1}]$ as a function of applied electric field.

tion along $[01\bar{1}]$. For higher electric field values the PMN-PT polarization is switched to OOP, and the XMCD signal recovers.

While Fig. 5.1 shows the decrease of the LSMO magnetization in applied electric field, Fig. 5.2 compares Mn $L_{3,2}$ XMCD measurements for the two distinct OOP (black curves) and IP (red curves) poled states of PMN-PT (011) taken at remanence. Insets depict the geometry that allows for the measurement of the respective magnetization projection along [100], $[01\bar{1}]$ and [011]. Figure 5.2 (a) reports the XAS spectrum (upper curve) and XMCD difference spectrum (lower curve) measured along the [100] direction. Comparing measurements for OOP and IP poled substrate, the XAS does not change, but the XMCD is reduced in the IP poled state. This change in magnetization upon switching is most pronounced for the spectra measured along the $[01\bar{1}]$ direction, see Fig. 5.2 (b). The difference at the L_3 edge measured for the OOP poled substrate reduces to half its value once the substrate is electrically switched to the IP state. Normalized XAS and XMCD measurements along the [011] direction are shown in Fig. 5.2 (c). Comparing the three orthogonal directions, the L_3 lower energy side of the XAS looks different between the [100] and $[01\bar{1}]$ directions but looks the same for [011] and $[01\bar{1}]$, reflecting that the XAS is sensitive to the crystallographic direction/site symmetry of the unoccupied Mn 3d states. The effective Mn spin magnetic moment $m_{\mathrm{s,eff}}$ and orbital magnetic moment m_{orb} along the different crystallographic directions is extracted from the spectra in Fig. 5.2 using sum rules [107, 108]. An example of the analysis is given in Fig. 3.5 (a) for the XAS spectrum (after subtraction of a background) and

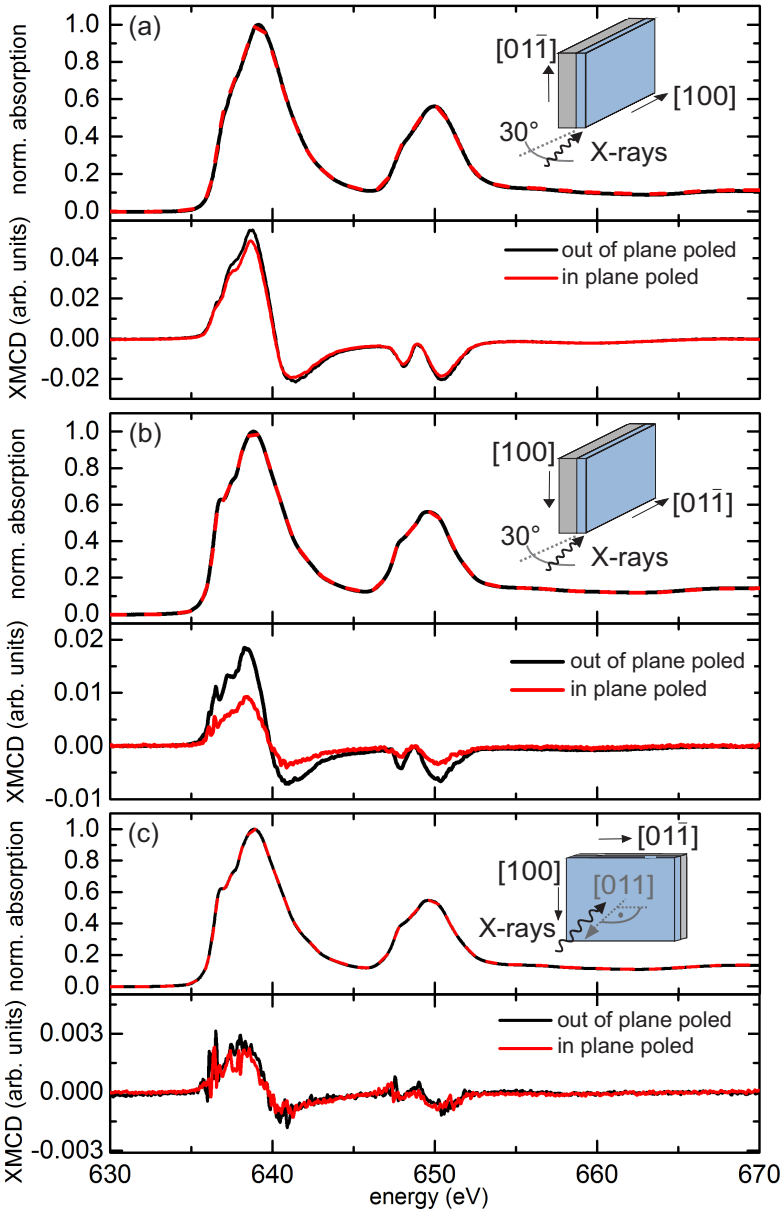

Figure 5.2: Mn $L_{3,2}$ polarization averaged XAS (top) and XMCD difference spectrum (bottom) measured in remanence at 250 K along different crystallographic directions: (a) projection along [100], (b) projection along [01$\bar{1}$], (c) projection along [011]. Black (red) curves correspond to OOP (IP) poled PMN-PT substrate. Figure adapted from [52].

Table 5.1: Projected effective Mn spin moment $m_{\mathrm{s,eff}}$ and orbital moment m_{orb} along different crystallographic directions for both OOP and IP poled FE substrate at 250 K extracted from Fig. 5.2.

crystallographic direction	OOP poled polarization		IP poled polarization	
	$m_{\mathrm{s,eff}}$ (μ_B/Mn)	m_{orb} (μ_B/Mn)	$m_{\mathrm{s,eff}}$ (μ_B/Mn)	m_{orb} (μ_B/Mn)
along [100]	0.84 ± 0.08	-0.024 ± 0.005	0.73 ±0.07	-0.024 ± 0.005
along [01$\bar{1}$]	0.24 ± 0.02	-0.0007 ±0.0001	0.15 ± 0.01	-0.0026 ±0.0005
along [011]	0.026 ± 0.003	-0.0013 ± 0.0003	0.026 ± 0.003	-0.0013 ± 0.0003
along [01$\bar{1}$] at 4 T	1.72 ± 0.17	-0.019 ± 0.004	1.75 ± 0.17	-0.039 ± 0.008

Fig. 3.5 (b) for the XMCD difference spectrum, respectively.

Here, a number of 4.3 electrons per Mn ion was assumed [130, 131]. Multiplet calculations using Cowan's Code [132] yield a spin correction factor of 1.52, to disentangle the overlap of the L_3 and L_2 parts in the spectrum, see also section 3.2.2. Table 5.1 lists $m_{\mathrm{s,eff}}$ and m_{orb} for both strain states. The orientation of $m_{\mathrm{s,eff}}$ and m_{orb} is antiparallel, consistent with the third Hund's rule in the case of a less than half-filled d shell.

The total magnetic moment $m_{\mathrm{tot}} = m_{\mathrm{s,eff}} + m_{\mathrm{orb}}$ is dominated by the spin magnetic moment. The orbital moment is mostly quenched by the crystal field as expected. Table 5.1 confirms the OOP direction [011] being the hard axis and the magnetization is pointing parallel to the surface as expected for LSMO thin films. As for the in-plane directions, [100] is the easy axis and [01$\bar{1}$] the hard axis. Both in-plane directions yield a smaller projected m_{tot}, once the substrate is in the IP poled state. Although the IP switching may be accompanied by an anisotropy change, it is not the only effect at play: if the observed changes upon switching would be a mere rotation of the anisotropy, a decrease in m_{tot} along one in-plane axis would be accompanied by an increase along the perpendicular in-plane direction. Table 5.1 also gives values of the spin and orbital magnetic moments along the [01$\bar{1}$] direction taken at a magnetic field of 4 T. At saturation, the poling direction does not influence the total magnetic moment within the experimental error, yielding m_{tot}=1.70 ± 0.17 μ_B/Mn and m_{tot}=1.71± 0.18μ_B/Mn for OOP poling and IP poling at 250 K. The saturated Mn total moment m_{tot}=3.36±0.34 μ_B/Mn measured at 50 K is comparable to the typical low temperature value for bulk LSMO ∼3.6μ_B/Mn [92].

XMCD measurements as a function of temperature are used to determine T_C

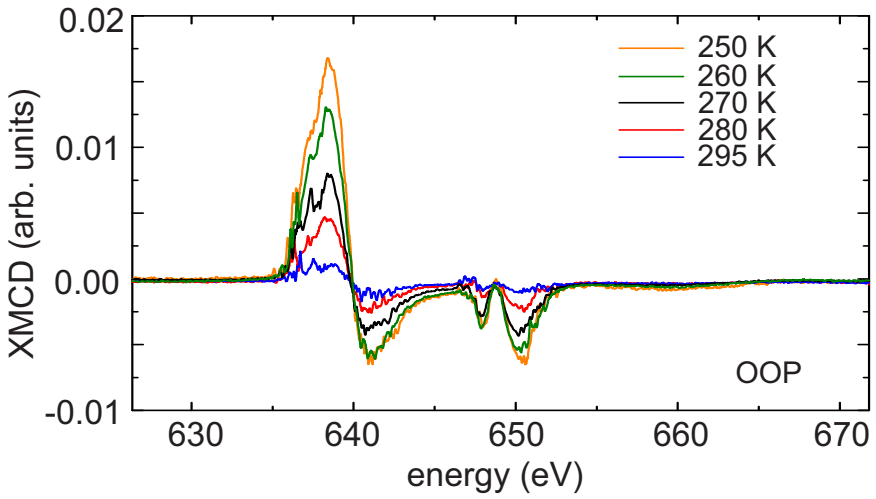

Figure 5.3: XMCD spectra along the $[01\bar{1}]$ axis at remanence as a function of temperature.

of the LSMO film[2]. Figure 5.3 shows the decrease in XMCD signal along the $[01\bar{1}]$ axis at remanence with increasing temperature for OOP poled PMN-PT. The temperature dependence of the extracted m_{tot} for both poled PMN-PT states is shown in Fig. 5.4. For the OOP poled substrate the magnetic moment vanishes at 300 K (black curve). Switching the FE polarization of the PMN-PT to the IP poled state, T_C shifts by -10 K (red curve). The electrical switching thus results in different Curie temperatures. XMCD probes a particular direction of the magnetization. Resistance measurements as a function of temperature for both poling states, also shown in Fig. 5.4, exclude a mere rotation of the moments away from the $[01\bar{1}]$ direction. The correlation between resistivity and T_C can be understood from the double exchange mechanism where a FM spin alignment of neighbouring Mn sites favours conductivity [84], hence resistivity measurements are widely used to determine the onset and evolution of ferromagnetism in manganite films [82, 133]. Here, the resistivity measurements yield approximate T_C values of 298 K (288 K) for OOP (IP) poled PMN-PT indicated by the maxima in the resistivity curves. The resistance measurements confirm the T_C shift of the XMCD measurements. The measured T_C values are somewhat reduced compared to the bulk value of about 370 K [134, 135] as expected for thin films [89, 136].

The heterostructure enables the reversible electrical switching of the Curie tem-

[2]Due to a small drift observable in subsequently measured XAS spectra at 200 K and 220 K the procedure was the following: From all XAS spectra a constant background was subtracted at the pre-edge. XAS spectra were normalized at the post-edge.

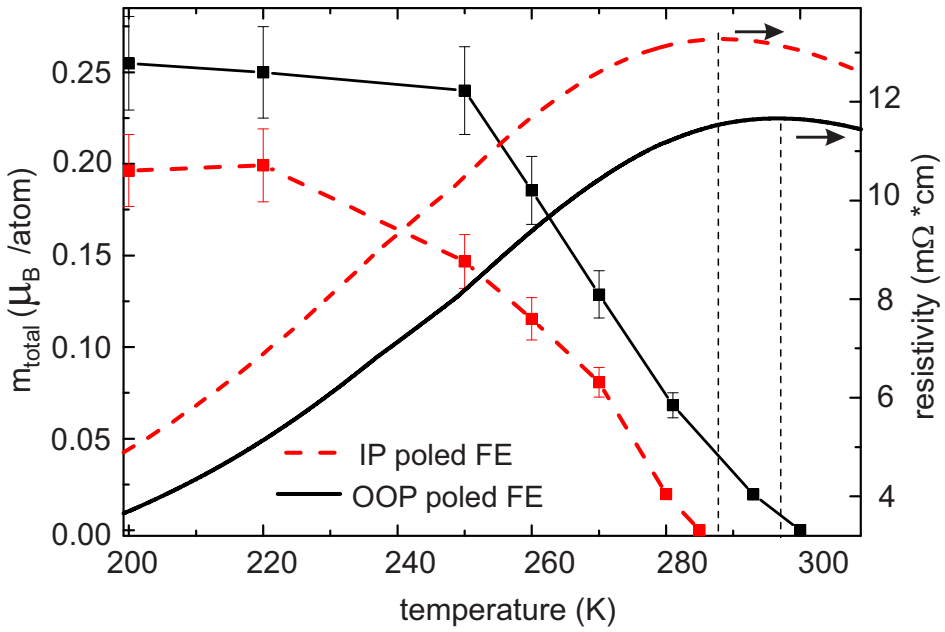

Figure 5.4: Magnetic moment along the $[01\bar{1}]$ axis at remanence and resistivity as a function of temperature. Red dashed lines correspond to IP poled FE, black lines correspond to OOP poled FE. Figure adapted from [52].

perature. The anisotropic in-plane strain triggering the T_C change is explored in detail in the following section.

5.1.3 X-ray diffraction - 2D reciprocal space maps

For PMN-PT (011), several voltage-dependent biaxial strain gauge measurements have been reported [20, 101]. However, they can only provide strain values along two independent in-plane directions. Furthermore, when using strain gauges, the piezoelectric substrate is glued to the sensor via a relatively thick layer of glue which can lead to an underestimation of the absolute strain value. XRD circumvents those problems by directly measuring the lattice parameters of the crystal in all three dimensions.

The crystal structure of both FE IP and OOP poled PMN-PT (011) was determined by performing XRD mappings around symmetric and asymmetric diffraction peaks. Measurements were done at remanence after electrical switching at 300 K, therefore the coercive field is slightly smaller than the one observed in the XMCD measurements taken at 250 K. Figure 5.5 shows reciprocal space maps for (011),

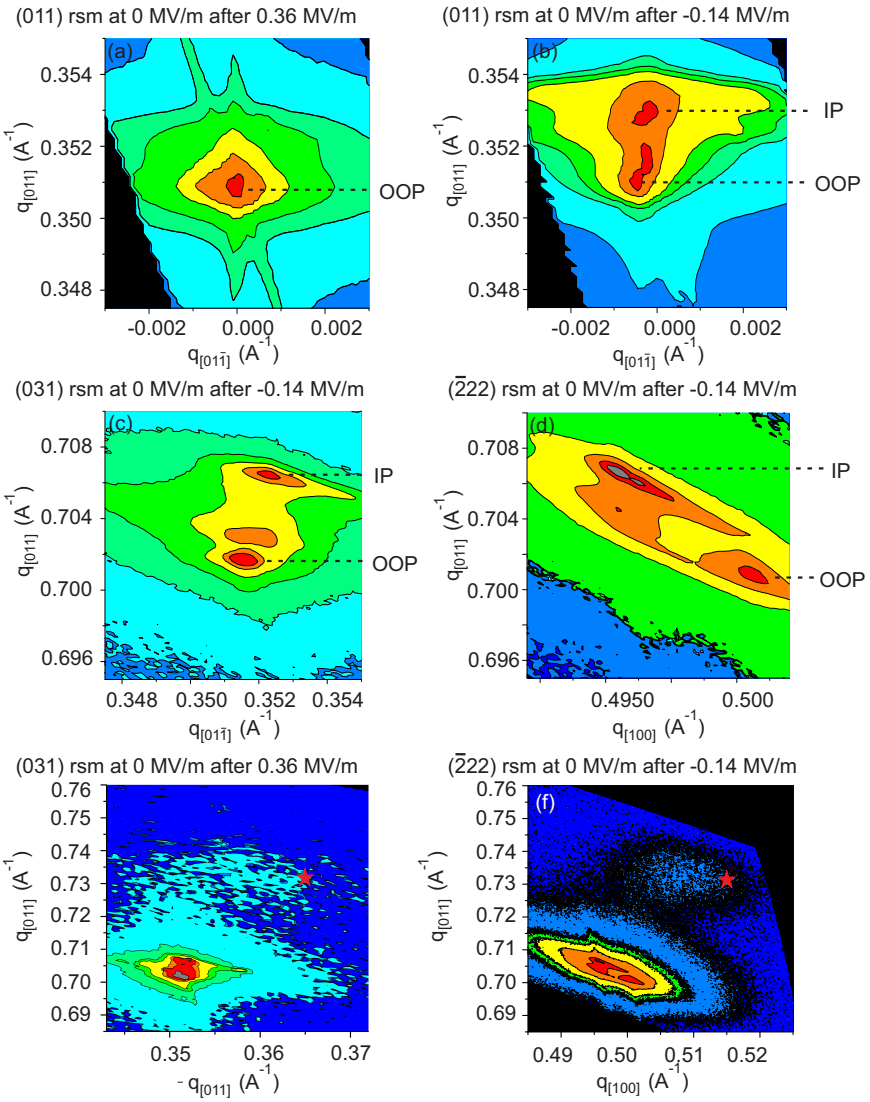

Figure 5.5: Reciprocal space maps for (011), (031) and ($\bar{2}22$) reflections on PMN-PT (011) for both poling states. (a) For OOP poled PMN-PT the (011) RSM shows a single reflection. (b) For the IP poled state the (011) RSM shows an additional reflection corresponding to IP poled domains. When switching the FE polarization from OOP to IP, the (031) RSM in (c) highlights an IP contraction along [01$\bar{1}$], the ($\bar{2}22$) RSM in (d) shows a respective tensile lattice parameter change along [100]. (e) and (f) show reflections of both substrate and the LSMO thin film, asterisks mark the expected peak positions for a fully relaxed LSMO film. Figure adapted from [52].

Table 5.2: q-values extracted from the RSMs for OOP and IP poled PMN-PT domains and resulting relative lattice parameter change along different crystallographic directions. Errors in q are smaller than $\pm 1.44 \times 10^{-5}$ Å^{-1} and $\pm 1.25 \times 10^{-5}$ Å^{-1} for IP and OOP domains, respectively.

		OOP poled FE	IP poled FE	lattice change switching from OOP to IP
RSM (011)	$q_{[011]}$ in (Å^{-1})	0.3508	0.3532	-0.68%
RSM (031)	$q_{[022]}$ in (Å^{-1})	0.7015	0.7064	-0.71%
	$q_{[01\bar{1}]}$ in (Å^{-1})	0.3515	0.3523	-0.23%
RSM ($\bar{2}22$)	$q_{[022]}$ in (Å^{-1})	0.7016	0.7066	-0.72%
	$q_{[100]}$ in (Å^{-1})	0.5007	0.4962	+0.90%

(031) and ($\bar{2}22$) reflections on LSMO/PMN-PT (011). Starting with a positively OOP poled PMN-PT substrate, Fig. 5.5 (a) shows a single (011) reflection with $q_{[011]}$=0.3508 Å^{-1} corresponding to a lattice constant c $\sim \sqrt{2}/q_{[011]} = 4.031$ Å. Reversing the applied voltage, the FE polarization rotates in-plane at the coercive electric field of -0.14 MV/m. In the (011) RSM in Fig. 5.5 (b) a second reflection appears at $q_{[011]}$=0.3532 Å^{-1} due to the IP poled domains. Not all domains have switched or some have already switched to the opposite OOP FE poling direction, as can be seen in Fig. 5.5 (b), since both reflections coexist with an intensity ratio of $\sim$60/40 for IP/OOP domains. As a larger $q_{[011]}$ value implies a smaller interplanar spacing, the electrical switching of the FE polarization from OOP to IP induces a contraction of -0.68%. The RSM of the (031) reflection in Fig. 5.5 (c) confirms the values of $q_{[011]}$ for OOP and IP poled domains in Fig. 5.5 (b), since the measured $q_{[022]}$ values are just multiples of the $q_{[011]}$ values. In addition, the (031) RSM allows one to deduce the voltage induced lattice parameter change along [01$\bar{1}$]: switching the FE polarization of the substrate to IP leads to a contraction of -0.23 % along [01$\bar{1}$]. Finally, the ($\bar{2}22$) RSM in Fig. 5.5 (d) shows that IP poling results in a larger interplanar spacing of +0.90 % along the [100] direction. All q-values are listed in table 5.2.

The RSMs give the complete picture of the resulting lattice changes upon switching in the PMN-PT. Besides the induced lattice parameter change upon switching, it is important to know the epitaxial strained state of the LSMO thin film compared to bulk. Figures 5.5 (e) and (f) show a larger section of the (031) and ($\bar{2}22$) RSMs that allow us to give estimates for the LSMO lattice parameters. The reflection

corresponding to the LSMO thin film is seen in Fig. 5.5 (e) and (f) in the upper right corner with respect to the PMN-PT reflection. The small number of diffracting planes leads to a spreading of the reflection peak in reciprocal space. However, it can be seen that only a partial lattice relaxation occurs. The expected peak positions for a fully relaxed film are indicated by an asterisk. The (031) RSM in Fig. 5.5 (e) shows the OOP poled state. Having its maximum at $q_{[01\bar{1}]}$=0.3558 Å^{-1}, LSMO is under tensile strain of approximately +2.49 ± 0.14% along the $[01\bar{1}]$ direction with respect to its bulk value. Regarding the OOP direction [011], LSMO is compressed by about $-0.40 \pm 0.05\%$. Figure 5.5 (f) shows a $(\bar{2}22)$ RSM for the IP poled state. Within the broad reflection peak, the two maxima corresponding to IP and OOP poled domains cannot be resolved separately. The broad maximum at $q_{[100]}$=0.5080 Å^{-1} corresponds to an average of $+1.52 \pm 0.02\%$ tensile strain along the [100] direction. Therefore the strain of the LSMO film differs along orthogonal in-plane directions.

5.1.4 Strain dependent x-ray natural linear dichroism

XNLD at the Mn $L_{3,2}$ edges is employed to probe the anisotropy of the Mn 3d orbital occupation in LSMO/PMN-PT (011) upon electric switching. Measured above T_C and with no magnetic field applied, the observed difference has no magnetic linear dichroism contribution and thus represents a change in crystal field. The results are reported in Fig. 5.6.

In our measurement geometry, at normal incidence, vertically polarized light probes the [100] direction and horizontally polarized light probes the $[01\bar{1}]$ (see the inset in Fig. 5.6 (a)). The x-ray polarization averaged XAS both for OOP (black) and IP (red) poled PMN-PT are shown in Fig. 5.6 (a). Comparing the two distinct strain states the XAS does not change. Fig. 5.6 (b) depicts the XNLD for the OOP poled (black) and the IP poled (red) state. Upon electrical switching the shape of the XNLD spectra is similar, but the relative XNLD signal intensity almost doubles for the IP poled state indicating a much larger charge asymmetry for the IP poled state. Atomic multiplet calculations help to clarify in which way changes in crystal field affect XAS spectra.

Multiplet calculations

The influence of biaxial in-plane strain on XAS spectra is investigated using multiX [114] multiplet calculations (see section 5.1.4). Starting with the crystallography data file [115] for LSMO with x =0.3 doping of rhombohedral symmetry the program ATOMS [137] is used to create a list of atomic coordinates x, y and z for Mn, O and

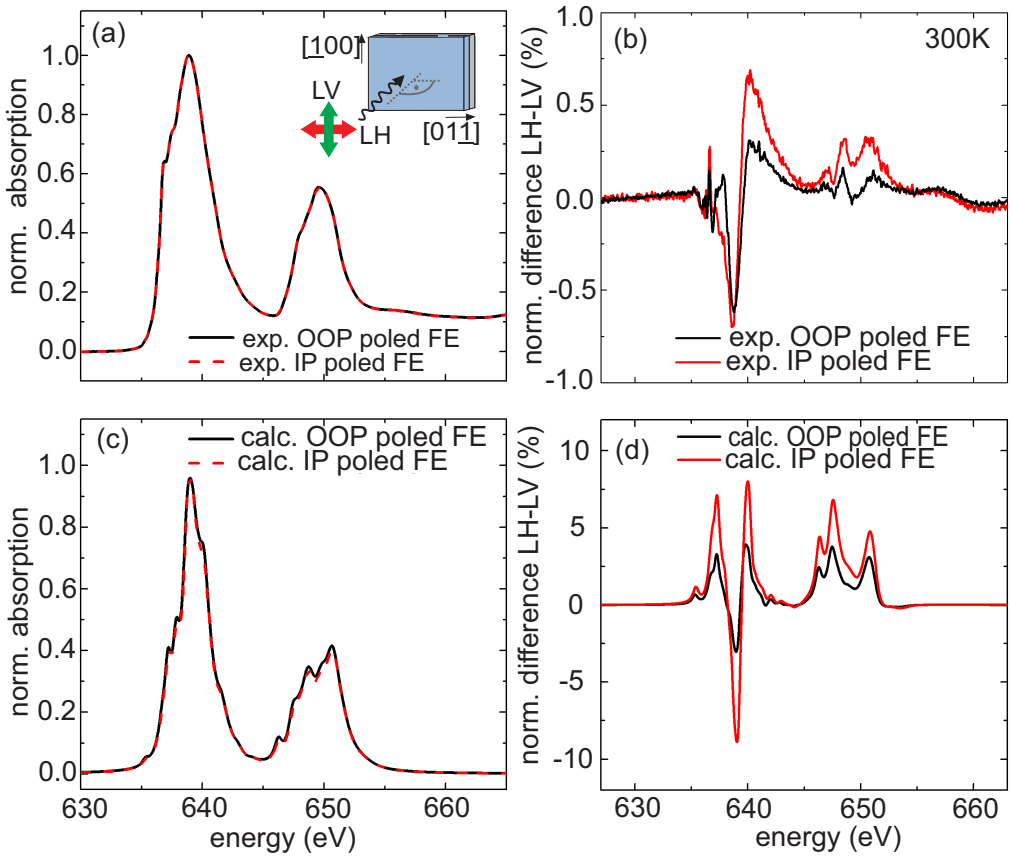

Figure 5.6: Mn $L_{3,2}$ normalized polarization averaged XAS from experiment (a) and multiplet calculations (c) for out of plane poled (black) and in-plane poled (red) PMN-PT at 300 K. The inset depicts the measurement geometry. The XNLD difference (LH-LV) with light polarized along [100] (LV) and [01$\bar{1}$] (LH) from experiment and calculations for both poling states of PMN-PT is shown in (b) and (d) respectively. Figure adapted from [52].

La ($LaMnO_3$) or Mn, O and Sr ($SrMnO_3$), respectively. A column containing the nominal ionic charge of each element was added. This list simulates a crystal field of about 17 Å radius around the Mn central atom. The crystal field data set is transformed to the coordinate system with [100], [01$\bar{1}$] and [011] axes, so strain can be applied to the ion positions simulating the situation of lattice mismatch of the LSMO film grown epitaxially on PMN-PT (011). The multiX code is run with the crystal field further transformed to pseudocubic symmetry where the axes of the oxygen octahedra around the Mn align with [100], [010] and [001], respectively. In analogy to the normal incidence geometry of the experiment, [01$\bar{1}$] and [100] were

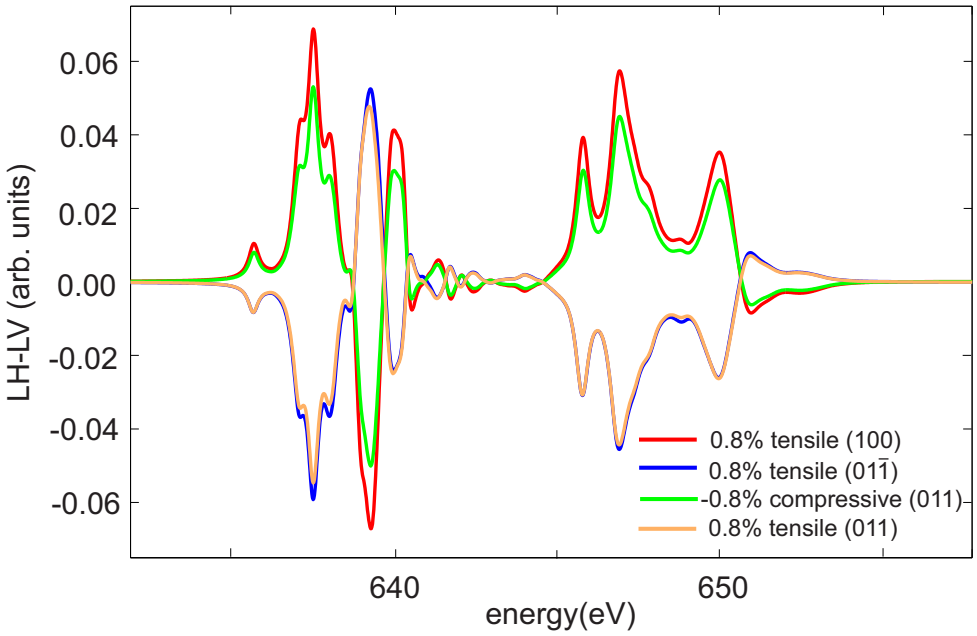

Figure 5.7: Calculated XNLD difference spectra at the Mn L edge for $LaMnO_3$ crystal field files under different strain conditions. Tensile strain was applied along a single axis, either [100] (red), [01$\bar{1}$] (blue) or [011] (orange), respectively. Compressive strain, shown for the [011] direction (green), yields a reversed line shape with respect to tensile strain.

chosen as linear polarization directions of the incoming light. The lines hapes in Fig. 5.7 are examples of XNLD multiX spectra corresponding to an applied strain along a single denoted axis that is [100], [01$\bar{1}$] or [011]. The situation where the unit cell is distorted due to in-plane lattice mismatch refers to a composition of strains along all three axes.

To compare the experimental XNLD in Fig. 5.6 (a) and (b) with multiX multiplet calculations, the OOP poled state is created by applying the constraints of epitaxial growth deduced from the RSMs Fig. 5.5 (e) and (f) in section 5.1.3 to all surrounding atoms: -0.4% compressive strain along the [011] direction, $+2.5\%$ tensile strain along the [01$\bar{1}$] direction and $+1.05\%$ tensile strain along the [100] direction. Here, for the [100] direction the maximum (1.5% tensile strain) extracted from the LSMO reflection in Fig. 5.5 (f) was assumed to present an average of domains in the OOP poled (1.05% tensile strained) and the IP poled (1.95% tensile strained) configuration, keeping in mind the PMN-PT lattice parameter change of

+0.9% upon switching. The resulting calculated XNLD difference spectrum obtained for the OOP poled case is shown in black in Fig. 5.6 (d).

To simulate LSMO in the IP poled state the procedure is the same, but the coordinate files representing the OOP poled case are further strained applying the strain values upon switching deduced from the PMN-PT RSMs (Fig. 5.5 (a) - (d)), i.e. an additional tensile strain of +0.9% along [100], as well as compressive strains of −0.23% along $[01\bar{1}]$ and −0.7% along [011]. The calculated XNLD difference spectrum obtained for the IP poled case would represent a single IP poled domain. The RSMs in section 5.1.3 gave an IP/OOP domain distribution ∼60/40. To compare with the measured XNLD, the simulations obtained for IP poled state and OOP poled state were averaged accordingly. This averaged XNLD spectrum representing the IP poled state is shown in Fig. 5.6 (d) in red. The multiplet calculations reproduce the experimental trends well as can be seen when comparing Fig. 5.6 (b) and (d).

For comparison, the LSMO XNLD calculations representing the IP poled case have been repeated, this time using strain values obtained by voltage-dependent biaxial strain gauge measurements for PMN-PT (011) [20]: Upon poling the FE from OOP to IP, Wu et al. measured 0.15% tensile strain response along $[01\bar{1}]$, 0.025% tensile strain along [100] as well as −0.15% compressive strain along [011] (The strain along [011] was derived assuming volume conservation). Figure 5.8 shows the resulting multiX calculation for this alternative scenario of IP poling. There is only a marginal difference observable between the OOP (in blue, simulating epitaxial growth as shown above) and IP (in red) poled case. In strain gauge measurements, an intermediate layer of glue between PMN-PT and strain gauge could lead to an underestimation of the absolute strain value. Hence, calculations are also shown for strain values from [20] enhanced by a factor of five (corresponding to the green XNLD spectrum), so the magnitude would be comparable to the lattice parameter changes observed in section 5.1.3. The comparison of the OOP poled state with the and IP poled scenario suggested by strain gauge measurements [20] does not meet the experimental observations in Fig. 5.6 (b), showing hardly visible changes for the different strain states. This is also evident from Fig. 5.7, since the XNLD change due to tensile strain along $[01\bar{1}]$ counteracts the XNLD change stemming from compressive strain along [011], and the strain gauge measurements report the same magnitude of strain response with opposite sign for the respective directions.

In contrast, the strain values extracted from RSMs in section 5.1.3 yield the correct line shape for the calculated XNLD spectrum and reproduce the XNLD increase upon IP poling, emphasizing that the changes in bond length play the key role to reproduce the spectroscopic features. Note that the first peak at 637 eV in the calculated difference spectrum is absent in the measured XNLD. This feature is

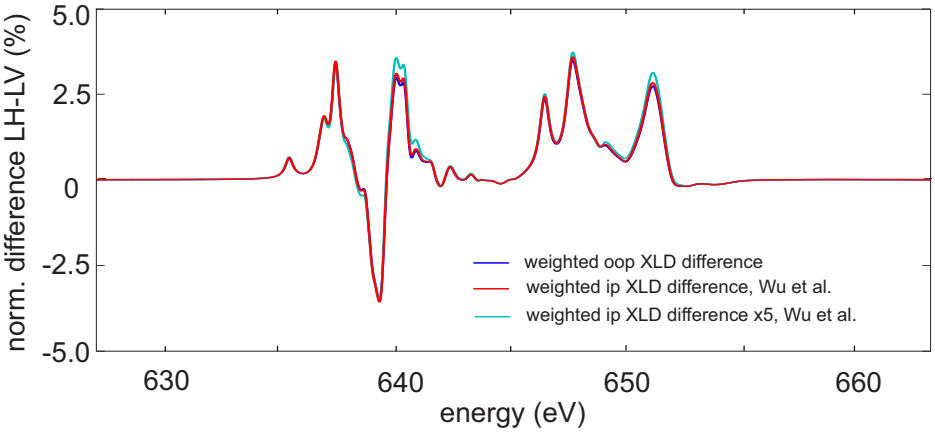

Figure 5.8: Calculated XNLD difference spectra (LH-LV) with light polarized along [100] (LV) and [01$\bar{1}$] (LH) at the Mn L edge for both poling states of PMN-PT by using the strain conditions upon IP poling from ref. [20].

also produced by other multiplet approaches, where the crystal field is introduced in a parameterized form depending on the point-group in consideration [99, 100]. Switching from an OOP state to an IP poled state, the intensity of the difference spectrum doubles due to the additional strain, but the lineshape of the XNLD does not change in agreement with experiment.

DMol^3 calculations

The $LaMnO_3$ crystal lattice strained to represent either the geometry of an OOP or an IP poled state is used as an input for DFT band-structure (DMol^3) [138] calculations provided through a collaboration with Bernhard Delley (Paul Scherrer Institut, Switzerland) in order to investigate the orbital occupation. Table 5.3 lists the occupation of the valence orbitals for both the OOP and IP poled strained constructed crystal field files. Regarding the majority spin, the Mn $d_{xy,yz,xz}$ orbitals corresponding to the t_{2g} representation are about fully occupied. All minority spin Mn d orbitals are largely unoccupied, except that the bonding bands for the e_g orbitals sum up to about 1/3. $d_{x^2-y^2,z^2-r^2}$ orbitals corresponding to the e_g representation are about half occupied. The strain leads to a redistribution of the 3d ground state population representing the e_g orbitals. The occupation ratio $d_{x^2-y^2}$ / $d_{z^2-r^2}$=1.031 for the OOP poled state increases to $d_{x^2-y^2}$ / $d_{z^2-r^2}$=1.077 for the IP poled state. As the experimental geometry probes the $d_{x^2-y^2}$ population along the in-plane [100] direction with LV polarized light, an increase of the difference spectrum (LH-LV) upon IP poling corresponds to a smaller density of empty states along the [100] direction

Table 5.3: DMol^3 calculations for the crystal field coordinate files in pseudocubic symmetry highlight the change in e_g orbital occupation that accompanies the strain changes.

Mn orbitals	OOP poled polarization		IP poled polarization	
	spin-up	spin-down	spin-up	spin-down
4 s	0.182	0.196	0.181	0.196
3 p_y	0.986	0.991	0.985	0.989
3 p_z	0.985	0.989	0.983	0.987
3 p_x	0.986	0.991	0.990	0.995
3 d_{xy}	0.988	0.176	0.988	0.174
3 d_{yz}	0.989	0.179	0.989	0.183
3 $d_{z^2-r^2}$	0.677	0.341	0.663	0.343
3 d_{xz}	0.989	0.178	0.988	0.176
3 $d_{x^2-y^2}$	0.698	0.336	0.714	0.334
occupation ratio $d_{x^2-y^2}/d_{z^2-r^2}$	1.031		1.077	

probed with vertical polarized light, i.e. an increase of the population parallel to the surface.

5.2 Discussion

In this study, we observe a T_C shift of 10 K due to electrical switching in both XMCD measurements along the $[01\bar{1}]$ direction and resistance measurements. Hence, the switching does not simply induce a mere rotation of the easy axis as previously reported [101] but a change in the exchange interaction. A similar magnitude in T_C change has been previously only observed under applied electric fields [98] or under hydrostatic compression [88] with a change of about 1.45 K/kbar. In contrast, our results show a reversible non-volatile T_C change, which can be understood along the lines of the model proposed by Millis and coworkers [86]. An anisotropic tensile strain changes Mn-O-Mn bond angles and increases the Mn-O distances, thus reducing the in-plane electron transfer. As a consequence the ferromagnetic double exchange mechanism is reduced leading to a general decrease in T_C. In the case of LSMO/PMN-PT (011) we observe a large tensile in-plane strain change upon switching $\sim$0.9% along the [100] direction, which contains a Mn-O-Mn bond chain. We note that our measured relative PMN-PT lattice changes deviate from reported strain gauge measurements [20]. Some of the strain gauge measurements were done

with thick Pt electrodes, that can lead to an underestimation of the strain variation [101, 20]. Here, we are directly distorting the LSMO lattice adjacent to the PMN-PT surface.

In the IP poled state, the LSMO exhibits a smaller projected m_{tot} at remanence for all IP directions. The FM phase in LSMO below T_C is characterized by the spontaneous alignment of Mn spins allowing for a delocalization of the e_g electrons, as the double-exchange interaction is of FM character. The smaller projected spin moment and higher resistivity observed for the IP poled state corresponds to a reduced e_g electron itinerancy and ultimately a lower T_C value. The fact that the saturation magnetization at 4 T remained the same for both strain states can be understood by recalling that a high magnetic field applied above T_C can reinforce FM alignment of spins leading to an induced magnetism [82].

The strain variations upon switching lead to a different orbital occupation as seen in the XNLD spectra. When measured above T_C, XNLD highlights changes in the crystal field upon switching. The multiX multiplet calculations for the IP and OOP poled state emphasize that the strain is the key to reproduce the spectroscopic features and is responsible for the crystal field change. A comparison of strain values for PMN-PT upon poling shows that the strain values extracted from the RSMs yield a good agreement between the experimental and calculated XNLD line shape and reproduce the XNLD increase upon switching, in contrast to strain values obtained by strain gauge measurements reported in literature.

DFT calculations using the strain states extracted from the RSMs yield a redistribution of the e_g population: for the OOP poled state, the occupation of orbitals oriented parallel to the surface plane is favoured over the occupation of orbitals pointing perpendicular to the surface. For the IP poled state, this occupation imbalance is further enhanced. The DFT calculations support the picture that the energy difference between the e_g levels is increased upon switching from OOP to IP, reinforcing the electron tendency to be localized, leading to a reduction of the Curie temperature.

5.3 Conclusion

In summary, this study demonstrated reversible electrical switching in LSMO/PMN-PT (011) resulting in a 10 K shift of the magnetic Curie temperature. Two distinct remanent strain states can be set in the substrate by poling the FE polarization out of plane or parallel to the surface. The PMN-PT (011) cut allowed the study of differently strained LSMO on a single substrate instead of LSMO on different substrates with distinct lattice mismatch. The change in crystal field upon switching

was probed by XNLD. MultiX multiplet calculations show that the change in Mn-O bond length due to the strain is the key to reproduce the XNLD spectral shape. DFT calculations support the picture that the structural modifications lead to a change in the population of the e_g orbitals favouring orbitals that lie in the surface plane, hence, localizing the electrons. Both effects, the lowering of the e_g itinerancy and the increase in the electron-lattice coupling, explain the reduction in T_C in agreement with the Millis model.

Chapter 6

Controlling magnetism via strain and charge - Co/PMN-PT

While the last chapter reported on strain mediated magnetoelectric coupling, the following chapter investigates a system that exhibits two interface coupling mechanisms, that is strain and charge. Only a few studies [139, 140, 141] and none beyond a phenomenological approach have been reported on the coexistence of different ME coupling mechanisms in a single system. As mentioned in the introduction, strain and charge influence material properties on different length scales. For example, lattice mismatch at interfaces in epitaxially grown heterostructures puts constraints that can extend to several tens of nanometers. Charge mediated ME coupling is an interface or surface sensitive effect where screening of surface charge takes place within the Thomas-Fermi screening length. In this chapter we study a heterostructure consisting of a Co wedge (0-7 nm) on top of the ferroelectric PMN-PT (011). We find that three distinct remanent and reversible magnetization states can be set at room temperature. Strain and charge contributions to the magnetic response upon electrical switching can be disentangled, since the wedge geometry allows for a thickness dependent study on a single substrate employing surface sensitive X-ray magnetic circular dichroism at the Co $L_{3,2}$ edges. Section 6.1.2 presents results on electrically controllable nonvolatile magnetoelastic anisotropy changes. Anisotropy changes originating from the polarity of the FE substrate are discussed in section 6.1.3. In combination with the RSM measurements on PMN-PT (011) (section 5.1.3) the findings serve as an input for ab-initio density functional theory calculations[1] that can explain both the strain induced magnetoelastic and charge induced magnetocrystalline anisotropy changes in Co/PMN-PT (011).

[1]Collaboration with Michael Fechner, ETH Zürich, Switzerland.

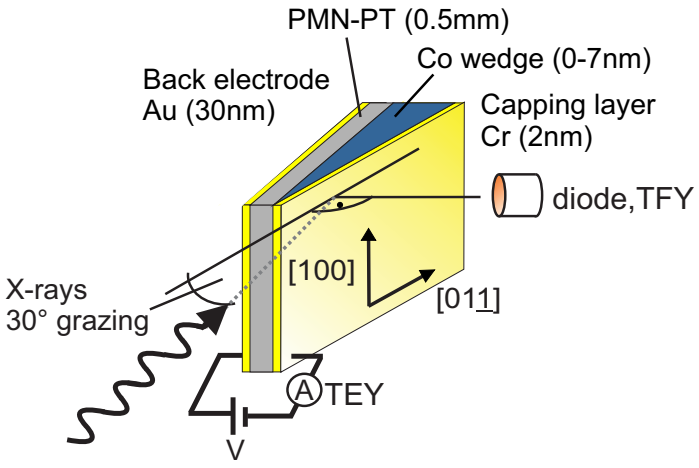

Figure 6.1: Schematics of the sample and measurement geometry.

6.1 Results

6.1.1 Sample preparation and experimental details

A schematic of the sample structure and the measurement geometry is shown in Fig. 6.1. Relaxor FE PMN-PT (011), with a composition of $x = 0.32$ was used as a substrate (produced via the modified Bridgman growth method by Atom Optics Co., LTD., Shanghai, China). For PMN-PT (011), the crystal structure and the lattice parameter changes in applied electric field have been described in section 2.1.2 and 5.1.3. A cobalt wedge with linearly increasing thickness from $0 - 7$ nm was grown on PMN-PT (011). X-ray diffraction measurements on the Co/PMN-PT bilayer showed, that the Co thin film grows face centered cubic (fcc) textured with [111] for the OOP direction, see Fig. 6.2. The only observable peak using the Cu K_α line as source was at 44.35° corresponding to the 100% intensity peak of fcc Co, nominally at 44.27°[142]. Other peaks, such as the 45% intensity (200) fcc peak at 51.58° or the 100% intensity (101) peak for hexagonal close packed cobalt at 47.46° were absent. Hexagonal close packed cobalt has a 27% intensity peak (002) at 44.54°, that can not be completely excluded [143]. A capping of 2 nm Cr prevents oxidation while a 30 nm Au film on the back of the substrate serves as bottom electrode.

The XMCD measurements were carried out at the X-Treme beamline at the Swiss Light Source, Paul Scherrer Institut, Switzerland and at beamline 6.3.1 at the Ad-

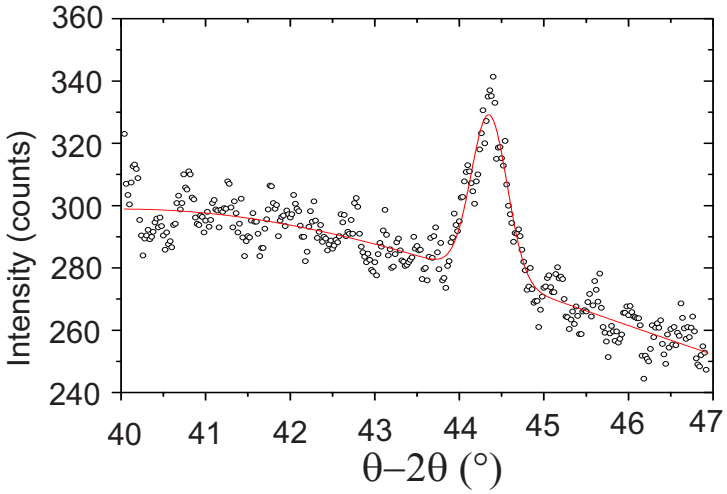

Figure 6.2: XRD of cobalt thin film on top of PMN-PT.

vanced Light Source, Lawrence Berkeley National Laboratory, California, USA (see also section 3.4.1). Spectra were recorded at room temperature with x-rays incident on the surface at an angle of 60°, measuring the projected magnetization along the $[01\bar{1}]$ crystal direction of the PMN-PT. XMCD hysteresis curves were measured in TEY mode while XMCD spectra were measured via TFY with a photodiode that is mounted perpendicular to the incoming x-rays, as indicated in Fig. 6.1. From all XAS spectra a constant background was subtracted at the pre-edge, the spectra of each polarization where normalized at the post-edge and XMCD difference spectra $(c_+ - c_-)$ were normalized to the L_3 XAS peak height.

6.1.2 Strain mediated magnetoelectric coupling

Figure 6.3 depicts representative XAS spectra for $c+$ and $c-$ polarized light taken along the [100] direction and XMCD spectra along the in-plane [100] and $[01\bar{1}]$ directions, both in remanence and at 2T in saturation. [100] is the direction of easy magnetization, its remanence value is close to saturation. Co $L_{3,2}$ hysteresis loops along the $[01\bar{1}]$ direction, taken for IP and OOP poled PMN-PT configurations are shown in Fig. 6.4. Electrical switching of the FE PMN-PT from an OOP poled to an IP poled state (explained in section 2.1.2), induces the development of a magnetic easy axis in the adjacent Co top layer as seen in Fig. 6.4 (a) for a nominal Co thickness of 3.5 nm. The same behaviour is observed probing a thicker part of the wedge at a nominal Co thickness of 6.3 nm in Fig. 6.4 (b). Since strain is a 'bulk'

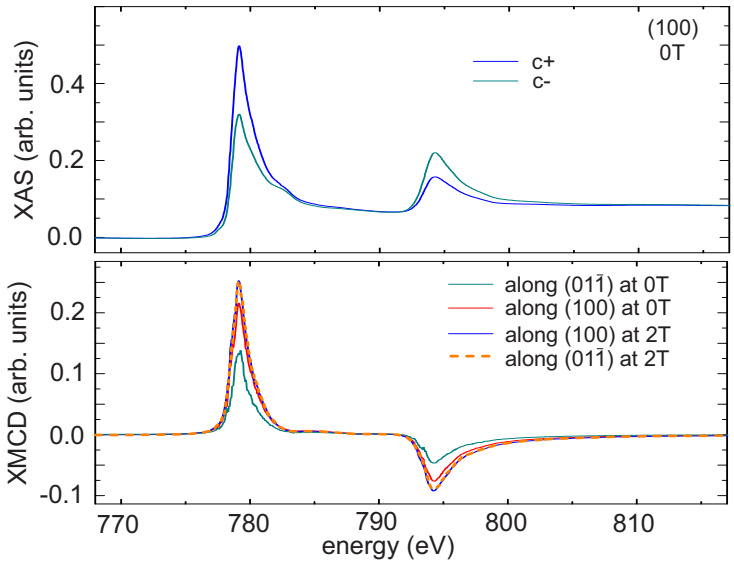

Figure 6.3: Top: Co XAS along the [100] direction. Bottom: Co XMCD at remanence along the in-plane [01$\bar{1}$] (green) and [100] (red) directions. XMCD at saturation is also depicted (blue and orange curves).

effect, it is visible at both the thinner and the thicker part of the wedge.

6.1.3 Dependence on the polarity of the substrate

There is another, more subtle, change in the magnetic anisotropy as shown by comparing hysteresis curves taken for oppositely OOP poled FE on the thinner part of the wedge, see Fig. 6.5(a). This effect cannot be attributed to a piezoelectric-magnetostrictive coupling since the structure of PMN-PT in the two OOP poled states is equivalent. Moreover, this anisotropy change is not observed in the thicker part of the wedge (Fig. 6.5(b)) hinting that this second effect is present at the interface between Co and PMN-PT and not throughout the whole Co film thickness: since TEY detection is very surface sensitive, at this larger Co thickness we no longer probe the interface region. For a quantitative analysis, XMCD spectra were taken at magnetic remanence after saturation in 2 T and sweeping the applied voltage across the FE. An example for oppositely poled PMN-PT states is shown in Fig. 6.6. Sum rule analysis was used to extract the projected magnetic moment $m_{\mathrm{tot}} = m_{\mathrm{s,eff}} + m_{\mathrm{orb}}$. The sum rules integration procedure was illustrated in Fig. 3.4 of section 3.2.2. The resulting dependence on the electric field is given in Fig. 6.7, where the grey curve links successive measurements. m_{tot} is strongest

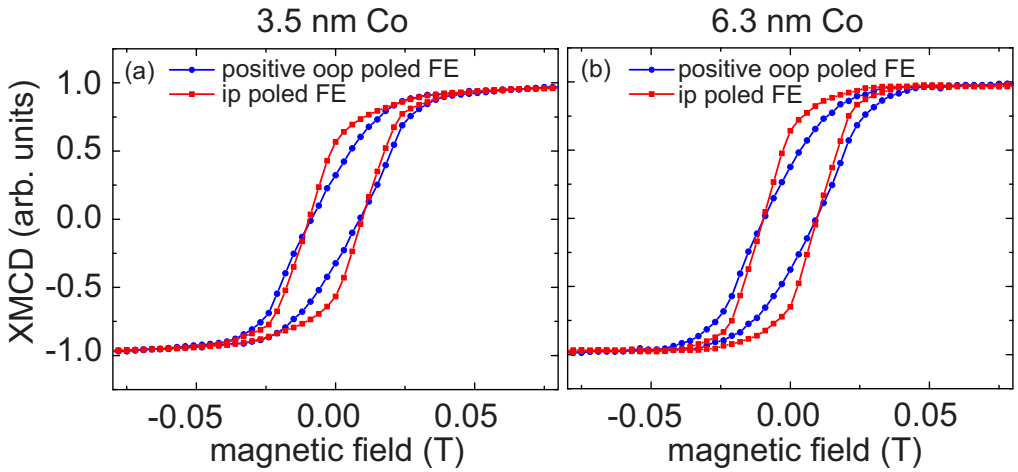

Figure 6.4: XMCD Co hysteresis curves probing the $[01\bar{1}]$ PMN-PT crystal direction for IP and OOP poled PMNPT (011). (a) probes a nominal Co thickness of 3.5 nm, (b) probes a nominal thickness of 6.3 nm. Upon switching the FE polarization from an OOP (blue curve) to an IP poled state (red curve), a magnetic easy axis develops.

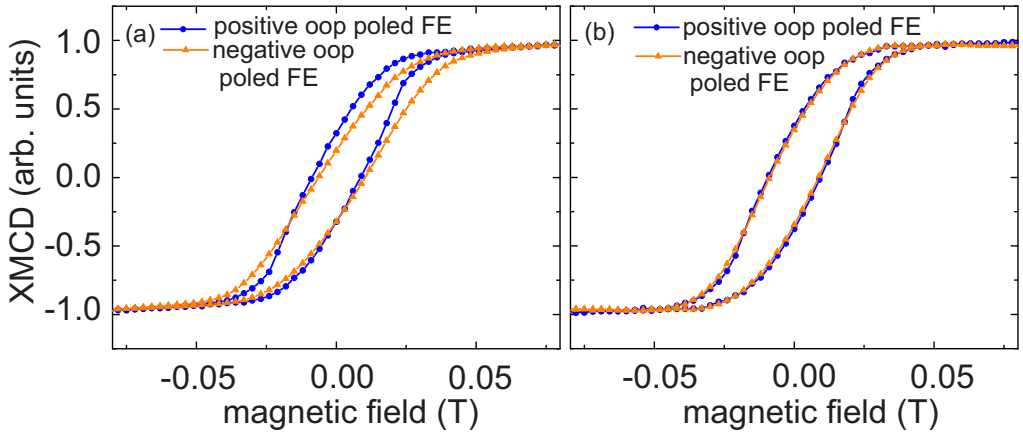

Figure 6.5: XMCD Co hysteresis curves probing the $[01\bar{1}]$ PMN-PT crystal direction for oppositely OOP poled FE polarization states. (a) probes a nominal Co thickness of 3.5 nm. Opposite OOP poled polarization directions exhibit also different anisotropies. (b) probes a thicker part of the wedge at 6.3 nm. The anisotropy change for oppositely OOP poled FE due to interface charge screening is now absent.

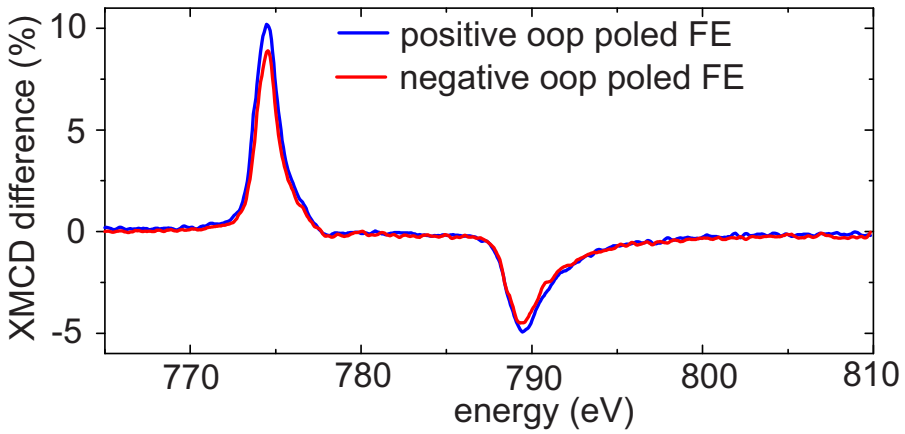

Figure 6.6: Co XMCD spectra taken at remanence for oppositely OOP poled FE.

at the coercive electric field, where the FE polarization rotates in-plane. Comparing the measurements of oppositely poled FE, negatively OOP poled PMN-PT results in a smaller Co total magnetic moment than positively OOP poled PMN-PT. Here, m_{tot} depends solely on the FE polarization state that the PMN-PT has been set in, irrespective of an actively applied bias voltage. The orbital moment is very small compared to the effective spin moment, yielding $m_{\mathrm{orb}} = 0.065 \pm 0.005\ \mu_{\mathrm{B}}$ for positive OOP poled PMN-PT, $m_{\mathrm{orb}} = 0.045 \pm 0.007\ \mu_{\mathrm{B}}$ for negative OOP poled PMN-PT and $m_{\mathrm{orb}} = 0.079 \pm 0.013\ \mu_{\mathrm{B}}$ for IP poling. At 2 T along the easy (100) direction, the effective spin moment $m_{\mathrm{s,eff}} = 1.639 \pm 0.164\ \mu_{\mathrm{B}}$ and orbital moment $m_{\mathrm{orb}} = 0.131 \pm 0.002\ \mu_{\mathrm{B}}$ compare well with literature [108, 144]. We also find that at 2 T applied field no dependence on the FE polarization can be observed.

6.2 Discussion

The impact of the FE order of PMN-PT (011) on the electronic and atomic structure of a Co top layer is twofold. The switching from an OOP to an IP poled configuration is accompanied by a biaxial structural change in the PMN-PT. The magnetic easy axis along the [100] direction for OOP poled PMN-PT as well as the development of an easy axis along $[01\bar{1}]$ upon IP poling can be qualitatively understood in terms of the negative magnetostriction of cobalt in response to the lattice parameter changes of the PMN-PT. Figure 6.8 shows a schematic of the in-plane strain exerted on the cobalt fcc unit cell for different poling directions. On the left side we show a piezo-

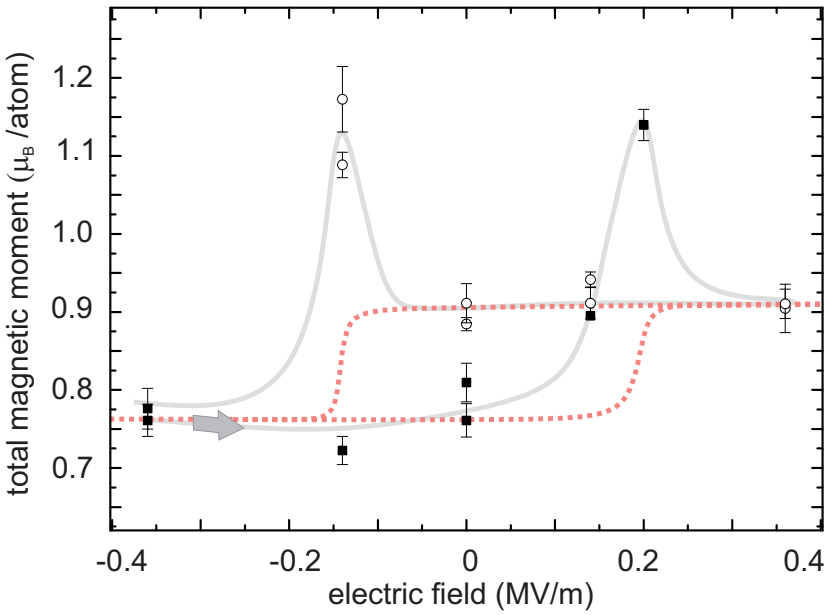

Figure 6.7: Total magnetic moment obtained from sum rules analysis as a function of applied electric field. The grey curve is a guide for the eye to link consecutive measurements and the arrow indicates the sweeping direction. Black squares (open circles) indicate measurements coming from negative (positive) OOP poling. The red curve represents the charge-only contributions to m_{tot}. At the coercive electric field, additional strain contributions are at play.

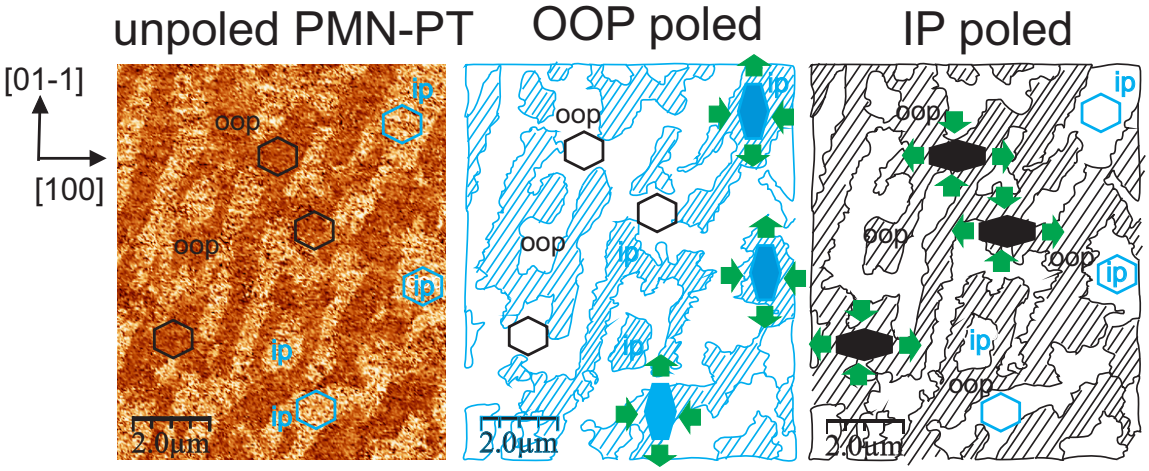

Figure 6.8: Schematic of the in-plane strain exerted to the cobalt fcc unit cell for different poling directions. On the left side, an in-plane phase piezo-force microscopy image is shown, highlighting the distribution of IP (light)/OOP(dark) domains for PMN-PT in the initial unpoled state before growth of the Co film.

force microscopy image[2] exhibiting a characteristic domain configuration of unpoled PMN-PT before the Co film deposition, where bright (dark) regions correspond to in-plane (out of plane) poled domains. XRD measurements showed that Co grows fcc textured with [111] oop direction. Consider a Co film grown on PMN-PT with roughly 50/50 IP/OOP poling ratio. The in-plane projection of the Co fcc unit cell along [111] is indicated by the black (on OOP poled PMN-PT domains) and blue (on IP PMN-PT domains) hexagons. The XRD space maps shown in chapter 5.1.3 showed that the largest strain exerted on a top layer upon poling from OOP to IP lies along the [100] direction (about 1% tensile strain). Vice versa, IP→OOP poling is accompanied by −1% compressive strain. The sketch in the center of Fig. 6.8 depicts the strain exerted on a Co top layer upon poling the PMN-PT OOP. The ferroelectric polarization of domains, originally in an IP configuration (blue hatched area) will be forced to rotate, hence cobalt grown on IP domains compresses along the [100] direction. With a negative magnetostriction constant for cobalt (see section 2.2.2), those domains contribute to the development of an easy axis along the [100] direction. The sketch on the right side in Fig. 6.8 depicts the situation for subsequent IP poling. When poling from OOP to IP, all constrained cobalt unit cells grown on IP poled PMN-PT domains will relax to their initial strain state, while all cobalt fcc unit cells originally grown on OOP poled domains (black hatched area) will be forced to strain tensile along [100]. Tensile strain along [100] implies that the direction perpendicular, i.e. $[01\bar{1}]$, becomes an easy magnetization axis. Wu et al. [145] have reported magneto-optical Kerr effect (MOKE) measurements on a Ni/Pt/PMN-PT structure, and observe the development of a hard axis along the $[01\bar{1}]$ direction upon in-plane poling. Due to the thick Pt electrodes between Ni and PMN-PT they solely observe strain mediated magnetoelectric coupling.

In contrast, charge mediated ME coupling is also present in the Co wedge/PMN-PT structure. The contribution of charge to the change in total magnetic moment is highlighted by superposing a ferroelectric hysteresis loop (red) as guide to the eye in Fig. 6.7. We observe a hysteretic behaviour of m_{tot} for positively and negatively OOP poled FE corresponding to accumulation and depletion of electrons at the FM/FE interface. Deviations from this hysteresis curve occur only at the coercive electric field, where the IP FE poling exerts a strain on the Co film leading to changes in magnetoelastic anisotropy and where no net surface charge should be present with a FE polarization oriented parallel to the surface plane. Comparing positively and negatively OOP poled FE no lattice parameter change is expected, the only difference being the polarity of the bound charge at the interface with the cobalt. Two previous

[2]Collaboration with Nicolas Pilet, NanoXAS beamline at the Swiss Light Source, Paul Scherrer Institut (Switzerland).

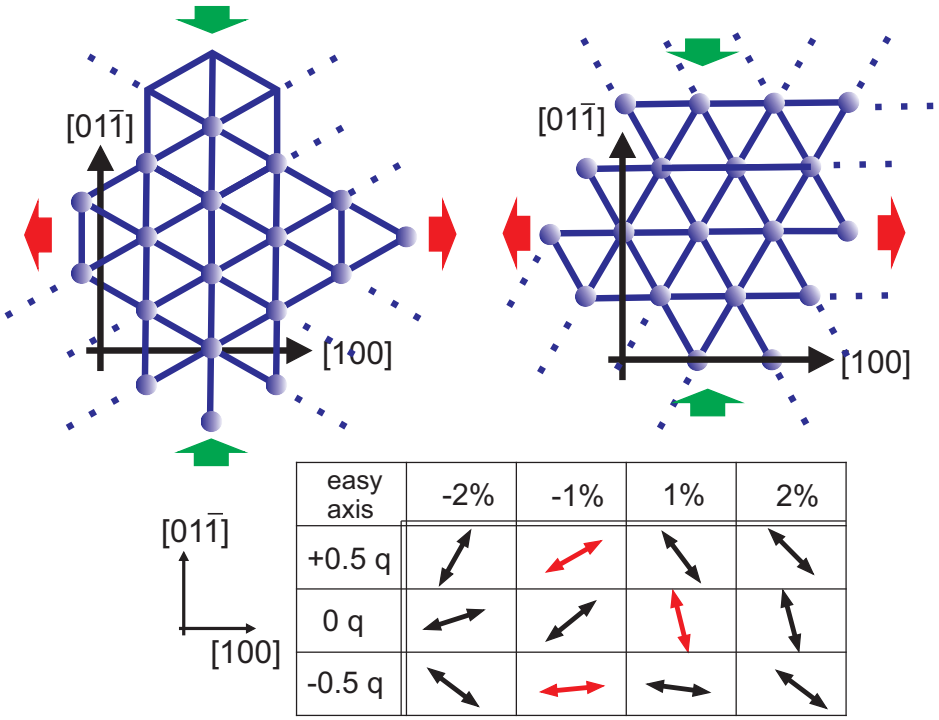

Figure 6.9: DFT calculations (in preparation for publication) of fcc (111) Co are carried out for two orientation configurations that differ by an angle of 30° with respect to the [100] direction in the surface plane. Green and red arrows indicate the application of in-plane strain exerted on the supercells (here, to simulate FE IP poling). The table depicts the resulting orientation of the magnetic easy axis as a function of in-plane strain and band filling. Easy axes, highlighted by red arrows, correspond to experimentally probed configurations of Co on positively OOP poled PMN-PT (top row), IP poled PMN-PT (middle row) and negatively OOP poled PMN-PT (bottom row), respectively.

studies [139, 140] used MOKE on samples of varying thickness to distinct between dominating magnetoelastic contribution in thick samples compared to an onset of surface anisotropy contribution in thinner samples[3]. The wedge geometry in this study allows us to distinguish between both anisotropy contributions in the same heterostructure.

So far, only phenomenological models have been used to explain the change in anisotropy due to charge screening. XMCD allows to give quantitative values regarding the change in total magnetic moment due to magnetoelastic contributions

[3]Note that in contrast to our study, Hu et al. [140] did not observe a FE polarity dependence for the Co magnetization at remanence in a Co/$BaTiO_3$ structure.

and due to the charge screening. In order to explain the nature and the mechanism of the observed anisotropy changes, ab-initio density functional theory calculations were carried out in a collaboration[4] (in preparation for publication). The theoretical approach to model the (111) textured but otherwise polycrystalline cobalt thin film considered two cases of orientation with respect to the single crystalline PMN-PT (011). Figure 6.9 shows a projection of the Co fcc unit cell on the (111) plane with Co atoms (in blue) at the center and at the corners of hexagons. On the left side the [100] direction points along the height of an equilateral triangle, on the right side nearest neighbours line up along the [100] direction. In other words the second configuration is rotated by 30° with respect to the first one and to the orthogonal PMN-PT crystal axes. Assuming no preferential in-plane orientation of polycrystalline Co during growth, all rotated configurations in between these two cases are equally possible. DFT calculations were carried out for the two depicted configurations.

For each configuration, a supercell representing fcc cobalt was strained within the (111) plane simulating the epitaxial constraints deducted from the space maps on the lattice parameter changes in PMN-PT (011) (section 5.1.3, table 5.2), indicated by the red and green arrows in Fig. 6.9. It was assumed that OOP and IP FE poling exerts strain on the adjacent polycrystalline Co layer as sketched in Fig. 6.8. The configurations in Fig. 6.9 were strained in the (111) plane in steps of ±1% where tensile strain refers to IP poling and compressive strain refers to OOP poling. For each calculation the c-axis was allowed to relax.

Finally, we calculate the angular dependence of the magnetocrystalline anisotropy as a function of the lateral strain by utilizing the magnetic force theorem [146, 147]. Consequently, the energetic change from a rotating magnetization is obtained by the differences of the full relativistic band energy sums at constant Kohn-Sham potential. Since no preferential in-plane orientation of polycrystalline Co exists, the calculations for the two extreme configurations depicted in Fig. 6.9 were averaged. For bulk Co, the calculations give [111] as the direction of easy magnetization. The in-plane magnetization of the Cobalt wedge on PMN-PT, obtained experimentally, can be ascribed to shape anisotropy. For zero strain, no anisotropy exists within the (111) plane. Checking different projection directions within the (111) plane for supercells as a function of lateral strain, an in-plane anisotropy develops; the easy axis is extracted and shown in the table in Fig. 6.9 ('0 q' case).

The strain dependence of the in-plane magnetocrystalline anisotropy was also calculated for supercells with altered electron count (±0.5 e/u.c.) (while overall charge neutrality of the supercell was accounted for) to simulate the influence of changes in band filling due to charge screening as it occurs at FM/FE interfaces.

[4]Michael Fechner, ETH Zürich, Switzerland.

Adding or subtracting charge from the supercell changes the orbital occupation and hence the band structure and hence the anisotropy, as well. The anisotropy behaviour for electron accumulation and depletion (averaged over both growth configurations) is also shown in the table in Fig. 6.9 ('+0.5 q' and '-0.5 q' case for accumulation and depletion). What follows, is a comparison of experiment and calculations. The XMCD measurements along the $[01\bar{1}]$ direction gave a larger magnetic moment for the case of electron accumulation at the Co/PMN-PT interface compared to the case of electron depletion. This trend is also verified from the calculations summarized in the table in Fig. 6.9: Comparing the first row (increased band filling) with the third row (reduced band filling) the projection of the easy axis on the $[01\bar{1}]$ direction is always higher for the case of electron accumulation. As illustrated in Fig. 6.8, OOP poling refers to compressive strain of about $\sim -1\%$. The calculated easy axes for opposite OOP poling that resemble the strain/charge situation found in the experiment are highlighted by red arrows. On the other hand, IP poling refers to the application of about $\sim 1\%$ tensile strain along [100], while no net charge is present. The development of an easy axis upon FE IP poling as probed by XMCD is also the outcome of the DFT, the middle row of the table in Fig. 6.8 shows an easy axis almost collinear to the $[01\bar{1}]$ for the IP poled strain/charge scenario (highlighted in red). Overall, the experimentally obtained changes in Co anisotropy along the $[01\bar{1}]$ direction that arise from the coexistence of strain and charge can be traced back to changes in magnetoelastic and magnetocrystalline anisotropy, respectively. The calculations overestimate the magnetization changes that result upon comparison of electron accumulation and depletion. Since, at a FM/FE interface charge screening is fulfilled within the Thomas-Fermi screening length (about 1.5 Å [30]), the XMCD measurements probe both charged and charge neutral slabs.

6.3 Conclusion

The coexistence of strain- and charge mediated magnetoelectric coupling in a cobalt wedge on ferroelectric PMN-PT was studied with surface sensitive XMCD at the Co $L_{3,2}$ edge on a single substrate. Three distinct remanent magnetization states can be set in the Co film at room temperature. Electrical switching between those states induces changes in anisotropy. Quantitative values of the total magnetic moment are given for the anisotropy behaviour of each of the states. The magnetization changes can be attributed to changes in strain and/or the FE substrate polarization triggering changes in the magnetoelastic and magnetocrystalline anisotropy energy, respectively. The experimental results serve as an input for DFT calculations, that model the three-state scenario of entwined charge and strain for polycrystalline fcc

(111) textured cobalt very well.

Chapter 7

Conclusion and outlook

The aim of this thesis was to create artificial multiferroic composites where electrical switching of a ferroelectric component induces non-volatile changes in the magnetic constituent and to provide insight into the underlying coupling mechanisms.

Two of the systems discussed above benefited from the specific (011) crystal orientation of the relaxor ferroelectric PMN-PT substrate.

The study of the FM/FE heterostructure $La_{0.7}Sr_{0.3}MnO_3/[Pb(Mg_{1/3}Nb_{2/3})O_3]_{0.68}$ -$[PbTiO_3]_{0.32}$ (011) highlighted the magnetoelectric control of the double exchange interaction via strain. Reversible electrical switching of the FE polarization induces a 10 K shift of the magnetic Curie temperature T_C. A similar magnitude in T_C change has been previously only observed under applied electric fields [98] or under hydrostatic compression [88]. In contrast, the T_C shift observed in this study remains at switched-off bias voltage. Two distinct FE polarization configurations, normal and parallel to the surface plane, can be set in the ferroelectric substrate and are stable at remanence; reciprocal space maps highlight the accompanying lattice parameter changes which impose a biaxial strain on the manganite thin film. Hence, it is possible to study the magnetic properties of epitaxial LSMO as a function of strain on a single substrate in contrast to studies where LSMO was grown epitaxially on different substrates with distinct lattice mismatch and distinct chemical environment at the interface. The magnetic response to the strain changes is probed by temperature dependent Mn $L_{3,2}$ x-ray magnetic circular dichroism providing quantitative values of the Mn spin and orbital moment. X-ray natural linear dichroism spectra for both strain states probe changes in the valence charge anisotropy. MultiX multiplet calculations allow one to simulate strain dependent crystal field changes in LSMO: A comparison of strain values for PMN-PT upon poling shows that the strain values extracted from the RSMs yield a good agreement between the experimental

and calculated XNLD line shape and reproduce the XNLD increase upon switching, in contrast to strain values obtained by strain gauge measurements reported in literature. The latter can only provide strain values along two independent in-plane directions, and may underestimate the absolute strain values since the piezoresponse of the substrate can be attenuated through thick layers of glue or thick electrodes. Multiplet and density functional theory calculations support the picture that the existing population imbalance between out of plane and in plane oriented orbitals increases further with tensile strain, favoring orbital occupation in the surface plane. An increase in tensile in-plane strain leads to an increased energy difference between the two e_g orbitals and a larger Mn-O-bond length. Increasing the electron-lattice coupling and reducing the e_g electron itinerancy that leads to ferromagnetism due to the double exchange interaction, results ultimately in lower T_C values in agreement with the Millis model.

In the epitaxial LSMO/PMN-PT system, the PMN-PT lattice parameter changes influence the double exchange mechanism in the LSMO.

In the Co/PMN-PT (011) system, the role of the PMN-PT is twofold: Upon FE switching, both strain and bound charge influence the magnetic response of the fcc (111) textured cobalt top layer. Three distinct remanent magnetization states can be set in the cobalt film at room temperature corresponding to three distinct ferroelectric poling orientations. If the ferroelectric polarization is switched from an OOP poled state to the IP poled state, the corresponding lattice parameter changes in the PMN-PT exert a strain on the cobalt top layer resulting in a higher remanent magnetization along the $[01\bar{1}]$ direction. Comparing oppositely OOP poled FE, an additional anisotropy change is observed; since the structure of PMN-PT in the two OOP poled states is equivalent, no lattice parameter changes are expected and the change in anisotropy behaviour must stem from the substrate polarity. The bound charge at the interface is expected to be screened by the cobalt metal within the Thomas Fermi screening length of a few Angstroms. We use a Co wedge geometry to study the magnetic response as a function of Co layer thickness employing XMCD with surface sensitive total electron yield detection. Consequently, the anisotropy change induced by the charged substrate is observed for the thinner part but absent in the thicker part of the Co wedge. Hence, we can disentangle interface (charge) and bulk (strain) contributions to the Co anisotropy. Quantitative values of the total magnetic moment are given for the three distinct remanent magnetization states.

Lattice parameter values for cobalt and PMN-PT obtained by x-ray diffraction as well as domain distributions obtained from atomic force microscopy serve as an input for DFT calculations which reproduce the experimentally observed anisotropy behaviour for fcc (111) textured cobalt as a function of the lateral strain and charge.

The strain dependence of the in-plane magnetocrystalline anisotropy was also calculated for supercells with altered electron count (± 0.5 e/u.c.) (while overall charge neutrality of the supercell was accounted for) to simulate the influence of changes in band filling due to charge screening as it occurs at FM/FE interfaces. It is found that the experimentally observed three-state scenario of entwined charge and strain for polycrystalline fcc (111) textured cobalt is reproduced very well by DFT. Beforehand, only phenomenological approaches [139, 140, 141] were reported on the coexistence of different ME coupling mechanisms in a single system. The Co electron DOS screens the FE polarization at the interface resulting in changes in the orbital occupation and hence the band structure and hence the magnetocrystallline anisotropy, as well. The study of the Co/PMN-PT (011) system unravels how magnetoelasticity and interfacial charge density trigger changes in the magnetic anisotropy. The coexistence of multiple coupling mechanisms opens up a route to tune and enhance magnetoelectric cross-coupling between layers in heterostructures.

While in the heterostructures investigated above, both layers of a two-component system exhibit a memory function on their own, an alternative strategy in creating an artificial multiferroic composite is to induce ferromagnetism in a PM/FE heterostructure via charge doping. This approach could enable electrical switching between FM/non-FM states. For palladium with a Stoner parameter slightly short of fulfilling the condition for ferromagnetism it was proposed [62, 64] that a shift of the Fermi level to slightly lower energies could induce magnetism. Here, a modulation of the charge carrier density via an adjacent FE PZT layer was envisaged. For all measured nanostructures the displacement current upon switching was monitored in-situ both at X-Treme and at PHOENIX and the Pd film surface seemed to be continuous as shown by the AFM data. However, no XMCD difference signal upon ferroelectric switching was found within the noise ratio of 0.2% at the $M_{3,2}$ edge and of 1% at the $L_{3,2}$ edge.

To exclude that there is ferromagnetism present in the Pd/PZT system, the experiments at the $L_{3,2}$ edge (where the XAS signal arises solely from Pd) would necessitate a setup that can reach lower temperatures, than the 65 K employed in this thesis. Also, high magnetic fields of several Tesla would be of advantage. Measurements employing XLD could clarify whether there are non-collinear spin configurations with no net magnetization present. Regarding the sample quality, a dead layer or spurious contamination at the PZT surface cannot be excluded, at the moment. Also, the PZT surface roughness could influence competing energy terms during growth and affect the single crystalline Pd growth on top of PZT. A better control of the PZT surface roughness could for example be achieved by molecular beam epitaxial growth.

Further research will be required to demonstrate electric field control of magnetism in Pd. In this regard we anticipate that hybridization at the interface and strain resulting from lattice mismatch are the key parameters to modulate the density of states in Pd. One could try other ferroelectrics such as $BaTiO_3$, $PbTiO_3$, $BiFeO_3$ or PMN-PT with different in-plane lattice mismatch and different hybridization formation between substrate and top layer.

Regarding the modulation of the electron DOS at the Fermi level, PZT prepared by molecular beam epitaxy can reach much higher polarizations of $P = 85\ \mu C/cm^2$ [127], $BaTiO_3$ reaches up to $P = 70\ \mu C/cm^2$ [128], $PbTiO_3$ reaches $P = 75\ \mu C/cm^2$ [37], for $BiFeO_3$ values of $P = 150\ \mu C/cm^2$ [129] have been reported. Another route to proceed would be to investigate a field effect structure, for example Pd on paraelectric $SrTiO_3$, where the induced charge at the interface can be varied continuously.

In summary, this thesis investigated magnetoelectric coupling mechanisms in artificial multiferroic composites for a range of material combinations. For Pd/PZT, a first experimental approach to electric field control of magnetism in Pd is described, but no conclusive results were achieved. In the LSMO/PMN-PT system, the measurements demonstrate *non-volatile*, electric field induced, strain mediated changes in the double exchange interaction responsible for ferromagnetism. Regarding the Co/PMN-PT system, our results evidence the coexistence of two coupling mechanisms leading to three distinct magnetization states upon electrical switching.

Thank you so much

Now is the time to thank YOU for making these four years at PSI such a great experience for me. First of all: The warmest thank you for making it all possible, Frithjof.

To overcome the accumulation of students at the PEEM, Frithjof delegated me away from the beautiful images I had already become acquainted with to Xtreme. Thank you for that! With a beamline scientist and two postdocs as direct supervisors, it was a most luxurious surrounding for me to learn from skilled and clever people that love their job.

Cinthia, it was supercool to learn from you and to work with you thanks to the positive attitude you bring along with all your skills. It gives one the feeling that all is (or will be then) possible (at the allocated beam time). I admire your efficiency with the many '20 min for problem solving until the last bus leaves' I have witnessed. In the end, me being so convinced about the X-Treme beamline ('L_3 edge only! Aah, we can do better than that!' at conferences) is being convinced about you. It is really fun to work with you, even if we try the 10th desperate permutation of 'Connect the LO to common and the common to GND through the BNC/Triax adapter and the HI to the back of the sample...'.
The deluxe in-house possibilities to unexpectantly win some right-after-commissioning beamtime allowed for the invaluable work strategy I learned from Carlos, in german we would call it 'to always have another iron in the fire'. I was highly motivated to start collaborations.

I thank you, Frithjof, for your encouraging way and all your help how to approach or improve and sell a project, or whom to approach for this and that missing measurements or calculations. Thanks to your positive attitude as a supervisor I felt very enthusiastic about my projects and got the reassuring impression that you also trust that there will be a positive outcome. And also thank you and PSI for all the opportunities I could seize, JEMS, SPS, InMRAM, Berkley, Lungern, how to give a good talk,...

I was very lucky that Rajesh Chopdekar was around at PSI, who shared not only

cool project ideas with me, but also went and grew samples (and they did work, of course). I'm thankful for his suggestions and sharing of know-how and that he took me to join his measurements at the ALS in Berkley and also for the careful reading of my thesis.

With Carlos Vaz I've already worked together before my time at PSI, so I was really happy, when it turned out that he would also stay at PSI. Our conversations added a lot to both my work and personal life strategy. Thank you for all your help. And that you always found time to discuss questions and possibilities how to measure missing pieces of information. Thank you also for your thesis corrections and suggestions.

Through all times it was a pleasure to have the MM team around. The inspiring lunch talks how everything works in his or her respective home countries Portugal, Spain, Italy, Northern Germany, Israel, Brazil, India, the US, ... and the daily news viewed from the many nations' perspectives was the coolest experience at an international research center such as PSI. Thank you all for times of fondue, BBQ and after-work beer, time macchine and more solid discussions, or just times of coffee and ice cream.

Michele (Buzzi) and Aurora (Alberca Carretero), thank you for your altruistic way of thinking, a real researchers skill, such that you help and get involved if you think it could add to the subject (it did).

Thank you, Michael (Fechner) for your enthusiasm and work on checking out the strain-charge-interplay!

Thank you Miguel (Uribe Laverde) for all your help and all the hours you spent for PMN-PT.

Thank you, Greta (Radaelli) for all your efforts in our LSMOp5/BTO collaboration upon electrical switching.

Thank you, Andi (Quindeau), Jochen (Stahn) and Michel (Kenzelmann) for letting me join in the investigations of the Co/PZT/LSMO tunneljunctions.

Many thanks to Ann-Christine (Uldry) for explaning the multiX code and Bernhard (Delley) for your help on the Mn orbital occupation.

And many thanks to the many in-house people at PSI that advised me and supported my work, Christof Schneider, Thomas Huthwelker, Marcus Schmidt, Nicolas Pilet, Peter Warnicke, Ekaterina Pomjakushina, Michael Horisberger.

And in the end I want to thank my family, luckiest me to have you in my life.

List of publications

[1] C. Piamonteze, M. Gibert, J. Heidler, J. Dreiser, S. Rusponi, H. Brune, J.-M. Triscone, F. Nolting, and U. Staub. *Phys. Rev. B* **92**, 014426 (2015).

[2] A. Bisig, M.-A. Mawass, M. Stärk, C. Moutafis, J. Rhensius, J. Heidler, S. Gliga, M. Weigand, T. Tyliszczak, B. Van Waeyenberge, H. Stoll, G. Schütz, and M. Kläui. *Appl. Phys. Lett.* **106 (12)**, 122401 (2015).

[3] J. Heidler, C. Piamonteze, R. V. Chopdekar, M. A. Uribe-Laverde, A. Alberca, M. Buzzi, A. Uldry, B. Delley, C. Bernhard, and F. Nolting. *Phys. Rev. B* **91**, 024406 (2015).

[4] J. Dreiser, A. M. Ako, C. Wäckerlin, J. Heidler, C. E. Anson, A. K. Powell, C. Piamonteze, F. Nolting, S. Rusponi, and H. Brune. *J. Phys. Chem. C* **119 (7)**, 3550 (2015).

[5] M. A. Uribe-Laverde, S. Das, K. Sen, I. Marozau, E. Perret, A. Alberca, J. Heidler, C. Piamonteze, M. Merz, P. Nagel, S. Schuppler, D. Munzar, and C. Bernhard. *Phys. Rev. B* **90**, 205135 (2014).

[6] A. Bisig, M. Stärk, M. Mawass, C. Moutafis, J. Rhensius, J. Heidler, F. Büttner, M. Noske, M. Weigand, S. Eisebitt, T. Tyliszczak, H. Van Waeyenberge, B.and Stoll, G. Schütz, and M. Kläui. *Nat. Commun.* **4**, 2328 (2013).

[7] R. Chopdekar, J. Heidler, C. Piamonteze, Y. Takamura, A. Scholl, S. Rusponi, H. Brune, L. J. Heyderman, and F. Nolting. *Eur. Phys. J. B* **86 (6)**, 241 (2013).

[8] P. Wohlhüter, J. Rhensius, C. A. F. Vaz, J. Heidler, H. S. Körner, A. Bisig, M. Foerster, L. Mechin, F. Gaucher, A. Locatelli, M. A. Niño, S. El Moussaoui, F. Nolting, E. Goering, L. J. Heyderman, and M. Kläui. *J. Phys. Condens. Matter* **25 (17)**, 176004 (2013).

[9] Y. Lisunova, J. Heidler, I. Levkivskyi, I. Gaponenko, A. Weber, C. Caillier, L. J. Heyderman, M. Kläui, and P. Paruch. *Nanotechnology* **24**, 105705 (2013).

[10] J. Heidler, J. Rhensius, C. A. F. Vaz, P. Wohlhüter, H. S. Körner, A. Bisig, S. Schweitzer, A. Farhan, L. Mechin, L. Le Guyader, F. Nolting, A. Locatelli, M. A. Niño, F. Kronast, L. J. Heyderman, and M. Kläui. *J. Appl. Phys.* **112**, 103921 (2012).

[11] C. Piamonteze, U. Flechsig, S. Rusponi, J. Dreiser, J. Heidler, M. Schmidt, R. Wetter, M. Calvi, T. Schmidt, H. Pruchova, J. Krempasky, C. Quitmann, H. Brune, and F. Nolting. *J. Synchrotron Radiat.* **19 (5)**, 661 (2012).

[12] J. Rhensius, C. A. F. Vaz, A. Bisig, S. Schweitzer, J. Heidler, H. S. Körner, A. Locatelli, M. A. Niño, M. Weigand, L. Mechin, F. Gaucher, E. Goering, L. J. Heyderman, and M. Kläui. *Appl. Phys. Lett.* **99 (6)**, 062508 (2011).

[13] C. A. F. Vaz, J. Rhensius, J. Heidler, P. Wohlhüter, A. Bisig, H. S. Körner, T. O. Mentes, A. Locatelli, L. Le Guyader, F. Nolting, T. Graf, C. Felser, L. J. Heyderman, M. Kläui. *Appl. Phys. Lett.* **99 (18)**, 182510 (2011).

[14] S. Glawion, J. Heidler, M. W. Haverkort, L. C. Duda, T. Schmitt, V. N. Strocov, C. Monney, K. J. Zhou, A. Ruff, M. Sing, and R. Claessen. *Phys. Rev. Lett.* **107**, 107402 (2011).

[15] M. Sing, S. Glawion, M. Schlachter, M. R. Scholz, K. Goß, J. Heidler, G. Berner, and R. Claessen. *Phys. Rev. Lett.* **106**, 056403 (2011).

Bibliography

[1] H. Schmid. *Ferroelectrics* **162 (1)**, 317 (1994).

[2] I. E. Dzyaloshinskii. *Zh. Eksp. Teor. Fiz.* **37**, 881 (1959).

[3] D. N. Astrov. *Zh. Eksp. Teor. Fiz.* **38**, 984 (1960).

[4] E. Ascher, H. Rieder, H. Schmid, and H. Stössel. *J. Appl. Phys.* **37 (3)**, 1404 (1966).

[5] R. P. Santoro, D. J. Segal, and R. E. Newnham. *J. Phys. Chem. Solids* **27 (67)**, 1192 (1966).

[6] D. N. Astrov, B. I. Al'shin, R. Zorin, and L. A. Drobyshev. *JETP* **28 (6)**, 1123 (1969).

[7] M. Fiebig. *J.Phys. D Appl. Phys.* **38 (8)**, R123 (2005).

[8] G. A. Smolenskii and I. E. Chupis. *Sov. Phys. Uspekhi* **25 (7)**, 475 (1982).

[9] C. A. F. Vaz, J. Hoffman, C. H. Ahn, and R. Ramesh. *Adv. Mater.* **22 (26-27)**, 2900 (2010).

[10] N. Spaldin, S.-W. Cheong, and R. Ramesh. *Phys. Today* **63 (10)**, 38 (2010).

[11] C. A. F. Vaz. *J. Phys. Condens. Mat.* **24 (33)**, 333201 (2012).

[12] S. Mathews, R. Ramesh, T. Venkatesan, and J. Benedetto. *Science* **276 (5310)**, 238 (1997).

[13] M. Gajek, M. Bibes, S. Fusil, K. Bouzehouane, J. Fontcuberta, A. Barthélémy, and A. Fert. *Nat. Mater.* **6 (4)**, 296 (2007).

[14] J. D. Burton and E. Y. Tsymbal. *Phys. Rev. Lett.* **106**, 157203 (2011).

[15] J.-M. Hu, Z. Li, L.-Q. CHen, and C.-W. Nan. *Nat. Commun.* **2**, 553 (2011).

[16] J. Hemberger, A. Krimmel, T. Kurz, H.-A. Krug von Nidda, V. Y. Ivanov, A. A. Mukhin, A. M. Balbashov, and A. Loidl. *Phys. Rev. B* **66**, 094410 (2002).

[17] Y. Wang, J. Hu, Y. Lin, and C.-W. Nan. *NPG Asia Mater.* **2**, 61 (2010).

[18] W. Eerenstein, M. Wiora, J. L. Prieto, J. F. Scott, and N. D. Mathur. *Nat. Mater.* **6 (5)**, 348 (2007).

[19] S. Zhang, Y. G. Zhao, P. S. Li, J. J. Yang, S. Rizwan, J. X. Zhang, J. Seidel, T. L. Qu, Y. J. Yang, Z. L. Luo, Q. He, T. Zou, Q. P. Chen, J. W. Wang, L. F. Yang, Y. Sun, Y. Z. Wu, X. Xiao, X. F. Jin, J. Huang, C. Gao, X. F. Han, and R. Ramesh. *Phys. Rev. Lett.* **108**, 137203 (2012).

[20] T. Wu, P. Zhao, M. Bao, A. Bur, J. L. Hockel, K. Wong, K. P. Mohanchandra, C. S. Lynch, and G. P. Carman. *J. Appl. Phys.* **109 (12)**, 124101 (2011).

[21] C.-G. Duan, S. S. Jaswal, and E. Y. Tsymbal. *Phys. Rev. Lett.* **97**, 047201 (2006).

[22] J. D. Burton and E. Y. Tsymbal. *Phys. Rev. B* **80**, 174406 (2009).

[23] S. Valencia, A. Crassous, L. Bocher, V. Garcia, X. Moya, R. O. Cherifi, C. Deranlot, K. Bouzehouane, S. Fusil, A. Zobelli, A. Gloter, N. D. Mathur, A. Gaupp, R. Abrudan, F. Radu, A. Barthélémy, and M. Bibes. *Nat. Mater.* **10 (10)**, 753 (2011).

[24] P. Borisov, A. Hochstrat, X. Chen, W. Kleemann, and C. Binek. *Phys. Rev. Lett.* **94**, 117203 (2005).

[25] H. Béa, M. Bibes, F. Ott, B. Dupé, X.-H. Zhu, S. Petit, S. Fusil, C. Deranlot, K. Bouzehouane, and A. Barthélémy. *Phys. Rev. Lett.* **100**, 017204 (2008).

[26] H. J. A. Molegraaf, J. Hoffman, C. A. F. Vaz, S. Gariglio, D. van der Marel, C. H. Ahn, and J.-M. Triscone. *Adv. Mater.* **21 (34)**, 3470 (2009).

[27] C. A. F. Vaz, J. Hoffman, Y. Segal, J. W. Reiner, R. D. Grober, Z. Zhang, C. H. Ahn, and F. J. Walker. *Phys. Rev. Lett.* **104**, 127202 (2010).

[28] H. Xi, W. Yi, W. Ning, A. N. Caruso, E. Vescovo, K. D. Belashchenko, P. A. Dowben, and C. Binek. *Nat. Mater.* **9 (7)**, 579 (2010).

[29] S. M. Wu, S. A. Cybart, P. Yu, M. D. Rossell, J. X. Zhang, R. Ramesh, and R. C. Dynes. *Nat. Mater.* **9 (756)** (2010).

[30] S. Zhang. *Phys. Rev. Lett.* **83**, 640 (1999).

[31] M. Weisheit, S. Fähler, A. Marty, Y. Souche, C. Poinsignon, and D. Givord. *Science* **315 (5810)**, 349 (2007).

[32] C.-G. Duan, J. P. Velev, R. F. Sabirianov, Z. Zhu, J. Chu, S. S. Jaswal, and E. Y. Tsymbal. *Phys. Rev. Lett.* **101**, 137201 (2008).

[33] T. Maruyama, Y. Shiota, T. Nozaki, K. Ohta, N. Toda, M. Mizuguchi, A. A. Tulapurkar, T. Shinjo, M. Shiraishi, S. Mizukami, Y. Ando, and Y. Suzuki. *Nat. Nanotechnol.* **4 (3)**, 158 (2009).

[34] T. Zhao, S. R. Shinde, S. B. Ogale, H. Zheng, T. Venkatesan, R. Ramesh, and S. Das Sarma. *Phys. Rev. Lett.* **94**, 126601 (2005).

[35] J. Rondinelli, M. Stengel, and N. Spaldin. *Nat. Nanotechnol.* **3**, 46 (2008).

[36] I. Stolichnov, S. W. E. Riester, H. J. Trodahl, N. Setter, A. W. Rushforth, K. W. Edmonds, R. P. Campion, C. T. Foxon, B. L. Gallagher, and T. Jungwirth. *Nat. Mater.* **7 (6)**, 464 (2008).

[37] K. M. Rabe, M. Dawber, C. Lichtensteiger, C. H. Ahn, and J.-M. Triscone. In *Physics of Ferroelectrics*, Topics in Applied Physics vol. 105, pages 1–30, (Springer Berlin Heidelberg 2007).

[38] A. Safari, R. K. Panda, and V. F. Janas. *Key Eng. Mat.* **122**, 35 (1996).

[39] B. Noheda. *Curr. Opin. Solid St. M.* **6 (1)**, 27 (2002).

[40] X. Hao, J. Zhai, L. B. Kong, and Z. Xu. *Progress in Materials Science* **63 (0)**, 1 (2014).

[41] N. Tohge, S. Takahashi, and T. Minami. *J. Am. Ceram. Soc.* **74 (1)**, 67. ISSN 1551-2916 (1991).

[42] X. Hong, A. Posadas, A. Lin, and C. Ahn. *Phys. Rev. B* **68**, 134415 (2003).

[43] A. Bokov and Z.-G. Ye. *J. Mater. Sci.* **41 (1)**, 31 (2006).

[44] P. K. Davies and M. A. Akbas. *J. Phys. Chem. Solids* **61 (2)**, 159 (2000).

[45] T. R. Shrout and J. Fielding Jr. In *Ultrasonics Symposium, 1990. Proceedings., IEEE 1990 vol.2*, page 711 (1990).

[46] B. P. Burton, E. Cockayne, S. Tinte, and U. V. Waghmare. *Phase Transit.* **79 (1-2)**, 91 (2006).

[47] L. E. Cross. *Mater. Chem. Phys.* **43 (2)**, 108 (1996).

[48] Z.-G. Ye and H. Schmid. *Ferroelectrics* **145 (1)**, 83 (1993).

[49] Z.-G. Ye and M. Dong. *J. Appl. Phys.* **87 (5)**, 2312 (2000).

[50] B. Noheda, D. E. Cox, G. Shirane, J. Gao, and Z.-G. Ye. *Phys. Rev. B* **66**, 054104 (2002).

[51] S. Zhang and F. Li. *J. Appl. Phys.* **111 (3)**, 031301 (2012).

[52] J. Heidler, C. Piamonteze, R. V. Chopdekar, M. A. Uribe-Laverde, A. Alberca, M. Buzzi, A. Uldry, B. Delley, C. Bernhard, and F. Nolting. *Phys. Rev. B* **91**, 024406 (2015).

[53] K. H. J. Buschkow and F. R. de Boer. *Physics of magnetism and magnetic materials*, (Kluwer Academic, New York 2003).

[54] E. C. Stoner. *P. Phys. Soc. Lond. A: Mathematical, Physical and Engineering Sciences* **165 (922)**, 372 (1938).

[55] J. F. Janak. *Phys. Rev. B* **16**, 255 (1977).

[56] O. Gunnarsson. *J. Phys. F Met. Phys.* **6 (4)**, 587 (1976).

[57] J. G. Gay, J. R. Smith, F. J. Arlinghaus, and T. W. Capehart. *Phys. Rev. B* **23**, 1559 (1981).

[58] L. Fritsche, J. Noffke, and H. Eckardt. *J. Phys. F Met. Phys.* **17 (4)**, 943 (1987).

[59] H. Chen, N. E. Brener, and J. Callaway. *Phys. Rev. B* **40**, 1443 (1989).

[60] V. L. Moruzzi and P. M. Marcus. *Phys. Rev. B* **39**, 471 (1989).

[61] T. Ochs and C. Elsässer. *Z. Metallk.* **93 (5)**, 406 (2002).

[62] Y. B. Kudasov and A. S. Korshunov. *Phys. Lett. A* **364 (34)**, 348 (2007).

[63] V. Pankoke and S. Gemming. *Eur. Phys. J. B* **67 (1)**, 57 (2009).

[64] Y. Sun, J. D. Burton, and E. Y. Tsymbal. *Phys. Rev. B* **81**, 064413 (2010).

[65] R. M. Bozorth, P. A. Wolff, D. D. Davis, V. B. Compton, and J. H. Wernick. *Phys. Rev.* **122**, 1157 (1961).

[66] J. Crangle and W. R. Scott. *J. Appl. Phys.* **36 (3)**, 921 (1965).

[67] U. Gradmann and R. Bergholz. *Phys. Rev. Lett.* **52**, 771 (1984).

[68] N. Takano, T. Kai, K. Shiiki, and F. Terasaki. *Solid State Commun.* **97 (2)**, 153 (1996).

[69] M. T. Johnson, P. J. H. Bloemen, F. J. A. den Broeder, and J. J. de Vries. *Rep. Prog. Phys.* **59 (11)**, 1409 (1996).

[70] R. Skomski, A. Kashyap, J. Zhou, and D. J. Sellmyer. *J. Appl. Phys.* **97 (10)**, 10B302 (2005).

[71] S. Blundell. *Magnetism in Condensed Matter*, (Oxford Master Series in Condensed Matter Physics, Oxford 2001).

[72] B. D. Cullity and C. D. Graham. *Introduction to magnetic materials*, (John Wiley & Sons, New Jersey 2009).

[73] J. Stöhr and H. Siegmann. *Magnetism: From Fundamentals to Nanoscale Dynamics*, (Springer Series in Solid-State Sciences, Berlin Heidelberg 2006).

[74] R. M. Bozorth. *Phys. Rev.* **96**, 311 (1954).

[75] N. S. Akulov. *Z. Phys.* **66 (7-8)**, 533 (1930).

[76] H. B. Callen and N. Goldberg. *J. Appl. Phys.* **36 (3)**, 976 (1965).

[77] E. W. Lee. *Rep. Prog. Phys.* **18 (1)**, 184 (1955).

[78] R. C. O'Handley. *Modern magnetic materials: principles and applications*, (John Wiley & Sons, New York 2000).

[79] L. Alberts and H. L. Alberts. *Philosophical Magazine* **8 (96)**, 2101 (1963).

[80] W. Betteridge. *Progress in Materials Science* **24 (0)**, 51 (1980).

[81] E. Klokholm and J. Aboaf. *J. Appl. Phys.* **53 (3)** (1982).

[82] A.-M. Haghiri-Gosnet and J.-P. Renard. *J. Phys. D* **36 (8)**, R127 (2003).

[83] E. Dagotto, T. Hotta, and A. Moreo. *Phys. Rep.* **344 (13)**, 1 (2001).

[84] C. Zener. *Phys. Rev.* **82**, 403 (1951).

[85] J. Fink, E. Schierle, E. Weschke, and J. Geck. *Rep. Prog. Phys.* **76 (5)**, 056502 (2013).

[86] A. J. Millis, T. Darling, and A. Migliori. *J. Appl. Phys.* **83 (3)**, 1588 (1998).

[87] Y. Moritomo, A. Asamitsu, and Y. Tokura. *Phys. Rev. B* **51**, 16491 (1995).

[88] V. Moshnyaga, S. Klimm, E. Gommert, R. Tidecks, S. Horn, and K. Samwer. *J. Appl. Phys.* **88 (9)**, 5305 (2000).

[89] F. Tsui, M. C. Smoak, T. K. Nath, and C. B. Eom. *Appl. Phys. Lett.* **76 (17)**, 2421 (2000).

[90] A. Tebano, C. Aruta, P. G. Medaglia, F. Tozzi, G. Balestrino, A. A. Sidorenko, G. Allodi, R. De Renzi, G. Ghiringhelli, C. Dallera, L. Braicovich, and N. B. Brookes. *Phys. Rev. B* **74**, 245116 (2006).

[91] C. Adamo, X. Ke, H. Q. Wang, H. L. Xin, T. Heeg, M. E. Hawley, W. Zander, J. Schubert, P. Schiffer, D. A. Muller, L. Maritato, and D. G. Schlom. *Appl. Phys. Lett.* **95 (11)**, 112504 (2009).

[92] H. Boschker, J. Kautz, E. P. Houwman, W. Siemons, D. H. A. Blank, M. Huijben, G. Koster, A. Vailionis, and G. Rijnders. *Phys. Rev. Lett.* **109**, 157207 (2012).

[93] J. Fontcuberta, V. Laukhin, and X. Obradors. *Appl. Phys. Lett.* **72 (20)**, 2607 (1998).

[94] H. Y. Hwang, S.-W. Cheong, P. G. Radaelli, M. Marezio, and B. Batlogg. *Phys. Rev. Lett.* **75**, 914 (1995).

[95] H. Y. Hwang, T. T. M. Palstra, S.-W. Cheong, and B. Batlogg. *Phys. Rev. B* **52**, 15046 (1995).

[96] J. Fontcuberta, B. Martinez, A. Seffar, S. Piñol, J. L. Garćia-Muñoz, and X. Obradors. *Phys. Rev. Lett.* **76**, 1122 (1996).

[97] Y. Suzuki, H. Y. Hwang, S.-W. Cheong, and R. B. van Dover. *Appl. Phys. Lett.* **71 (1)** (1997).

[98] C. Thiele, K. Dörr, O. Bilani, J. Rödel, and L. Schultz. *Phys. Rev. B* **75**, 054408 (2007).

[99] A. Tebano, C. Aruta, S. Sanna, P. G. Medaglia, G. Balestrino, A. A. Sidorenko, R. De Renzi, G. Ghiringhelli, L. Braicovich, V. Bisogni, and N. B. Brookes. *Phys. Rev. Lett.* **100**, 137401 (2008).

[100] D. Pesquera, G. Herranz, A. Barla, E. Pellegrin, F. Bondino, E. Magnano, F. Sánchez, and J. Fontcuberta. *Nat. Commun.* **3**, 1189 (2012).

[101] Y. Yang, M. Meng Yang, Z. L. Luo, H. Huang, H. Wang, J. Bao, C. Hu, G. Pan, Y. Yao, Y. Liu, X. G. Li, S. Zhang, Y. G. Zhao, and C. Gao. *Appl. Phys. Lett.* **100 (4)**, 043506 (2012).

[102] J. Stöhr. *NEXAFS spectroscopy*, (Springer Series in Surface Sciences 25, Berlin Heidelberg 1992).

[103] G. Schütz, E. Goering, and H. Stoll. In *Handbook of Magnetism and Advanced Magnetic Materials*, pages 1322–1332, (John Wiley & Sons 2007).

[104] E. U. Condon and G. H. Shortley. *The Theory of Atomic Spectra*, (Cambridge University Press, Cambridge 1963).

[105] J. C. Slater. *Quantum Theory of Atomic Structure, Vol. II*, (McGraw-Hill, New York 1960).

[106] B. T. Thole, P. Carra, F. Sette, and G. van der Laan. *Phys. Rev. Lett.* **68**, 1943 (1992).

[107] P. Carra, B. T. Thole, M. Altarelli, and X. Wang. *Phys. Rev. Lett.* **70**, 694 (1993).

[108] C. T. Chen, Y. U. Idzerda, H.-J. Lin, N. V. Smith, G. Meigs, E. Chaban, G. H. Ho, E. Pellegrin, and F. Sette. *Phys. Rev. Lett.* **75**, 152 (1995).

[109] F. de Groot. *Coordin. Chem. Rev.* **249 (12)**, 31 (2005).

[110] Y. Teramura, A. Tanaka, and T. Jo. *J. Phys. Soc. Jpn* **65 (4)**, 1053 (1996).

[111] Private communications with Cinthia Piamonteze.

[112] J. Stöhr and H. König. *Phys. Rev. Lett.* **75**, 3748 (1995).

[113] Private communications with Michael Fechner.

[114] A. Uldry, F. Vernay, and B. Delley. *Phys. Rev. B* **85**, 125133 (2012).

[115] Inorganic Crystal Structure Database, http://icsd.fiz-karlsruhe.de/icsd, ICSD Collection Code 186700.

[116] C. Piamonteze, U. Flechsig, S. Rusponi, J. Dreiser, J. Heidler, M. Schmidt, R. Wetter, M. Calvi, T. Schmidt, H. Pruchova, J. Krempasky, C. Quitmann, H. Brune, and F. Nolting. *J. Synchrotron Radiat.* **19 (5)**, 661 (2012).

[117] P. Nachimuthu, J. H. Underwood, C. D. Kemp, E. M. Gullikson, D. W. Lindle, D. K. Shuh, and R. C. C. Perera. *AIP Conf. Proc.* **705 (1)** (2004).

[118] A. Flank, G. Cauchon, P. Lagarde, S. Bac, M. Janousch, R. Wetter, J. Dubuisson, M. Idir, F. Langlois, T. Moreno, and D. Vantelon. *Nucl. Instrum. Meth. B* **246 (1)**, 269 (2006).

[119] T. Funk, A. Deb, S. J. George, H. Wang, and S. P. Cramer. *Coordin. Chem. Rev.* **249 (1)**, 3 (2005).

[120] R. Nakajima, J. Stöhr, and Y. U. Idzerda. *Phys. Rev. B* **59**, 6421 (1999).

[121] A. J. Achkar, T. Z. Regier, H. Wadati, Y.-J. Kim, H. Zhang, and D. G. Hawthorn. *Phys. Rev. B* **83**, 081106 (2011).

[122] J. Jaklevic, J. A. Kirby, M. Klein, A. Robertson, G. Brown, and P. Eisenberger. *Solid State Commun.* **23 (9)**, 679 (1977).

[123] S. Eisebitt, T. Böske, J.-E. Rubensson, and W. Eberhardt. *Phys. Rev. B* **47**, 14103 (1993).

[124] T. Wagner, G. Richter, and M. Rühle. *J. Appl. Phys.* **89 (5)**, 2606 (2001).

[125] M. Weinert and S. Blügel. In *Magnetic multilayers*, pages 51–83, (World Scientific Publishing Co. Pte. Ltd., Singapore 1994).

[126] M. Weinert, R. E. Watson, J. W. Davenport, and G. W. Fernando. *Phys. Rev. B* **39**, 12585 (1989).

[127] C. A. F. Vaz, Y. Segal, J. Hoffman, F. J. Walker, and C. H. Ahn. *J. Vac. Sci. Technol. B* **28 (4)**, C5A6 (2010).

[128] K. J. Choi, M. Biegalski, Y. L. Li, A. Sharan, J. Schubert, R. Uecker, P. Reiche, Y. B. Chen, X. Q. Pan, V. Gopalan, L.-Q. Chen, D. G. Schlom, and C. B. Eom. *Science* **306 (5698)**, 1005 (2004).

[129] K. Y. Yun, D. Ricinschi, T. Kanashima, M. Noda, and M. Okuyama. *Jpn. J. of Appl. Phys.* **43 (5A)**, L647 (2004).

[130] T. Saitoh, A. E. Bocquet, T. Mizokawa, H. Namatame, A. Fujimori, M. Abbate, Y. Takeda, and M. Takano. *Phys. Rev. B* **51**, 13942 (1995).

[131] T. Koide, H. Miyauchi, J. Okamoto, T. Shidara, T. Sekine, T. Saitoh, A. Fujimori, H. Fukutani, M. Takano, and Y. Takeda. *Phys. Rev. Lett.* **87**, 246404 (2001).

[132] R. D. Cowan. *The Theory of Atomic Structure and Spectra*, (Los Alamos Series in Basic and Applied Sciences, University of California Press, California 1981).

[133] A. Anane, C. Dupas, K. Le Dang, J. P. Renard, P. Veillet, A. M. de Leon Guevara, F. Millot, L. Pinsard, and A. Revcolevschi. *J. Phys. Condens. Matter* **7 (35)**, 7015 (1995).

[134] G. Jonker and J. V. Santen. *Physica* **16 (3)**, 337 (1950).

[135] A. Urushibara, Y. Moritomo, T. Arima, A. Asamitsu, G. Kido, and Y. Tokura. *Phys. Rev. B* **51**, 14103 (1995).

[136] R. V. Chopdekar, E. Arenholz, and Y. Suzuki. *Phys. Rev. B* **79**, 104417 (2009).

[137] B. Ravel. WebATOMS version 1.8 (Atoms 3.0 beta10), http://cars9.uchicago.edu/cgi-bin/atoms/atoms.cgi (2005).

[138] B. Delley. *J. Chem.Phys.* **92 (1)**, 508 (1990).

[139] L. Shu, Z. Li, J. Ma, Y. Gao, L. Gu, Y. Shen, Y. Lin, and C. W. Nan. *Appl. Phys. Lett.* **100 (2)**, 022405 (2012).

[140] J.-M. Hu, C.-W. Nan, and L.-Q. Chen. *Phys. Rev. B* **83**, 134408 (2011).

[141] T. Nan, Z. Zhou, M. Liu, X. Yang, Y. Gao, B. A. Assaf, H. Lin, S. Velu, X. Wang, H. Luo, J. Chen, S. Akhtar, E. Hu, R. Rajiv, K. Krishnan, S. Sreedhar, D. Heiman, B. M. Howe, G. J. Brown, and N. X. Sun. *Sci. Rep.* **4**, 3688 (2014).

[142] E. A. Owen and D. Madoc Jones. *P. Phys. Soc. Lond.* **67 (1)**, 459 (1954).

[143] R. W. G. Wyckoff. *Crystal Structures 1*, (Interscience Publishers, New York 1963).

[144] M. Tischer, O. Hjortstam, D. Arvanitis, J. Hunter Dunn, F. May, K. Baberschke, J. Trygg, J. M. Wills, B. Johansson, and O. Eriksson. *Phys. Rev. Lett.* **75**, 1602 (1995).

[145] T. Wu, A. Bur, P. Zhao, K. P. Mohanchandra, K. Wong, K. L. Wang, C. S. Lynch, and G. P. Carman. *Appl. Phys. Lett.* **98 (1)**, 012504 (2011).

[146] M. Weinert, R. E. Watson, and J. W. Davenport. *Phys. Rev. B* **32 (4)**, 2115 (1985).

[147] A. I. Liechtenstein, M. I. Katsnelson, V. P. Antropov, and V. A. Gubanov. *J. Magn. Magn. Mater.* **67 (1)**, 65 (1987).